TÉCNICO LISBOA

Performance Evaluation of GPS Auto-Surveying Techniques

João Gonçalo Filipe Manito

Thesis to obtain the Master of Science Degree in

Aerospace Engineering

Supervisor(s): José Eduardo Charters Ribeiro da Cunha Sanguino

Examination Committee

Chairperson: Prof. José Fernando Alves da Silva
Supervisor: Prof. José Eduardo Charters Ribeiro da Cunha Sanguino
Member of the Committee: Prof. Francisco António Bucho Cercas

March 2021

To my family and friends, without whom I wouldn't be here today.

Declaration

I declare that this document is an original work of my own authorship and that it fulfills all the requirements of the Code of Conduct and Good Practices of the Universidade de Lisboa.

Acknowledgments

This thesis marks the end of my journey at Instituto Superior Técnico, which had its ups and downs but which I will forever cherish and be proud of.

To my supervisor and tutor, Prof. José Sanguino, my sincere thanks for his guidance, support and help, as well as putting up with me since my first year at this university as my tutor. His approachability helped spark my interest in Navigation Systems, an interest I will carry for the foreseeable future.

I would also like to thank Instituto de Telecomunicações (IT) for all the resources that were made available to work on my thesis.

To my family, who have been with me through many hardships and without whom I wouldn't be writing this thesis, my most heartfelt thanks.

To my friends at IST, Tiago, Mónica, Pedro, Bernardo, Alexandre (both of them), Daniel, Inês, and many others. Thank you for your help, friendship and camaraderie. I hope one day we can work together again.

To my friends back at home, Diogo, Gonçalo, Pedro (both of them), Daniela, Marta, Vanessa, Catarina, a big thank you for many, many years of friendship and support.

And finaly, to my coworkers and Professors at LTI-DEQB, who managed to turn a job into some of my fondest memories. I will miss you all (and even all the work!).

Note regarding experimental data and source code access

In the spirit of free and unrestricted access to academic research and experimental data, all the datasets used in this thesis will be published free of charge in a Github repository, `https://github.com/JGManito/msc-thesis-data`, under the Creative Commons Zero v1.0 Universal license.

The source code used for this thesis will also be available in a Github repository, `https://github.com/JGManito/msc-thesis-code-public`, under the GNU General Public License v3.0.

If, for some reason, the data or source code are no longer available contact me through the e-mail joao.manito@tecnico.ulisboa.pt to request a copy.

Resumo

Com a massificação da utilização dos sistemas de navegação global por satélite (GNSS), cada vez mais aplicações estão a fazer uso de dados de posicionamento precisos. De todos os métodos de posicionamento desenvolvidos para GNSS, os mais precisos são aqueles baseados em sistemas diferenciais, como GNSS diferencial (DGNSS) e Real-Time Kinematics (RTK), usando uma estação de referência. No entanto, estes sistemas necessitam de saber a posição desta estação com grande precisão para poderem ser precisos. É sobre esta problemática que a presente tese incide.

Foram analizados quatro métodos de posicionamento, nomeadamente o Método dos Mínimos Quadrados (LS), o Método dos Mínimos Quadrados Ponderados (WLS), o Filtro de Kalman Extendido (EKF) e o Filtro de Kalman Unscented (UKF), usando apenas pseudoranges como medições. Foram testados também o Filtro de Hatch, RAIM e métodos estatísticos, de forma a caracterizar várias possibilidades para métodos de auto-posicionamento de um receptor estático.

Testados estes métodos, verificou-se que o EKF e UKF apresentam muito melhores resultados que o LS e o WLS no seu erro médio, conseguindo uma precisão abaixo de 1 metro ao fim de cerca de 4 horas. Verificou-se também que o sistema de RAIM é importante para o auto-posicionamento.

Escolhida a combinação de métodos que apresenta melhores resultados, esta foi testada contra implementações existentes revelando que é bastante competitiva, principalmente quando considerando as diferenças entre receptores utilizados. Finalmente, estes resultados foram utilizados num teste de DGNSS que verificou a melhoria significativa da estimativa de posição quanto melhor for a estimativa de posição da estação de referência.

Palavras-chave: GNSS, GPS, Estação-base, Auto-posicionamento

Abstract

With the increase in widespread use of Global Navigation Satellite Systems (GNSS), more and more applications require precise position data. Of all the GNSS positioning methods, the most precise ones are those that are based in differential systems, like Differential GNSS (DGNSS) and Real-Time Kinematics (RTK). However, these systems require a very precise estimate of their reference station position to have good precision. This is the problem this thesis set out to study.

Four positioning methods were analyzed, namely Least Squares (LS), Weighted Least Squares (WLS), Extended Kalman Filter (EKF) and Unscented Kalman Filter (UKF), using only pseudorange measurements. It was also tested the Hatch Filter, RAIM and statistical methods, in order to characterize several possible methods of auto-survey for a static receiver.

After testing, it is seen that the EKF and UKF present much better mean error results than LS and WLS, with an attained precision below 1 meter after about 4 hours. It was also verified the importance of RAIM for the self-survey procedure.

Chosen the combination of methods that gives the best results, it was tested against existing implementations showing it is very competitive, especially considering the differences between the used receivers.

Finally, these results were used in a DGNSS test, which verified a significant improvement in the position estimate as the base station position estimate improves.

Keywords: GNSS, GPS, Base-station, Auto-surveying

Contents

Nomenclature i
Acknowledgments vi
Note regarding experimental data and source code access vii
Resumo ix
Abstract xi
List of Tables xvii
List of Figures xix
Nomenclature xxi

1 Introduction **1**
1.1 Motivation 1
1.2 State of the Art 2
1.3 Objectives 2
1.4 Thesis Outline 3

2 Background **4**
2.1 Overview of the GPS 4
2.2 GPS Architecture 5
2.2.1 Space Segment 5
2.2.2 Control Segment 6
2.2.3 User Segment 6
2.3 Coordinate Systems 7
2.3.1 Earth-Centered Inertial (ECI) coordinate system 7
2.3.2 Earth-Centered, Earth-Fixed (ECEF) reference frame 8
2.3.3 World Geodetic System 1984 (WGS84) 8
2.3.4 East-North-Up (ENU) reference frame 8
2.3.5 Conversion between reference frames 9
2.4 Error sources in GPS measurements 11
2.4.1 Satellite clock errors 11
2.4.2 Tropospheric delay 12
2.4.3 Ionospheric delay 14

2.4.4 Ephemeris errors . . . 15
2.4.5 Multipath error . . . 15
2.4.6 GPS pseudorange error budget . . . 16
2.5 GPS Observables . . . 16
2.5.1 Pseudorange . . . 17
2.5.2 Carrier phase . . . 18
2.6 Dilution of Precision . . . 19
2.7 Position accuracy measures . . . 19
2.7.1 2D accuracy metrics . . . 20
2.7.2 3D accuracy Metrics . . . 20
2.8 Maximum Likelihood Estimation . . . 21

3 Position Determination **23**
3.1 Least Squares . . . 23
3.2 Weighted Least Squares . . . 25
3.3 Extended Kalman Filter . . . 26
3.3.1 Dynamics model . . . 27
3.3.2 Observations Model . . . 28
3.3.3 Algorithm . . . 30
3.4 Unscented Kalman Filter . . . 30
3.4.1 Unscented Transform . . . 30
3.4.2 Algorithm . . . 31
3.5 Carrier-Smoothed Code - the Hatch Filter . . . 31
3.6 Differential GPS . . . 34
3.7 RAIM . . . 37
3.7.1 Fault detection and handling of conventional RAIM . . . 38
3.7.2 Least Squares Residuals . . . 38

4 Precise Positioning **41**
4.1 International GNSS Service . . . 41
4.2 Precise Point Positioning . . . 42

5 Experimental Results **45**
5.1 Problem Description . . . 45
5.2 Experimental Setup . . . 45
5.2.1 Receivers . . . 45
5.2.2 Antennas . . . 47
5.2.3 Software . . . 47
5.3 Antenna reference position determination . . . 48
5.3.1 Reference Station antenna position . . . 48

5.3.2 Fixed Rover antenna position . . . 50
5.3.3 ProFlex 500 receiver antenna position . . . 51
5.4 Algorithm validation using IGS station data . . . 52
5.4.1 Positioning algorithm validation . . . 52
5.4.2 Hatch filter validation . . . 55
5.5 Reference Station antenna position determination . . . 59
5.6 Convergence over time of the position solution . . . 60
5.7 Improving the position estimate with statistical methods . . . 61
5.7.1 The median as position estimate . . . 62
5.7.2 The weighted average as position estimate . . . 62
5.7.3 The MLE as position estimate . . . 63
5.8 Filtering using a threshold . . . 64
5.9 Final proposed positioning method . . . 64
5.10 Impact of RAIM in auto-surveying . . . 67
5.11 Performance comparison with existing auto-survey methods . . . 69
5.12 Differential GPS test . . . 70

6 Conclusions **73**
6.1 Future Work . . . 73

Bibliography **75**

A Routines for downloading IGS GNSS data **79**
A.1 IGS_dump.bat . . . 79
A.2 IGS_merge.bat . . . 80

B Surveying procedure **81**
B.1 7 day survey - Antennas RF2 and RF6 . . . 81
B.2 2 day survey - Antenna RF4 . . . 82

List of Tables

2.1 Earth ellipsoid parameters from WGS84 datum 8
2.2 Meteorological parameters for tropospheric delay model 13
2.3 Typical UERE budget for single-frequency receiver 16

5.1 PPP position results for RF2 49
5.2 PPP position results for RF6 50
5.3 PPP position results for RF4 51
5.4 Error metrics for the reference receiver 53
5.5 Error metrics for the reference receiver after correction of initial position 54
5.6 Error metrics for different values of γ of the Hatch Filter for the reference position 58
5.7 Error metrics for 24 hour position survey of the Reference Station Antenna 59
5.8 Error metrics for 24 hour position survey of the reference station antenna using the finalized position methods 66
5.9 Error metrics for 24 hour position survey of the Reference Station Antenna after RAIM test 67
5.10 Mean error for the DGPS receiver with base station position averaged after a set number of hours 70

List of Figures

2.1 Current GPS constellation planar projection 6
2.2 Current GPS Control Segment facilities 7

3.1 Least Squares algorithm 25
3.2 Flowchart of the EKF algorithm for GPS positioning 29
3.3 Flowchart of the UKF algorithm for GPS positioning 33
3.4 GPS interferometer configuration for one satellite 34
3.5 GPS interferometer configuration for two satellites 35
3.6 Flowchart of the basic KF algorithm 37
3.7 Flowchart of the RAIM algorithm 40

5.1 u-blox EVK 6T Receiver 46
5.2 Ashtech ProFlex 500 Receiver 46
5.3 NovAtel GPSAntenna Model 521 GNSS antenna 47
5.4 Scatterplot of PPP position results for RF2 (day 1) 49
5.5 Scatterplot of PPP position results for RF6 (day 1) 51
5.6 Scatterplot of PPP position results for RF4 (day 1) 52
5.7 Absolute position error for the reference receiver 53
5.8 Absolute position error for the reference receiver after correction of initial position 54
5.9 Scatter plot of position results for the reference receiver after correction of initial position . 55
5.10 Detail of the effect of a cycle slip in the Hatch Filter 56
5.11 Detail of the result of cycle slip correction in the Hatch Filter 56
5.12 Absolute error for the reference receiver with Hatch Filter with $\gamma = 0.005$ 57
5.13 Absolute error for the reference receiver with Hatch Filter with $\gamma = 0.010$ 57
5.14 Absolute error for the reference receiver with Hatch Filter with $\gamma = 0.015$ 57
5.15 Absolute error for the reference receiver with Hatch Filter with $\gamma = 0.020$ 57
5.16 Absolute error for the RF2 antenna position with no Hatch Filter 59
5.17 Absolute error for the RF2 antenna position with Hatch Filter and $\gamma = 0.010$ 59
5.18 GDOP values for the 24 hour survey of the reference station antenna 60
5.19 Number of satellites used for position determination for the 24 hour survey of the reference station antenna 60

5.20 Mean error variation over time for the reference station antenna with no Hatch Filter . . . 61
5.21 Mean error variation over time for the reference station antenna with Hatch Filter and $\gamma = 0.010$ . . . 61
5.22 Median error variation over time for the reference station antenna with no Hatch Filter . . . 62
5.23 Median error variation over time for the reference station antenna with Hatch Filter and $\gamma = 0.010$ . . . 62
5.24 Weighted average error variation over time for the reference station antenna with no Hatch Filter . . . 63
5.25 Weighted average error variation over time for the reference station antenna with Hatch Filter and $\gamma = 0.010$ . . . 63
5.26 Maximum Likelihood Estimator error variation over time for the reference station antenna with no Hatch Filter . . . 63
5.27 Maximum Likelihood Estimator error variation over time for the reference station antenna with Hatch Filter and $\gamma = 0.010$ . . . 63
5.28 Effect of a 1σ threshold on the mean error over time for the reference station antenna with no Hatch Filter . . . 65
5.29 Effect of a 1σ threshold on the mean error over time for the reference station antenna with Hatch Filter and $\gamma = 0.010$ . . . 65
5.30 Effect of a 2σ threshold on the mean error over time for the reference station antenna with no Hatch Filter . . . 65
5.31 Effect of a 2σ threshold on the mean error over time for the reference station antenna with Hatch Filter and $\gamma = 0.010$ . . . 65
5.32 Mean error for 24 hour position survey of the reference station antenna using the finalized position methods . . . 66
5.33 Reference station receiver error in the presence of simulated faulty satellites without RAIM 68
5.34 Reference station receiver error in the presence of simulated faulty satellites with RAIM FDE algorithm . . . 68
5.35 RAIM test statistic for the simulated faulty satellites . . . 68
5.36 Auto-survey results for the u-blox 6T and ProFlex receivers for a 24 hour survey . . . 70
5.37 Rover position error with base station position obtained with EKF and averaged after a set number of hours . . . 71
5.38 Rover position error with base station position obtained with UKF and averaged after a set number of hours . . . 71

Nomenclature

CEP Circular Error Probable

CSC Carrier-Smoothed Code

DD Double Difference

DGNSS Differential Global Navigation Satellite Systems

DGPS Differential Global Positioning System

DOP Dillution of Precision

2DRMS Twice Distance Root Mean Squared

DRMS Distance Root Mean Squared

ECEF Earth-Centered, Earth-Fixed

ECI Earth-Centered Inertial

EKF Extended Kalman Filter

ENU East-North-Up

FDE Fault Detection and Exclusion

FD Fault Detection

GNSS Global Navigation Satellite Systems

GPS Global Positioning System

ICBM Intercontinental Ballistic Missile

IGS International GNSS Service

IP Internet Protocol

LADGPS Local Area Differential Global Positioning System

LS Least Squares

LSR Least Squares Residuals

MRSE Mean Radial Spherical Error

PPP Precise Point Positioning

PVT Position, Velocity and Time

RADGPS Regional Area Differential Global Positioning System

RAIM Receiver Autonomous Integrity Monitoring

RMS Root Mean Squared

RTK Real-Time Kinematics

RV Random Variable

SAS90 90% Spherical Accuracy Standard

SAS99 99% Spherical Accuracy Standard

SatNav Satellite Navigation

SBAS Satellite Based Augmentation System

SD Single Difference

SEP Spherical Error Probable

SPP Standard Point Positioning

SSE Sum of Squared Errors

TLS Total Least Squares

TOA Time-of-arrival

UKF Unscented Kalman Filter

USN United State's Navy

US United States (of America)

WADGPS Wide Area Differential Global Positioning System

WGS84 World Geodetic System 1984

WLS Weighted Least Squares

Chapter 1

Introduction

This chapter is dedicated to give a general overview of the topic that will be discussed in this thesis. A general presentation of the motivation for this thesis is given, as well as summary of the intended goals of the project and a basic outline of the structure of this thesis.

1.1 Motivation

Global Navigation Satellite Systems (GNSS), of which the most famous is the Global Positioning System (GPS), are of paramount importance in our contemporary society. From navigation to accurate time keeping, with many other uses in-between, these systems are deeply woven into the fabric of our life.

When the GPS constellation was initially launched, receivers where large boxes which required large amounts of power and big, clunky data-processing systems. Nowadays, most of us carry in our pockets at least one GPS-enabled device, small, sleek and inexpensive, which can interact with the rest of the world. This miniaturization brought about several new ways in which to leverage the capabilities of GNSS systems: self-driving vehicles, autonomous harbour freight transport, small, unmanned aircraft, etc. As a consequence of this phenomena, ever-more accurate receivers where required, to provide more accurate position solutions for new fields: autonomous navigation, GNSS-aided Geodesy, small-satellite positioning, guided projectiles (”smart ammunition”), etc.

While it is possible to obtain a position estimate with a single receiver, much more accurate estimates can be obtained by using two or more receivers in static locations and obtaining differential measurements to remove errors in the position determination. This is one of the requirements for several high-accuracy position estimation methods, like Differential GNSS (DGNSS) and Real-Time Kinematics (RTK).

However, this raises an important question: what is the real position of the reference receivers? This is the question that this thesis tries to answer. Using several methods, a comparative analysis of current position estimation methods will be done, with regards to both precision and time to convergence of the position solution.

1.2 State of the Art

When the original GPS constellation was completed, civilian signals where heavily hampered by pseudorandom errors purposely added to the GPS signal, a feature called *Selected Availability* (SA), to deny potential enemies of the United States of America the possibility of using the civilian GPS system for precise weapon guidance. As the added error was in the order of 50m RMS [1], possible applications of GPS were restricted to a very coarse position solution, which hampered applications like vehicle navigation and tracking and precision aircraft navigation around airports. Since these errors are highly correlated, i.e. they affected all the receivers in the same area in almost the same way, a method to use a reference station to determine the SA-induced error was developed, leading to the creation of Differential GPS (DGPS). This system is based on having one fixed reference GPS receiver with precisely known coordinates, using the difference between the position solution and the real position to determine the SA-induced error and finally to broadcast corrections to receivers in the reference station's coverage area. Consequently, a large number of DGPS reference stations where built in a short time, to provide precise navigation solutions for terrestrial, maritime and aerial traffic.

While SA has been disabled since May of 2000 [2] and is no longer present as a feature from GPS Block III satellites forward [3], DGPS still has a great precision advantage when compared to stand-alone positioning [4] and as such is still widely used in applications that require high-levels of accuracy and integrity.

The accuracy of a DGNSS base station is highly dependent on the accuracy of its position. As such, before they are brought online to provide DGNSS services, an initial survey of its position, a so-called auto-survey, is performed. This survey is usually done as a position solution average over a large time span. Such a measurement, although highly accurate, takes a long time to perform, usually in the order of days, in order to ensure that spurious errors and other effects are negated in the position estimate. It also makes use of very expensive, survey-grade GNSS receivers. This data is then processed using high precision positioning algorithms, yielding a very accurate position estimate.

1.3 Objectives

The main objective of this thesis is to analyse and compare several methods of obtaining a precise estimation of the position of a static receiver. It will be analyzed not only the overall precision of the position solution, but also the time it takes to reach that precision. The obtained results will be used to identify possible auto-survey methods to be applied to DGPS base stations.

In order to increase the scope of possible applications of this thesis, all the analysis will be done restricting the available variables to those captured by a simple, low-cost, single frequency receiver capable of outputting only pseudorange and carrier phase measurements, although the later will only be used for smoothing the pseudorange measurements. This allows the usage of very low-cost processors for the positioning algorithm, since the pseudorange-only approach is computationally much simpler due to not having to solve the integer ambiguity problem. Usage of differential corrections, satellite-

based augmentation systems and International GNSS Service (IGS) products wasn't considered for the position solution. This allows the simulation of a worst-case, or, more aptly, cheapest-case, DGPS base station receiver architecture, which increases the possible scope of application of this thesis.

Also, as a note, this work, while focused on GPS and, more precisely, DGPS base stations, can be applied to other GNSS systems as well with minor modifications.

1.4 Thesis Outline

In Chapter 1 the motivation behind this thesis was presented, as well as the objectives and an overview of the state of the art.

For Chapter 2, a description of the workings of a GNSS and DGNSS system is done, as well as the presentation of the measurement and error models for the GNSS observables. In this chapter is also introduced the concept of Maximum Likelihood Estimation, and are presented several error metrics.

In Chapter 3 several possible single-receiver positioning methods are introduced, as well as the augmentation method RAIM and the Double-Difference DGNSS positioning method.

For Chapter 4 the highly accurate PPP model is discussed briefly, which, although not used in this thesis for positioning, is used to determine the reference positions of the used antennas with high precision.

Following that, in Chapter 5 the results of the positioning methods are presented, as well as the results of several post-processing methods to obtain a better position estimate.

Finally, in Chapter 6 we present the conclusions of this thesis, as well as providing some avenues for further development of the obtained results.

Chapter 2

Background

2.1 Overview of the GPS

In 1958, a joint DARPA-Johns Hopkins University's Applied Physics Laboratory project, sponsored by the United State's Navy (USN), saw the birth of Transit, the first satellite navigation system in the world. While revolutionary, this system didn't provide 24/7 coverage, usually only a single satellite pass per roughly 1h. This severely limited the usability of Transit as a real-time precise navigation system, because single-pass errors where in the order of 27 to 37 meters RMS and required several satellite passes for more accurate position estimation; As an example, 10 passes where required for an horizontal accuracy of around 7 meters and 25 passes for about 5 meters [5]. While this was enough for the USN's Polaris system, who only needed to determine the position of a ballistic missile submarine accurately at the time of missile launch, such a system was unfit for both the much longer range Intercontinental Ballistic Missiles (ICBMs) of the United States' Air Force (USAF), which required accurate, real-time positioning to ensure they stayed on course, as well as it's strategic bombers, which couldn't wait several hours for a single, accurate positioning fix. Several projects where then developed in parallel by the various branches of the United States' armed forces, all of them associated with problems related to navigation: timekeeping, satellite orbital parameter measurement and precise ranging. This culminated in a single, multi-service project: the *Navstar Global Positioning System* system, later renamed to just GPS.

Conceptualized in the early 1970s, the GPS had it's first prototype satellite launched in 1978. A total of 10 prototype satellites where launched until 1985, and together are called *Block I*. These satellites validated several concepts and technologies required to the full-fledged GPS. A second generation of satellites, the *Block II*, was launched between 1989 and 1990, with a total of 9 satellites. These satellites where the first to have the payload required for complete GPS functionality. A slightly improved version, the *Block IIA*, was launched between 1990 and 1997. Initial GPS operational capacity was reached on December 1993 with a constellation of 24 satellites and full operational capacity reached on April 1995.

The GPS is divided in three segments: The Space Segment, consisting of the GPS satellite constellation; The User Segment, comprised of the user receivers; and the Control Segment, which includes

the GPS control stations and observatories that determine the orbital parameters of the satellites and all the necessary corrections.

Due to their limited design life, GPS satellites have been continuously replaced since their initial launch over 30 years ago, with the *Block IIR* series, where the R stands for *Replacement*, being launched between 1997 and 2004. A modernized version of this satellite, the *Block IIR-M*, was launched between 2005 and 2009. The final version of the *Block II* satellites, the *Block IIF* was designed to replace the *Block IIA* satellites and launched between 2010 and 2016.

Advances in technology during the development and launch of the *Block II* satellites and new requirements from both military and civilian users saw the creation of a completely new block of satellites, named *Block III*. These retain the original GPS signals, but add new signals and other features, increasing the scope of applications of the GPS satellite constellation. The *Block III* satellites are currently divided in two sub-blocks, *Block IIIA*, which started being launched in 2018 and and is the current, state-of-the-art GPS satellite, and *Block IIIF*, which will be launched no earlier than 2025.

While initially a military system, geopolitics tensions resulting from the Korean Air Lines Flight 007 incident over the Soviet Union saw US President Ronald Reagan issue a directive to allow free, civilian use of the GPS whenever it became available [6]. This directive started a new revolution in the maritime and aviation sectors, as well as broadening the access to very accurate geodesy measurements which, until that time, required the cooperation of the US Armed Forces for the access to GPS receivers. While initally the civilian service wasn't very accurate, the disabling of SA in May 2000 gave rise to a plethora of GPS-enabled devices, with the market for mobile devices and location-based services expected to increase around 8% per year until 2029 [7].

2.2 GPS Architecture

The GPS is divided into three segments: the space segment, the control segment and the user segment. Each one performs very different functions and the interoperability of all three is critical for the correct functioning of GPS.

2.2.1 Space Segment

The Space Segment of the GPS is comprised of a nominal constellation of 24 satellites, each placed in a specific slot in orbit around the Earth, and divided into six orbital planes with 4 slots each. The orbits are nearly circular, with an orbital radius of approximately 26600 km, and an inclination of 55º. This allows for complete coverage of the planet by ensuring that at every time there are at least 4 satellites in view of a receiver. Three expanded slots exist in the current configuration of the constellation, allowing for two satellites in the same slot and increasing the constellation size to 27 satellites. However, currently there are 31 operational GPS satellites [8], with the extra satellites being used as in-orbit spares.

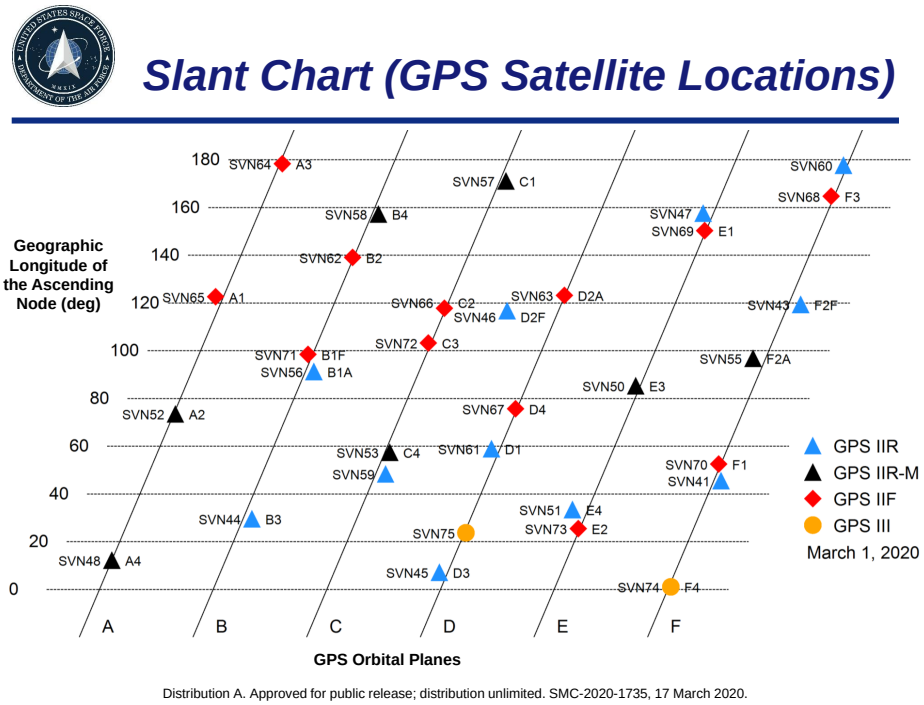

Figure 2.1: Current GPS constellation planar projection [8]

2.2.2 Control Segment

The Control Segment is the segment responsible for all the coordination, monitoring, command and control of the GPS constellation. This segment is composed of a network of ground-based stations and antennae, which monitors the GPS signals and update the navigation message, checks the satellite health, controls the orbits and eventual maneuvers of the satellites and provides a centralized way in which to control all the satellites.

Since the GPS is military in nature, facilities associated with the Control Segment are usually located in military bases, both those from the USA and those from USA-allied nations, with the Master Control Stations based in the USA. Figure 2.2 shows the location and type of all the current GPS Control Segment facilities.

2.2.3 User Segment

This segment encompasses all the users equipped with systems capable of receiving and processing GPS signals, in order to produce a Position, Velocity and Time (PVT) solution. These users can be civillian or military, commercial or private, but are characterized by having only the capability of receiving GPS signals, having no uplink capability whatsoever with regards to the GPS navigation subsystem (other links might exist, tied to other services provided by the GPS constellation).

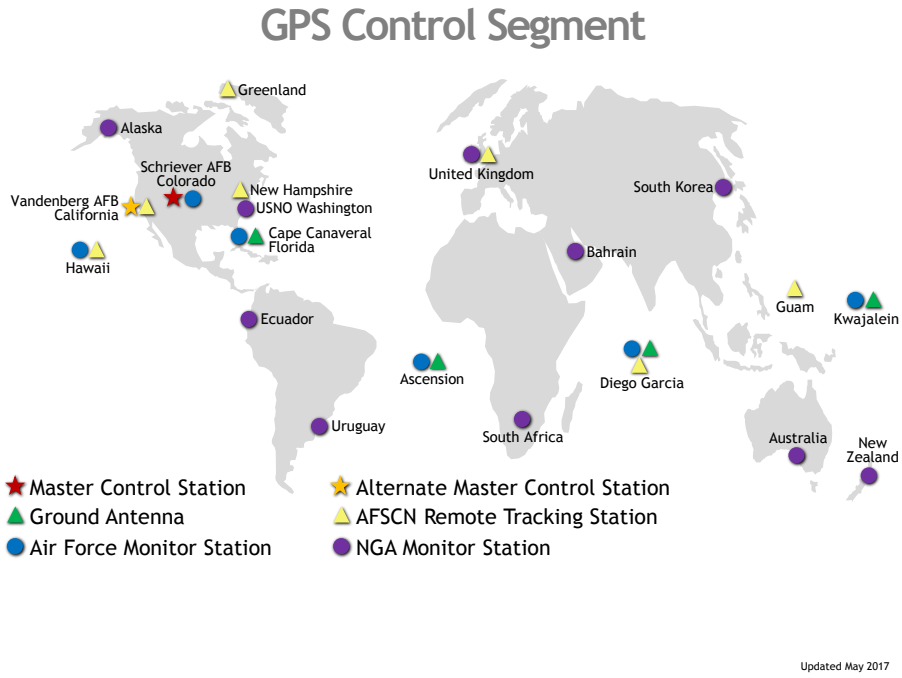

Figure 2.2: Current GPS Control Segment facilities [9]

2.3 Coordinate Systems

Being comprised of such distinct elements like satellites and ground receivers, it is of no surprise that different positions require different coordinate systems. In this section we will give a brief overview of the coordinate systems used throughout the entire process of user position determination.

2.3.1 Earth-Centered Inertial (ECI) coordinate system

For satellite orbit determination, an inertial reference frame is of obvious usage since it enables the satellite motion modelling using Newton's Laws, greatly simplifying the calculations involved. As such, the Earth-Centered Inertial (ECI) coordinate system was designed, with origin in Earth's center of mass, $+x$ axis pointed towards the vernal equinox, $+z$ axis perpendicular to the equatorial plane and pointing along the celestial North Pole and $+y$ axis pointed such that the three axis form a right-handed coordinate system.

While this coordinate system is taken as fixed, the Earth exhibits rotation, nutation and precession. This makes it so that the ECI coordinate system as defined before changes over time, making it necessary to choose a specific point in time, an epoch, as reference for the coordinate system orientation. An usual ECI coordinate system is called J2000, which takes as reference the equatorial plane at 12:00 UTC on January 1, 2000 [4].

2.3.2 Earth-Centered, Earth-Fixed (ECEF) reference frame

While for a satellite moving in space an inertial frame is the most adequate, for a receiver on Earth a coordinate system that rotates in sync with the Earth, i.e. fixed with respect to Earth's surface, is much more adequate. As such, the Earth-Centered, Earth-Fixed (ECEF) was devised, which represents positions as X,Y and Z coordinates.

Like the ECI reference frame, this coordinate system has its origin at the center of mass of the Earth. However, the *+x* axis is no longer fixed in space, rotating with the Earth and pointing towards the intersection of the equator with the prime meridian, (0º,0º). The *+y* axis now points in the direction of 90º East longitude, (0º,90º) and the *+z* axis is normal to the instantaneous equatorial plane and in the direction of the geographical North Pole, with the three axis forming a right-handed coordinate system. Also, since the ECEF frame has the *+x* axis pointed towards the equator, its angular velocity is the same as Earth's [4].

2.3.3 World Geodetic System 1984 (WGS84)

While an ECEF coordinate system might be able to represent the position of a receiver on Earth's surface, it doesn't lend itself to be of easy usage when it comes to having humans interpreting the resulting position. As such, the centuries-old method of referencing a position on Earth using latitude (ϕ), longitude (λ) and height (h) coordinates (LLH) is still the main representation of position data to a user. These coordinates are determined by the usage of an ellipsoidal model of Earth's shape, since Earth isn't a perfect sphere, which requires several geometric parameters. [4]

The WGS84 standard comprises both an ECEF reference frame and geodetic datum, providing the necessary geometrical parameters to compute the reference ellipsoid of the Earth [10]. These parameters are provided in Table 2.1.

Parameter	Symbol	Value	Units
Semi-major axis	a	6378137.0	m
Flattening Factor of the Earth	$1/f$	298.257223563	Unit-less
Geocentric Gravitational Constant	GM or μ	$3.986004418 \times 10^{14}$	m^3/s^2
Nominal Mean Angular Velocity of the Earth	ω	7.292115×10^{-5}	rad/s

Table 2.1: Earth ellipsoid parameters from WGS84 datum [10]

2.3.4 East-North-Up (ENU) reference frame

While the ECI and ECEF reference frames represent a position with relation to the center of the Earth, sometimes a more simple reference frame that has its origin on the surface of the Earth and is defined such that it forms a local tangent plane is used.

One such reference frame is the East-North-Up (ENU) frame. With the origin located on any point in the surface of the Earth, we define the Up axis along the ellipsoidal normal and outwards from the Earth, the North axis tangent to the ellipsoidal meridian and pointing towards the geographical North and the East axis perpendicular to the other two axis. [4]

2.3.5 Conversion between reference frames

While some coordinates are better expressed in one reference frame than another, sometimes it is necessary to convert between coordinate frames to allow certain calculations. The conversions used in this thesis are presented in this section.

Rotation Matrices

An important concept in coordinate conversion between cartesian reference systems is the concept of a rotation matrix. Such matrices, when a vector is multiplied by them, define a rotation around one of the axis of the reference frame. The matrices

$$R_x(\theta) = \begin{bmatrix} 1 & 0 & 0 \\ 0 & \cos\theta & \sin\theta \\ 0 & -\sin\theta & \cos\theta \end{bmatrix} R_y(\theta) = \begin{bmatrix} \cos\theta & 0 & -\sin\theta \\ 0 & 1 & 0 \\ \sin\theta & 0 & \cos\theta \end{bmatrix} R_z(\theta) = \begin{bmatrix} \cos\theta & \sin\theta & 0 \\ -\sin\theta & \cos\theta & 0 \\ 0 & 0 & 1 \end{bmatrix} \tag{2.1}$$

represent a rotation by angle θ around the x, y and z axis respectively, with positive θ representing a counterclockwise rotation of the axis when the origin is viewed from the positive end of that axis [4].

ECEF to Geodetic

The conversion between these two coordinate systems is accomplished by using the Heikkinen (1984) method for latitude and height [11] [12] and the Vermeille (2004) method for longitude [13]. Let $P_{ECEF} = (x, y, z)$ be a point in the ECEF frame, and $P_{LLH} = (\phi, \lambda, h)$ be its equivalent in a geodetic system.

For a given ellipsoid with semi-major axis a and flattening factor f we can define the eccentricity of the ellipsoid, e, and ellipsoidal polar radius, b, respectively as

$$b = a(1 - f)$$

$$e = \sqrt{1 - \frac{b^2}{a^2}}$$

We then define the two-dimensional distance in the *xy* plane, r, as

$$r = \sqrt{x^2 + y^2}$$

Then, Heikkinen's formula for latitude and geodetic height is

$$
\begin{aligned}
e'^2 &= (a^2 - b^2)/b \\
F &= 54b^2z^2 \\
G &= r^2 + (1-e^2)z^2 - e^2(a^2-b^2) \\
c &= e^4Fr^2/G^3 \\
s &= \sqrt[3]{1 + c + sqrtc^2 + 2c} \\
P &= \frac{F}{(3(s + s^{-1} + 1)^2G^2} \\
Q &= \sqrt{q + 2e^4P} \\
r_0 &= -\frac{Pe^2r}{1+Q} + \sqrt{\frac{a^2}{2}\left(1 + \frac{1}{Q}\right) - \frac{P(1-e^2)z^2}{Q(1+Q)} - \frac{Pr^2}{2}} \\
U &= \sqrt{(r - e^2r_0)^2 + (1-e^2)z^2} \\
z_0 &= \frac{b^2z}{aV} \\
h &= U\left(1 - \frac{b^2}{aV}\right) \\
\phi &= \arctan\left((z + e'^2z_0)/r\right)
\end{aligned}
$$

And finally Vermeille's formula for longitude is

$$
\lambda = \begin{cases} \frac{\pi}{2} - 2\arctan\frac{x}{r+y}, & \text{if } y \geq 0 \\ -\frac{\pi}{2} + 2\arctan\frac{x}{r-y}, & \text{if } y < 0 \end{cases}
$$

Geodetic to ECEF

While the conversion between ECEF and geodetic coordinates isn't straightforward and is still an active field of research, the conversion between geodetic and ECEF coordinates is direct.

For a given ellipsoid with semi-major axis a, flattening factor f and eccentricity e we can obtain the radius of curvature in the prime vertical, R_N, in meters using [14]:

$$
R_N = \frac{a}{\sqrt{1 - e^2(sin\phi)^2}}
$$

We then can compute the cartesian coordinates using [14]:

$$
\begin{aligned}
x &= (R_N + h)\cos\phi\cos\lambda \\
y &= (R_N + h)\cos\phi\sin\lambda \\
z &= \left((1-f)^2R_N + h\right)\sin\phi\right)
\end{aligned}
$$

where (x, y, z) are the desired cartesian coordinates and (ϕ, λ, h) are the original geodetic coordinates.

ECEF to ENU

To convert coordinates of a point from an ECEF coordinate system to a local ENU coordinate system we first need to define the origin of the ENU frame. Let $P = (x, y, z)$ be the point whose coordinates we want to compute, and $P_{0,ECEF} = (x_0, y_0, z_0)$ and $P_{0,LLH} = (\phi_0, \lambda_0, h_0)$ be the location of the origin of the ENU frame in the ECEF and Geodetic reference systems respectively.

This conversion corresponds to a translation of the ECEF frame to the origin of the ENU frame combined with a rotation about the z axis and another around the x axis [4]:

$$\begin{bmatrix} e \\ n \\ u \end{bmatrix} = \mathbf{R_x}\left(\frac{pi}{2} - \phi\right)\mathbf{R_z}\left(\frac{pi}{2} + \lambda\right)\begin{bmatrix} x - x_0 \\ y - y_0 \\ z - z_0 \end{bmatrix} = \begin{bmatrix} -\sin\lambda_0 & \cos\lambda_0 & 0 \\ -\sin\phi_0\cos\lambda_0 & -\sin\phi_0\sin\lambda_0 & \cos\phi_0 \\ \cos\phi_0\cos\lambda_0 & \cos\phi_o\sin\lambda_0 & \sin\phi_0 \end{bmatrix}\begin{bmatrix} x - x_0 \\ y - y_0 \\ z - z_0 \end{bmatrix}$$

where $P' = (e, n, u)$ are the coordinates of point P in the ENU frame

From the ENU frame we can also obtain two angular coordinates of point P': its azimuth, α and elevation, ϵ. These are given by[1]:

$$\alpha = \arctan\frac{e}{n}$$

$$\epsilon = \arctan\frac{u}{\sqrt{n^2 + e^2}}$$

2.4 Error sources in GPS measurements

2.4.1 Satellite clock errors

While the atomic clocks on GPS satellites are very precise, they aren't without error. And, since the GPS signals travel at the speed of light, even a small clock error will produce a large range error, in the order of kilometers [4]. Since the synchronization of the entire GPS constellation is a complex problem, instead every GPS satellite's atomic clocks are allowed to drift within a certain tolerance, and corrections to remove this drift are calculated by the Control Segment and broadcasted by the satellite.

The clock correction is then computed using the following second-degree polynomial [1]:

$$\Delta t_{SV} = a_{f0} + a_{f1}(t_{sv} - t_{oc}) + a_{f2}(t_{sv} - t_{oc})^2 + \Delta t_r \tag{2.2}$$

where:

- a_{f0},a_{f1},a_{f2} are the correction polynomial coefficients;
- t_{sv} is the current satellite time;
- t_{oc} is the clock data reference time;
- Δt_r is a relativistic correction due to orbital eccentricity.

[1] For the elevation angle the function $\arctan$ represents the quadrant-dependant $\arctan$ function, usually called atan2 in mathematical programming libraries

All of these parameters are broadcasted in the navigation message, with exception of the relativistic correction. The relativistic correction term, Δt_r can be calculated from orbital parameters using [15]:

$$\Delta t_r = Fe\sqrt{A}\sin E_k \tag{2.3}$$

where

- F is a constant with value $-4.442807633 \times 10^{-10}\ s/m^{1/2}$
- e is the satellite orbital eccentricity
- A is the satellite orbit's semi-major axis
- E_k is the satellite orbit's eccentric anomaly

Another correction parameter, only for the single-frequency receiver case, is the group differential delay, T_{GD}. This parameter is associated with the delay between the signal output of a GPS satellite measured at the antenna phase center and the output of the satellite's frequency source [15]. This parameter is broadcasted in the navigation message.

Finally, the correction can be applied to the current satellite time using [15]

$$t = t_{sv} - \Delta t_{sv} + T_{GD} \tag{2.4}$$

where t denotes the GPS system time.

2.4.2 Tropospheric delay

When the GPS signals reach the troposphere, the presence of dry gases and water vapour will create refraction phenomena, which will increase the path travelled by the GPS signal and result in a delay.

Several empirical models exist for the computation of the tropospheric delay, taking into account parameters like temperature, humidity and pressure. Some of these require that a receiver obtains such atmospheric data from an atmospheric sensor, while others resort to using long-term, average atmospheric data, dependent on user position and time of year. For this thesis, the selected model is the MOPS Troposphere Model, used by the SBAS systems [16]. This model was chosen because it not only has a known track record, being used by the SBAS systems, but it also doesn't depend on *in situ* measurements of atmospheric parameters, reducing the overall cost and complexity of the receiver.

The tropospheric delay correction for a given satellite elevation, ϵ, is given by [17] (here with a slightly different nomenclature):

$$T(\epsilon) = (T_{z,dry} + T_{z,wet})\, M(\epsilon) \tag{2.5}$$

where the obliquity factor, $M(\epsilon)$ is given by the mapping:

$$M(\epsilon) = \frac{1.001}{\sqrt{0.002001 + \sin^2(\epsilon)}} \tag{2.6}$$

valid for elevation angles over 5º, and $T_{z,dry}$ and $T_{z,wet}$ are the vertical delays of the wet and dry components of the troposphere.

The $T_{z,dry}$ and $T_{z,wet}$ terms depend on several meteorological parameters, namely pressure ($P, mbar$), temperature (T, K), water vapour pressure (e, $mbar$), temperature lapse rate (β, K/m) and water vapour lapse rate (λ, dimensionless). Each of these parameters is computed from the linear interpolation of average and seasonal variation values given in Table 2.2 and the receiver latitude, ϕ, and day-of-year, D, using [17]

$$\xi(\phi, D) = \xi_0(\phi) - \Delta\xi(\phi)\cos\left[\frac{2\pi(D - D_{min})}{365.25}\right] \tag{2.7}$$

where $\xi_0(\phi)$ and $\Delta\xi(\phi)$ are, respectively, the average and seasonal variation values of each parameter at a given latitude, and $D_{min} = 28$ for northern latitudes and $D_{min} = 211$ for southern latitudes.

	Average				
Latitude (º)	$P_0(mbar)$	$T_0(K)$	$e_0(mbar)$	$\beta_0(mbar)$	λ_0
15° or less	1013.25	299.65	26.31	$6.30 \cdot 10^{-3}$	2.77
30	1017.25	294.15	21.79	$6.05 \cdot 10^{-3}$	3.15
45	1015.75	283.15	11.66	$5.58 \cdot 10^{-3}$	2.57
60	1011.75	272.15	6.78	$5.39 \cdot 10^{-3}$	1.81
75° or greater	1013.00	263.65	4.11	$4.53 \cdot 10^{-3}$	1.55

	Seasonal Variation				
Latitude (º)	$\Delta P(mbar)$	$\Delta T(K)$	$\Delta e(mbar)$	$\Delta\beta(mbar)$	$\Delta\lambda$
15° or less	0.00	0.00	0.00	$0.00 \cdot 10^{-3}$	0.00
30	−3.75	7.00	8.85	$0.25 \cdot 10^{-3}$	0.33
45	−2.25	11.00	7.24	$0.32 \cdot 10^{-3}$	0.46
60	−1.75	15.00	5.36	$0.81 \cdot 10^{-3}$	0.74
75° or greater	−0.50	14.50	3.39	$0.62 \cdot 10^{-3}$	0.3

Table 2.2: Meteorological parameters for tropospheric delay model [17]

To compute the tropospheric delay terms, we first need to compute the respective zero-altitude delays:

$$T_{z_0,dry} = \frac{10^{-6}k_1R_dP}{g_m} \tag{2.8}$$

$$T_{z_0,dry} = \frac{10^{-6}k_2R_d}{(\lambda+1)g_m - \beta R_d}\frac{e}{T} \tag{2.9}$$

and finally we compute the vertical delay at the receiver height, H

$$T_{z,dry} = \left[1 - \frac{\beta H}{T}\right]^{\frac{g}{R_d\beta}} \cdot T_{z_0,dry} \tag{2.10}$$

$$T_{z,wet} = \left[1 - \frac{\beta H}{T}\right]^{\frac{(\lambda+1)g}{R_d \beta} - 1} \cdot T_{z_0,wet} \tag{2.11}$$

where

- $k_1 = 77.604\ K/mbar$
- $k_2 = 382000\ K^2/mbar$
- $R_d = 287.054\ J/Kg/K$
- $g_m = 9.784\ m/s^2$
- $g = 9.80665 m/s^2$
- P, T, e, β and λ are the atmospheric parameters computed using Equation 2.7

2.4.3 Ionospheric delay

During their travel between satellite and receiver, the GPS signals pass through a layer of the atmosphere called the ionosphere. This layer, located between 70 and 1000km, is a dispersive medium, and its influence on the GPS signals depends on the concentration of free electrons, released from sun-atmosphere interactions [4].

For the GPS, the most used model is the Klobuchar model, which reduces, on average, about 50% of the RMS ionospheric delay for a single-frequency receiver [18]. It assumes that the electron content is concentrated in a thin layer at 350 km of altitude, which is pierced by the GPS signal at a given point, named Ionospheric Pierce Point (IPP). From here, the vertical delay is computed and then a mapping function converts it to a slant delay. This is the model used by the GPS and whose parameters are broadcasted by the GPS satellites in their navigation messages.

The Klobuchar model is given by the following equations [15]:

$$\psi = \frac{0.0137}{E + 0.11} - 0.022 \qquad \text{(in semicircles)} \tag{2.12}$$

$$\begin{cases} \phi_i = \phi_u + \psi \cos A, & \text{if } |\phi_i| \leq 0.416 \\ \text{if } \phi_i > +0.416, & \text{then } \phi_i = +0.416 \\ \text{if } \phi_i < -0.416, & \text{then } \phi_i = -0.416 \end{cases} \qquad \text{(in semicircles)} \tag{2.13}$$

$$\lambda_i = \lambda_u + \frac{\psi \sin A}{\cos \phi_i} \qquad \text{(in semicircles)} \tag{2.14}$$

$$\phi_m = \phi_i + 0.064 \cos(\lambda_i - 1.617) \qquad \text{(in semicircles)} \tag{2.15}$$

$$\begin{cases} t = 43200 \lambda_i + t_{GPS}, & \text{if } 0 \leq t \leq 86400 \\ \text{if } t \geq 86400, & \text{then } t = t - 86400 \\ \text{if } t < 0, & \text{then } t = t + 86400 \end{cases} \qquad \text{(in seconds)} \tag{2.16}$$

$$AMP = \begin{cases} \sum_{n=0}^{3} \alpha_n \phi_m^n, & \text{if } AMP \geq 0 \\ \text{if } AMP < 0, & \text{then } AMP = 0 \end{cases} \quad \text{(in seconds)} \tag{2.17}$$

$$PER = \begin{cases} \sum_{n=0}^{3} \beta_n \phi_m^n, & \text{if } PER \geq 0 \\ \text{if } PER < 72000, & \text{then } PER = 72000 \end{cases} \quad \text{(in seconds)} \tag{2.18}$$

$$x = \frac{2\pi(t - 50400)}{PER} \quad \text{(in radians)} \tag{2.19}$$

$$F = 1.0 + 16.0(0.53 - E)^3 \tag{2.20}$$

$$T_{iono} = \begin{cases} F \cdot \left[5 \cdot 10^{-9} + AMP \left(1 - \frac{x^2}{2} + \frac{x^4}{24} \right) \right], & \text{if } |x| < 1.57 \\ F \cdot \left(5 \cdot 10^{-9} \right), & \text{if } |x| \geq 1.57 \end{cases} \quad \text{(in seconds)} \tag{2.21}$$

where:

- ϕ_u and λ_u are the approximate receiver latitude and longitude
- t_{GPS} is the GPS system time after corrections
- α_n and β_n are the Klobuchar parameters included in the GPS navigation message
- A and E are the satellite azimuth and elevation respectively in semicircles, here with a different symbol to avoid confusion with the Klobuchar parameters

While usually angles are given in radians or degrees, the Klobuchar model works with semicircles. The conversion between these units is:

$$1 \text{ semicircle} = 180^\circ = \pi \text{ radians} \tag{2.22}$$

2.4.4 Ephemeris errors

One of the roles of the GPS Control Segment is the determination of orbital elements of the GPS satellites. This is achieved by a set of ground-based tracking stations, whose measurements are then collected and a curve-fit is done to determine accurate orbital elements [4]. After these orbital elements are calculated, they are sent to the GPS satellites via uplink stations, and then broadcasted to the users via the navigation message. This orbital data isn't calculated in real time, but is refreshed over a few hours for every satellite [1], meaning that its best fit will be at the time of computation. As such, after a while perturbations will accumulate on the satellite's orbit, creating a difference between the computed and real orbit, which in turn will add some error to the receiver position solution.

2.4.5 Multipath error

Near the Earth's surface, the GPS signals might encounter obstacles in their line of sight that difract or reflect the signals, like buildings or trees, or even the ground. Those signals are then received by the GPS receiver as delayed versions of the direct signal, because their travel path is longer.

If the delay is long enough, corresponding to a distant source of reflection, then the receiver can mitigate the multipath effect, and it has little effect on the position solution. However, when the delay is short, in the order of tens or hundreds of nanoseconds [4], they distort the received signal in a way that cannot be easily resolved by the receiver, degrading the position solution.

This effect is highly dependent on surface characteristics, so it is not an easy error to model; However, a choke ring can be added to the GPS antenna to reduce the effect of the multipath interference, as was done in the experimental setup used in this thesis. Due to this fact, this error has not been accounted for in the algorithm used in this thesis.

2.4.6 GPS pseudorange error budget

Given that all the previous sections discussed the different errors that affect the GPS signal, it is logical to follow with a budget of the errors that affect the GPS signals. In this case, we will focus only on the single-frequency receiver case, as well as only the errors that affect the pseudoranges, which we will approach in Chapter 2.5.1.

The combination of all the previous errors result in an overall error value that is known as the User Equivalent Range Error (UERE), given by the Root-Sum-Squared (RSS) of all the different components. This error is assumed to be gaussian-distributed, and all the components are treated as independent random variables [1].

All the different errors that together give the UERE can be found in Table 2.3.

Segment Source	**Error Source**	1σ **Error (m)**
Space/Control	Broadcast clock	0.4
	Broadcast ephemeris	0.3
	Differential group delay	0.15
User	Residual ionospheric delay	7.0
	Tropospheric delay	0.2
	Receiver noise and resolution	0.1
	Multipath	0.2
System UERE	Total	7.03

Table 2.3: Typical UERE budget for single-frequency receiver [4]

2.5 GPS Observables

While we usually only see the final position output of a GPS receiver, in the background there are several quantities being measured which will be used to compute the receiver's position. The two most used observables are the pseudorange and the carrier phase, which give a measure of the distance between receiver and satellite.

2.5.1 Pseudorange

The most basic method of positioning relies on knowing the range between a receiver and three transmitters, where the receiver position is the point that satisfies the ranges for the three transmitters. However, this method uses *range*, not *pseudorange*. So, what is the difference?

Let us start at the beginning. A GPS receiver can determine its position by usage of ranging codes, using a modified version of the so called time-of-arrival (TOA) ranging method. These codes work by having the receiver correlate the received code with an internal replica code tied to the receiver's clock that is time-shifted until it matches the received code. When that correlation is maximum, the time difference between transmission and reception is subtracted from the receiver's clock time, obtaining the transmission time as seen by the receiver [14].

By determining the time difference between broadcast and reception of a ranging code, one can obtain the distance to the transmitter; expanding this concept to a three-dimensional scenario, the problem requires the determination of the three position coordinates of the receiver as well as the receiver clock bias. By having four unknowns, 4 linearly independent equations are required to solve the problem, which corresponds to 4 measurements to different satellites. This is the basis of *Code Based Positioning*, and represents the most usual method of position calculation.

The distance, as seen by the receiver, between the receiver and a GPS satellite in orbit is given by

$$r = c\,(t_u - t_s) = c\Delta t \tag{2.23}$$

where:

- r is the true range to the satellite
- t_s is the true time of departure of the signal from the GPS satellite
- t_u is the true time of arrival of the signal to the receiver
- c is the speed of light in a vaccum
- Δt is the true travel time of the signal

However, since both the satellite and receiver clocks present some degree of error, using the previous formula will almost always yield a distance that is different from the true range. The time of propagation of the GPS signals is also affected by the propagation media since the signal won't always travel in vacuum, as well as reflections and other phenomena. The measured distance with all these errors and perturbations is then significantly different from the true range, and as such we call this measured distance *pseudorange*, ρ.

Adding the different delays and errors, we can write a new equation for the time of arrival method using the pseudorange

$$\rho^i = r^i + c\delta t_r - c\delta t^i + T^i + I^i + MP^i + \epsilon_\rho \tag{2.24}$$

where:

- δt_r and δt^i are the receiver and satellite clock errors (in seconds)

- T^i is the tropospheric delay (in meters) between the receiver and satellite i
- I^i is the ionospheric delay (in meters) between the receiver and satellite i
- MP^i is the multipath error (in meters) between the receiver and satellite i
- ϵ_ρ denotes any unmodelled errors in the pseudorange

2.5.2 Carrier phase

Another parameter that can be measured from the GPS signals is the phase of the received signal, relative to the receiver-generated carrier at reception time. This measurement is very precise, on the order of millimeters [19].

Since the phase repeats after a set period, the receiver cannot determine how many cycles have passed since the broadcast time, only the fractional phase difference at reception time. The total number of cycles that passed since the broadcast is called ambiguity, and it the major problem when using carrier phase as an observable. When the GPS receiver locks on to the GPS signal, the fractional part of the carrier phase is accurate, but carrier phase observable is given an arbitrary integer value for the ambiguity; Then, as long as the satellite is being tracked, the fractional part of the carrier phase is accumulated over time and can provide very accurate measurements after determining the initial ambiguity [19].

In an ideal, error-free situation, the carrier phase measured by a receiver r, ϕ_r, relative to satellite s is given by [19]

$$\phi_r^s = \phi_r(t) - \phi^s(t - \Delta t) + N_r^s \tag{2.25}$$

where:

- $\phi_r(r)$ is the receiver-measured carrier phase at time t
- $\phi^s(t - \Delta t)$ is the carrier phase at the time of transmission
- N_r^s is the number of whole cycles between transmission and reception, i.e. the integer ambiguity

Multiplying 2.25 by the carrier wavelength, λ, we can express phase in units of length:

$$\Phi_r^t = \lambda\phi_r^s(t) = \lambda\phi_r(t) - \lambda\phi^s(t - \Delta t) + \lambda N_r^s \tag{2.26}$$

where $\Phi_r^t(t)$ denotes the carrier phase in units of length instead of radians. From here we can use the time of propagation, Δt to define the true range to the satellite and write

$$\Phi_r^s = r + \lambda N_r^s \tag{2.27}$$

Adding all the modelled error terms, we then get the final carrier phase model

$$\Phi_r^s = r + c\delta t_r + c\delta t^s + \lambda N_r^s + T^i - I^i + MP^i + \epsilon_\phi \tag{2.28}$$

where:

- δt_r and δt^i are the receiver and satellite clock errors (in seconds)
- T^i is the tropospheric delay (in meters) between the receiver and satellite i
- I^i is the ionospheric delay (in meters) between the receiver and satellite i
- MP^i is the multipath error (in meters) between the receiver and satellite i
- ϵ_ϕ denotes any unmodelled errors in the carrier phase

Comparing with Equation 2.24, we see that the ionospheric delay in the pseudorange and carrier phase models has different signs. This is due to the ionosphere delaying the GPS signal information but advancing the carrier phase, a phenomenon known as ionospheric divergence or code-carrier divergence. While of no impact in pure pseudorange or carrier phase positioning methods, it will have an effect on positioning methods that rely on both observables [4].

Finally, one particular issue with the usage of the carrier phase observable is that, due to its dependance on an arbitrary integer N, if the receiver loses lock with the satellite it will generate a new integer ambiguity when the lock is reestablished. This phenomenon is called cycle slip, and its detection and correction is of paramount importance for any positioning methods that use the carrier phase. In the case of the single-frequency receiver, this detection is only indirect. For dual-frequency receivers, this phenomenon is much more visible and as such easier to detect and solve [4].

2.6 Dilution of Precision

The concept of Dilution of Precision (DOP) is very important in GPS navigation. In a perfect system, where the receiver and transmitter clocks are perfect and synchronized, there is no uncertainty in the position determination since only a single point is the possible solution. However, when we add uncertainties instead of a point we end up with an area of possible positions for the receiver. This area is highly dependent on the geometry of the satellite sub-constellation used by the receiver, and can significantly degrade the position solution precision. When the satellites are well spaced in the sky, the position solution precision is good, i.e. it has low DOP; However, when the satellites are close together the precision is reduced, or, more accurately, diluted, meaning this solution has high DOP.

2.7 Position accuracy measures

An important measure in any navigation system is how accurate and precise the position solutions are. This allows us to have an idea of the quality of the position solutions, as well as define safety margins to account for errors in the position solutions.

Accuracy is defined by how close an estimate is to its real value. The higher the accuracy, the closer the estimate is to its real value. This parameter is associated with observation errors. **Precision**

is a metric that quantifies the statistical variability of a measurement. A higher precision means that the measurements are close to their mean value [20].

In order to quantify the accuracy of the position solutions, several accuracy metrics were implemented, both for 2D and 3D position solutions:

2.7.1 2D accuracy metrics

Distance Root Mean Squared

One of the 2D accuracy metrics is the Distance Root Mean Squared (DRMS), which is given by

$$\text{DRMS} = \sqrt{\sigma_x^2 + \sigma_y^2} \tag{2.29}$$

where σ_x and σ_y are the standard deviations of the position solutions in the xy plane centered at the receptor and tangent to the ellipsoid. This metric corresponds to the radius of a circle centered at the true position that has 65% of the probability of the position solutions [20].

Twice Distance Root Mean Squared

The Twice Distance Root Mean Squared (2DRMS) metric is the double of the previous metric

$$\text{2DRMS} = 2\sqrt{\sigma_x^2 + \sigma_y^2} \tag{2.30}$$

and corresponds to the radius of a circle centered at the true position that contains 95% of the probability of the position solutions [20].

Circular Error Probable

The Circular Error Probable (CEP) is defined as the radius of the circle, centered at the true position, that contains 50% of all the position solutions [20].

R95

This metric is similar to the CEP, however it contains 95% of all the position solutions [20].

2.7.2 3D accuracy Metrics

Mean Radial Spherical Error

The Mean Radial Spherical Error (MRSE) is the 3D analog of the DRMS error. It is given by

$$MRSE = \sqrt{\sigma_x^2 + \sigma_y^2 + \sigma_z^2} \tag{2.31}$$

where σ_x, σ_y and σ_z are the standard deviations of the position solutions in the ECEF frame. This metric corresponds to the radius of a sphere centered at the true position that has 61% of the probability of the position solutions.

Spherical Error Probable

The Spherical Error Probable (SEP) is defined as the radius of a sphere centered at the true position that contains 50% of all the position solutions [20].

90% Spherical Accuracy Standard

The 90% Spherical Accuracy Standard (SAS90) is defined as the radius of a sphere centered at the true position that contains 90% of all the position solutions [20].

99% Spherical Accuracy Standard

The 99% Spherical Accuracy Standard (SAS99) is defined as the radius of a sphere centered at the true position that contains 99% of all the position solutions [20].

2.8 Maximum Likelihood Estimation

Since GNSS position estimates are tainted by noise, we can use statistical methods to analyse their properties and give a better estimate of the true position of a GNSS antenna.

One possible method to obtain position estimates is using Maximum Likelihood Estimation. In this method, we use the known density probability function of the measurement data, where each sample is assumed independent, conditioned by a parameter θ and a sample set, $\mathbf{x}$. From here, we can define the likelihood function, $\mathcal{L}(\theta, \mathbf{x})$, as [21]

$$\mathcal{L}(\theta|\mathbf{x}) = f_{\mathbf{X}}(\mathbf{x}|\theta) = \prod_{i=1}^{n} f_X(x_i|\theta), \quad \text{with } \theta \in \Theta \tag{2.32}$$

where:

- $f_X(\,\cdot\,|\theta)$ is the probability density function of the random variable X knowing that θ is the true value of the desired parameter
- θ represents, by convention, both the unknown parameter and the estimated parameter
- Θ is the parametric space of possible parameters

The Maximum Likelihood Estimate, $\hat{\theta}$, corresponds to the argument that maximizes the likelihood function, i.e. it is the maxima of the likelihood function:

$$\mathcal{L}(\hat{\theta}|\mathbf{x}) = \arg\max_{\theta \in \Theta} \mathcal{L}(\theta|\mathbf{x}) \tag{2.33}$$

One can also use the logarithm of the likelihood function, designated log-likelihood function

$$\ln\left[\mathcal{L}(\hat{\theta}|\mathbf{x})\right] = \arg\max_{\theta\in\Theta} \ln\left[\mathcal{L}(\theta|\mathbf{x})\right] \tag{2.34}$$

which is analitically simpler since it converts the products of Equation 2.33 into a sum of logarithms. In the case of a continuous parametric space, we can use the normal process of finding the maxima of a function. We start by finding a stationary point of the likelihood function. For a given parameter vector θ with $p > 1$ number of parameters the maximum likelihood function verifies the condition

$$\left.\frac{\partial \ln\left[\mathcal{L}(\theta_1,\ldots,\theta_p|\mathbf{x})\right]}{\partial\theta_j}\right|_{\theta=\hat{\theta}} = 0, \quad \text{with } j = 1,\ldots,p \tag{2.35}$$

Then, we check if that point is a maxima of the function. Using the concept of Hessian matrix we get [22]

$$H(\theta) = \nabla^2 \ln\left[\mathcal{L}(\theta_1,\ldots,\theta_p|\mathbf{x})\right] = h_{ij}(\theta), \quad \text{with } i,j = 1,\ldots,p \tag{2.36}$$

where

$$h_{ij}(\theta) = \frac{\partial^2 \ln\left[\mathcal{L}(\theta_1,\ldots,\theta_p|\mathbf{x})\right]}{\partial\theta_i\partial\theta_j} \tag{2.37}$$

If these conditions are verified, then $\hat{\theta}$ is the maximum likelihood estimate of the parameter vector θ. In this thesis, to compute the maximum likelihood estimate for a given distribution we will use the mle function of Matlab's Statistics and Machine Learning Toolbox, which implements an iterative version of this method for a given distribution.

Chapter 3

Position Determination

In this chapter we will give an overview of some of the methods used to determine the position of single-frequency GPS receiver using pseudoranges. It will also be introduced a smoothing method for the raw pseudorange data that uses the carrier phase to reduce noise, as well as the differential GPS method, which is the positioning method that gave motive to the creation of this thesis. Finally, even though it is not a positioning method, we introduce an augmentation system, RAIM, whose function is to detect and remove a satellite if it degrades the position solution due to satellite problems.

3.1 Least Squares

Let the satellite-receiver true range be [4]:

$$r^i = \sqrt{(x^i - x)^2 + (y^i - y)^2 + (z^i - z)^2} \tag{3.1}$$

where (x^i, y^i, z^i) are the coordinates of satellite i and (x, y, z) is the true receiver position, both in an ECEF reference frame.

We recall that the pseudorange of a GPS satellite is given by

$$\rho^i = r^i + c\delta t_r - c\delta t^i + T^i + I^i + MP^i + \epsilon_\rho \tag{2.24 revisited}$$

Assuming that the modeled errors have been removed from the pseudorange measurement, we can combine the two previous equations [23]

$$\rho^i = \sqrt{(x^i - x)^2 + (y^i - y)^2 + (z^i - z)^2} + c\delta t_r \tag{3.2}$$

where on the right side we obtain the four unknown parameters: receiver coordinates (x, y, z) and receiver clock offset δt_r. Since we have four unknown parameters, we will require at least four independent measurements to be able to determine all the unknown parameters.

Since Equation 3.2 is a non-linear equation, one possible approach to solve it is to linearize the

equation in the neighbourhood of a point. Defining an initial position estimate $\mathbf{x_0} = (x_0, y_0, z_0)$, we can apply Taylor's series expansion to the satellite-receiver range, equation 3.1, yielding [14]

$$r^i = r_0^i + \frac{x_0 - x^i}{r_0^i}\Delta x + \frac{y_0 - y^i}{r_0^i}\Delta y + \frac{z_0 - z^i}{r_0^i}\Delta z \tag{3.3}$$

where

$$\begin{cases} \Delta x = x - x_0 \\ \Delta y = y - y_0 \\ \Delta z = z - z_0 \end{cases} \tag{3.4}$$

and r_0^i is the satellite-receiver distance computed at the linearization point.

Combining equations 3.3 and 3.2, we can write the linearized pseudorange equation [14]

$$\rho^i - r_0^i = \frac{x_0 - x^i}{r_0^i}\Delta x + \frac{y_0 - y^i}{r_0^i}\Delta y + \frac{z_0 - z^i}{r_0^i}\Delta z + c\Delta t \tag{3.5}$$

Since a GPS receiver provides pseudorange measurements for several satellites, we can rewrite Equation 3.5 in matrix notation for n satellites and pseudorange measurements

$$\begin{bmatrix} \rho^1 - r_0^1 \\ \vdots \\ \rho^n - r_0^n \end{bmatrix} = \begin{bmatrix} \frac{x_0 - x^1}{r_0^1} & \frac{y_0 - y^1}{r_0^1} & \frac{z_0 - z^1}{r_0^1} & 1 \\ \vdots & \vdots & \vdots & \vdots \\ \frac{x_0 - x^n}{r_0^n} & \frac{y_0 - y^n}{r_0^n} & \frac{z_0 - z^n}{r_0^n} & 1 \end{bmatrix} \begin{bmatrix} \Delta x \\ \Delta y \\ \Delta z \\ c\delta t \end{bmatrix}, n \geq 4 \tag{3.6}$$

or, in a more compact notation

$$\mathbf{\Delta}\rho = \mathbf{H}\mathbf{\Delta}\mathbf{x} \tag{3.7}$$

where $\mathbf{\Delta}\rho$ is named the prefit-residuals vector, $\mathbf{H}$ the geometry matrix and $\Delta\mathbf{x}$ the unknown parameters vector that contains the deviations between the initial and estimated parameters. Finaly, the solution for this equation is given by

$$\mathbf{\Delta}\mathbf{x} = \mathbf{H}^{-1}\mathbf{\Delta}\rho \tag{3.8}$$

and the position estimate can be calculated by updating the initial estimate with the estimated deviations

$$\hat{\mathbf{x}} = \mathbf{x_0} + \mathbf{\Delta}\mathbf{x} \tag{3.9}$$

While the solution of Equation 3.6 is direct with four measurements, usually a GPS receiver is capable of acquiring more than four measurements, resulting in an over-determined system. To be able to solve this problem, we can use the Least Squares (LS) method. This method uses all the available measurements to find the solution that minimizes the sum of squares of the estimated residuals, i.e. solving the equation [14]

$$\hat{\mathbf{x}} = \arg\min_{\mathbf{x}} ||\Delta\rho - \mathbf{H}\mathbf{\Delta}\mathbf{x}|| \tag{3.10}$$

which results in the Least Squares solution[14]

$$\boldsymbol{\Delta}\hat{\mathbf{x}} = \left(\mathbf{H}^{\mathsf{T}}\mathbf{H}\right)^{-1}\mathbf{H}^{\mathsf{T}}\boldsymbol{\Delta}\rho \tag{3.11}$$

where $\left(\mathbf{H}^{\mathsf{T}}\mathbf{H}\right)^{-1}\mathbf{H}^{\mathsf{T}}$ is the Moore-Penrose pseudoinverse matrix. Equation 3.6 can then be linearized again around the new estimated position, and the method can be iterated until the position estimate difference is bellow a given threshold.

A diagram ilustrating this process is given in Figure 3.1.

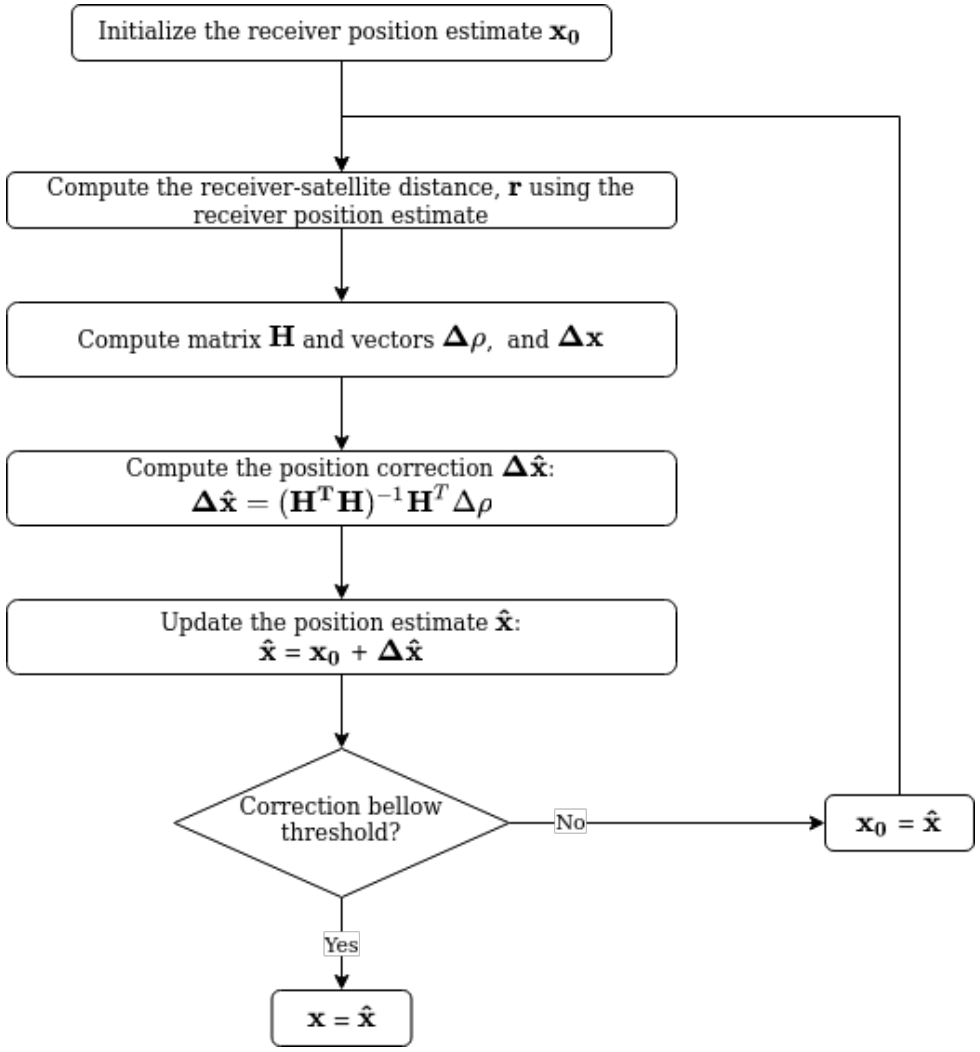

Figure 3.1: Least Squares algorithm

3.2 Weighted Least Squares

The Least Squares solution from Chapter 3.1 assumes that all the measurements' errors are independent and identically distributed, hence treating all the measurements equally. However, the satellites influence the position solution differently. For example, some might have lower elevation, which will increase the ionospheric and multipath error due to higher slant range, others might have some kind of

signal degradation in effect and transmit that information in their navigation message. In these cases, the errors are not independent and identically distributed, and as such the LS solution is not optimal [4].

In order to quantify and incorporate the measurement quality into the LS solution we can define a weighting matrix $\mathbf{Q}$, that corresponds to the inverse of the measurement error covariance matrix [24]. Applying this matrix to the LS method, we obtain the Weighted Least Squares (WLS) solution [24]

$$\mathbf{\Delta\hat{x}} = \left(\mathbf{H}^{\mathsf{T}}\mathbf{Q}\mathbf{H}\right)^{-1}\mathbf{H}^{\mathsf{T}}\mathbf{Q}\Delta\rho \tag{3.12}$$

There are several possible formulations for the measurement error covariance matrix and, subsequently, for the weighting matrix [4] [24]. For the present thesis, let us assume that the satellite measurements are uncorrelated. Consider then a diagonal matrix with diagonal elements

$$\mathbf{Q}_i i = 1/\sigma_i^2 \tag{3.13}$$

In order to give more weight to satellites with higher elevation, since they have less atmospheric and multipath errors, we can define the satellite error standard deviation, σ_i, as a function of the elevation angle. For example, a monotonous mapping function that ensures maximum weight $\mathbf{Q}_i i$ for 90° elevation and minimum weight for 0° elevation is the sin function, which entails the relationship $\mathbf{Q}_i i \propto \sin\epsilon_i$ where ϵ_i is the elevation of satellite i. One such possibility is the method described in [25] where

$$\sigma_i = \frac{\sigma_{URA_i}}{\sin\epsilon_i} \tag{3.14}$$

where σ_{URA_i} is the broadcasted User Range Accuracy for satellite i, present in the navigation message. From here, we can write the weighting matrix diagonal elements as

$$Q_i i = \frac{1}{\sigma_i^2} = \frac{\sin^2\epsilon_i}{\sigma_{URA_i}^2} \tag{3.15}$$

3.3 Extended Kalman Filter

The Least Squares methods presented in Chapters 3.1 and 3.2 are examples of single epoch measurements; they do not incorporate any information regarding previous position estimates. This is one of the major limitations of the LS methods.

One solution to this problem is the use of a recursive method to compute the position solutions. An example of such a method is the Extended Kalman Filter (EKF). This filter allows the introduction of the system dynamics to better model the receiver's states, as well as linearizing the observations model relative to the current best estimate, refining the state estimation with every new measurement. Like the LS methods, the EKF also works on the basis of the linearization of the observations model [23].

The EKF works in discrete time, t_k, and for each iteration k of the filter we have two steps:

- **Prediction**, where we estimate the state vector $\hat{\mathbf{x}}_k$ using the observations from the previous iteration,

- **Filtering**, where we estimate $\hat{\mathbf{x}}_k$ using the state vector estimate of the prediction step and the current observations.

3.3.1 Dynamics model

For the current thesis, since the problem of interest is the positioning of a static receiver, only the *P model* for the EKF will be implemented. In this model, the state vector $\mathbf{x}$ is comprised of the thre position components in an ECEF frame and two clock states representing a noise model consisting in a random walk clock frequency error plus a white noise clock drift. The complete state vector is then: [23]

$$\mathbf{x} = \begin{bmatrix} x \\ y \\ z \\ x_\phi \\ x_f \end{bmatrix} \tag{3.16}$$

Let us assume that no coupling exists between the states corresponding to the receiver position and both position and clock states are modeled by Brownian motion. For this case, the state transition matrix $\mathbf{\Phi}$ is given by [23]

$$\Phi = \begin{bmatrix} 1 & 0 & 0 & 0 & 0 \\ 0 & 1 & 0 & 0 & 0 \\ 0 & 0 & 1 & 0 & 0 \\ 0 & 0 & 0 & 1 & \Delta t \\ 0 & 0 & 0 & 0 & 1 \end{bmatrix} \tag{3.17}$$

The noise covariance matrix for the continuous-time model, $\mathbf{Q}$, is block diagonal, with three identical blocks for the position states and a 2×2 submatrix for the clock model states[23]:

$$Q = \begin{bmatrix} 0 & 0 & 0 & 0 & 0 \\ 0 & 0 & 0 & 0 & 0 \\ 0 & 0 & 0 & 0 & 0 \\ 0 & 0 & 0 & q_\phi & 0 \\ 0 & 0 & 0 & 0 & q_f \end{bmatrix} \tag{3.18}$$

where the matrix elements associated with the receiver coordinates are zero since the coordinates are assumed constant for a static receiver and q_ϕ and q_f are the power spectral densities of the phase and noise white gaussian noises. These two parameters are associated with the Allan variance parameters by [26]

$$q_\phi \approx \frac{h_0}{2}$$

$$q_f \approx 2\pi^2 h_{-2}$$

These parameters characterize the clock errors over time, and are different for different kinds of oscil-

lators. For this thesis, a low-cost temperature-compensated crystal oscillator was considered, whose Allen variance parameters are assumed [26]

$$\begin{aligned} h_0 &= 2 \cdot 10^{-19} \\ h_{-2} &= 2 \cdot 10^{-20} \end{aligned} \tag{3.19}$$

From Equations 3.17 and 3.18 we can obtain the noise covariance matrix of the discrete-time dynamics dynamics model, $\mathbf{Q_k}$, as [23]

$$\mathbf{Q_k} \approx \mathbf{\Phi Q \Phi}^{\mathsf{T}} \Delta t = \Delta t \begin{bmatrix} 0 & 0 & 0 & 0 & 0 \\ 0 & 0 & 0 & 0 & 0 \\ 0 & 0 & 0 & 0 & 0 \\ 0 & 0 & 0 & c^2 \left(q_\phi + \frac{q_f \Delta t^2}{3} \right) & \frac{c^2 q_f \Delta t}{2} \\ 0 & 0 & 0 & \frac{c^2 q_f \Delta t}{2} & c^2 q_f \end{bmatrix} \tag{3.20}$$

where the clock variances where multiplied by c^2 because the clock errors are in units of meters.

3.3.2 Observations Model

The main problem with solving the pseudorange GPS navigation equations is that those equations are non-linear functions of the state variables. The EKF solves this problem by linearizing the observations model. Let us start with the observations equation [23]

$$\mathbf{z_k} = \mathbf{h}\left[\mathbf{x}(t_k)\right] + \mathbf{v}_k \tag{3.21}$$

where $\mathbf{z}_k$ is the measured pseudorange vector with $n \geq 4$ observations, $\mathbf{v}_k$ the observations noise and $\mathbf{h}\left[\mathbf{x}(t_k)\right]$ is the navigation equation vector composed of n instances of Equation 3.2, i.e.

$$\mathbf{h}(\mathbf{x}) = \begin{bmatrix} \sqrt{\left(x^1 - x\right)^2 + \left(y^1 - y\right)^2 + \left(z^1 - z\right)^2} + c\delta t_r \\ \vdots \\ \sqrt{\left(x^n - x\right)^2 + \left(y^n - y\right)^2 + \left(z^n - z\right)^2} + c\delta t_r \end{bmatrix} \tag{3.22}$$

In order to linearize the navigation equations, we obtain the Jacobian matrix of 3.22. This matrix is called the observation matrix, $\mathbf{H}$, and is given by

$$\mathbf{H}_k = \left[\frac{\partial \mathbf{h}(\mathbf{x})}{\partial \mathbf{x}} \right]_{\mathbf{x}=\mathbf{x}_{\mathbf{k-1}}^+}, \tag{3.23}$$

For the P model used in this thesis, the observation matrix for n observations can be defined as

$$\mathbf{H}_k = \begin{bmatrix} a_{x_1} & a_{y_1} & a_{z_1} & 1 & 0 \\ \vdots & & & & \\ a_{x_n} & a_{y_n} & a_{z_n} & 1 & 0 \end{bmatrix} \tag{3.24}$$

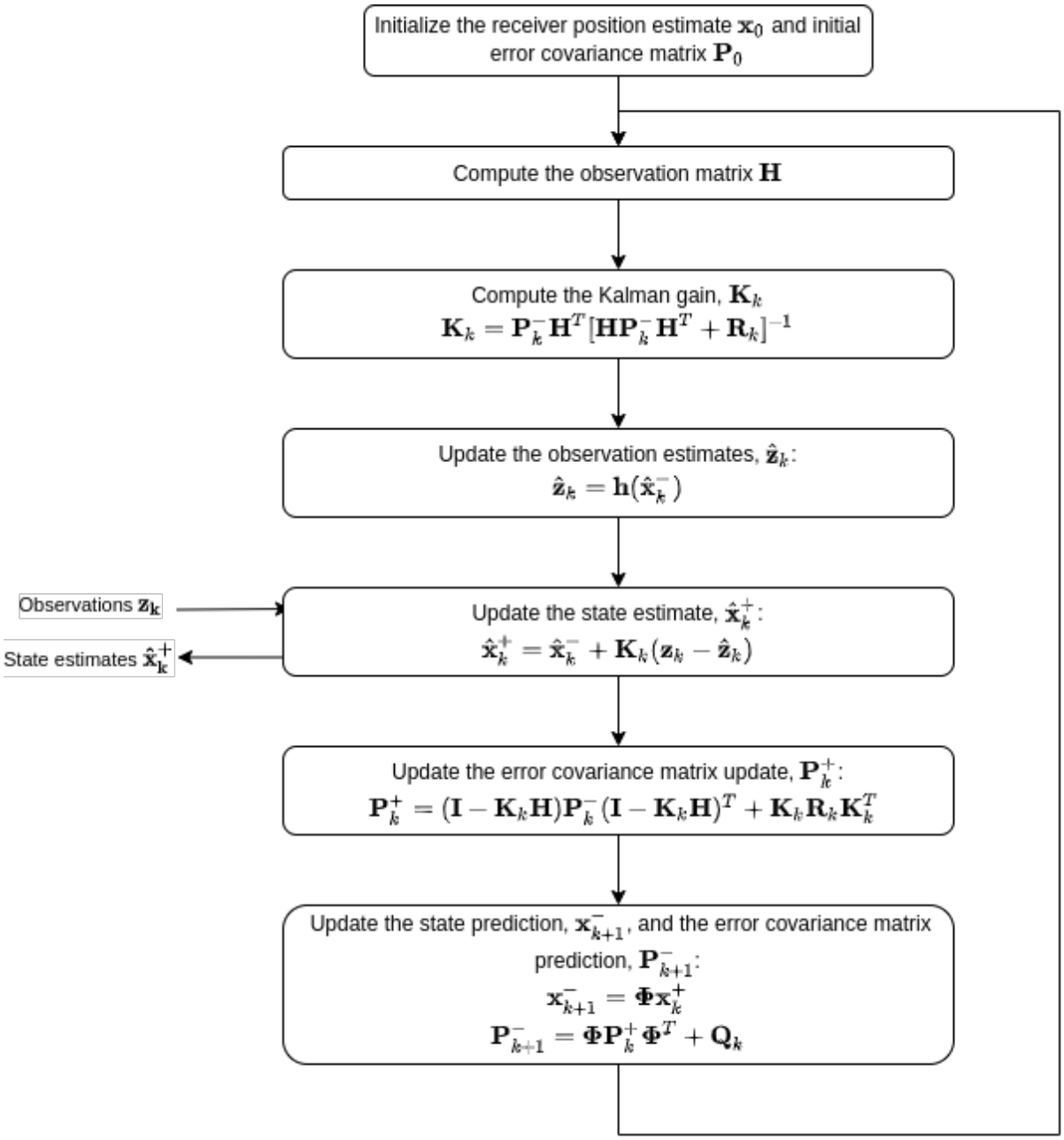

Figure 3.2: Flowchart of the EKF algorithm for GPS positioning

The elements of the observation matrix are given by

$$a_{x_i} = \frac{x^i - \hat{x}}{\hat{r}^i} a_{y_i} \quad = \frac{y^i - \hat{y}}{\hat{r}^i} a_{z_i} = \frac{z^i - \hat{z}}{\hat{r}^i} \tag{3.25}$$

where the satellite-receiver range, $\hat{r}^i$, is given by

$$\hat{r}^i = \sqrt{(x^i - \hat{x})^2 + (y^i - \hat{y})^2 + (z^i - \hat{z})^2} \tag{3.26}$$

Finally, the last observation model parameter is the observation noise covariance matrix, $\mathbf{R}_k$, which

is a $n \times n$ diagonal matrix given by

$$\mathbf{R}_k = \begin{bmatrix} \sigma_1^2 & & \mathbf{0} \\ & \sigma_2^2 & \\ & & \ddots \\ \mathbf{0} & & \sigma_n^2 \end{bmatrix} \tag{3.27}$$

3.3.3 Algorithm

Having obtained all the parameters necessary to the computation of the EKF, we then proceed to the implementation of the EKF algorithm, which is presented in Figure 3.2 [23] [27]. This filter must be initialized with an initial position estimate, $\mathbf{x}_0$ and error covariance matrix $\mathbf{P}_0$.

3.4 Unscented Kalman Filter

Another possible implementation of the Kalman Filter for a non-linear system is the Unscented Kalman Filter (UKF). This method differs from the EKF in that, instead of linearizing the non-linear system around a single point, we calculate the statistics of the random variables (RV), assumed as gaussian, to approximate the state distribution of a non-linear function [28]. As such, the differences between the UKF and EKF models will be in the observations model, with the matrices and vectors that correspond to the dynamics model being the same as Equations 3.16, 3.17 and 3.20, and the observation noise covariance matrix being the same as 3.27.

3.4.1 Unscented Transform

Let us define a non-linear function $\mathbf{f}(\mathbf{x}_k)$, where $\mathbf{x}$ is a vector of random variables with an expected value, i.e. mean, $\hat{\mathbf{x}_k}$ and covariance matrix $\mathbf{P}_k$. The Unscented Transform (UT) of this function consists in taking a set of samples from the random variable $\mathbf{x}_k$, applying the non-linear function to this set of points and then obtain a new set of statistics for the transformed random variable. Since we assumed the random variable as gaussian, the random variable obtained from the transformation will also be gaussian.

The points used in the UT are called sigma points, and together form the sigma vector, $\mathcal{X}$. For a given iteration k, these points are given by [28]

$$\begin{aligned} \mathcal{X}_{0,k} &= \hat{x}_k \\ \mathcal{X}_{i,k} &= \hat{x}_k + \sqrt{n+\tau}\left(\sqrt{\mathbf{P}_k}\right)_i \qquad \text{with } i = 1, \ldots, n \\ \mathcal{X}_{i+n,k} &= \hat{x}_k - \sqrt{n+\tau}\left(\sqrt{\mathbf{P}_k}\right)_i \end{aligned} \tag{3.28}$$

where

- n is the size of $\mathbf{x}$

- τ is the scale factor of the sampling
- $\left(\sqrt{P_k}\right)_i$ designates the i-th line of $\sqrt{P_k}$

The sigma vector that arises is a matrix of $n \times (2n+1)$, where each line is a set of sigma points for a given element of $\mathbf{x}_k$. The matrix $\sqrt{P_k}$ is the solution of the equation

$$\mathbf{P}_k = \sqrt{\mathbf{P}_k}\sqrt{\mathbf{P}_k}^{\mathsf{T}} \tag{3.29}$$

which can be obtained using the Cholesky decomposition [28]. The scaling factor τ is used to adjust the spacing between sample points and their weight in the statistics of the transformation, and can be either positive or negative. For the simmetrical sampling case, we can write [28]

$$n + \tau = 3 \tag{3.30}$$

After this sampling, the sigma points are propagated through the non-linear function $\mathbf{f}$

$$\mathcal{Y}_i, k = \mathbf{f}\left(\mathcal{X}_{i,k}\right) \qquad \text{with } i = 0, \ldots, 2n \tag{3.31}$$

And then the statistics of the resulting vector can be obtained by means of a weighted average [28], from which we can determine the mean and covariance matrix

$$\begin{aligned} \hat{\mathbf{y}_k} &= \sum_{i=0}^{2n} W_i \mathcal{X}_{i,k} \\ \mathbf{P}_{yy} &= \sum_{i=0}^{2n} W_i \left(\mathcal{Y}_{i,k} - \hat{\mathbf{y}_k}\right)\left(\mathcal{Y}_{i,k} - \hat{\mathbf{y}_k}\right)^{\mathsf{T}} \end{aligned} \tag{3.32}$$

where the weight values W_i are given by

$$\begin{aligned} W_0 &= \frac{\tau}{n+\tau} \\ W_i &= \frac{1}{2\left(n+\tau\right)} \end{aligned} \tag{3.33}$$

3.4.2 Algorithm

With the results of the UT, we can now rework the Kalman Filter to include those results and compute the position solution. The resulting algorithm is presented in Figure 3.3 [28]. Like the EKF, this method must also be initialized with an initial position estimate, $\mathbf{x}_0$ and error covariance matrix $\mathbf{P}_0$.

3.5 Carrier-Smoothed Code - the Hatch Filter

Up until now, the only observable that was considered for the positioning methods was the pseudorange; however, some GPS receivers can also output the carrier phase observable. The main difference between these two is that the pseudorange presents a higher noise, but is unambiguous and can be

directly used as an observation, while the carrier phase is much more precise but is tainted by an arbitrary ambiguity which precludes its usage directly as a measurement. There are methods to determine the ambiguity problem, however they aren't trivial and even less so in the case of the single-frequency receiver studied in this thesis [4].

A simpler solution to the usage of the carrier phase observable consists in the combination of the code and carrier measurements, in range domain, to obtain a new, more precise, measurement of the pseudorange. These techniques are called Carrier-Smoothed Code (CSC). For this thesis, we will implement the Hatch Filter, a recursive method which uses time-differenced carrier phase measurements together with pseudorange measurements and appropriated weights to create a smoothed pseudorange measurement.

The time-differencing of the carrier phase measurement, in its error-free model, is given by

$$\Phi_r^s(n) - \Phi_r^s(n-1) = r_n - r_{n-1} + \lambda N_r^s - \lambda N_r^s = r_n - r_{n-1} \tag{3.34}$$

which, since the integer ambiguity N is constant and cancels-out, enables the usage of the carrier phase measurements without explicit ambiguity resolution.

We can then define the weighting factors $W(n)$ for the Hatch Filter, which are used to weight the influences of the carrier phase and pseudorange measurments in the smoothed result:

$$W(n) = W(n-1) - \gamma \tag{3.35}$$

Finally, the Hatch Filter method is given by

$$\rho_{s,k} = W(n)\rho_k + (1 - W(n))\left(\rho_{s,k-1} + \Phi_k - \Phi_{k-1}\right) \tag{3.36}$$

The weighting factor must be initialized in its first iteration, for which we use the case where only the pseudorange measurement is used:

$$W(1) = 1 \tag{3.37}$$

The parameter γ in the weighting factor formula is called the averaging constant and defines the averaging interval for the filter. Usually, it is set as 0.01 or 0.02, for a smoothing interval respectively of 100 or 50 seconds at 1Hz. Higher values of γ result in a higher smoothing [29], however it also increases the code-carrier divergence problem due to ionospheric delay [4].

One major flaw of the Hatch Filter is that whenever a cycle slip occurs the filter's result is corrupted, since there is a different integer ambiguity between two epochs. Whenever this happens, the hatch filter must be reinitialized.

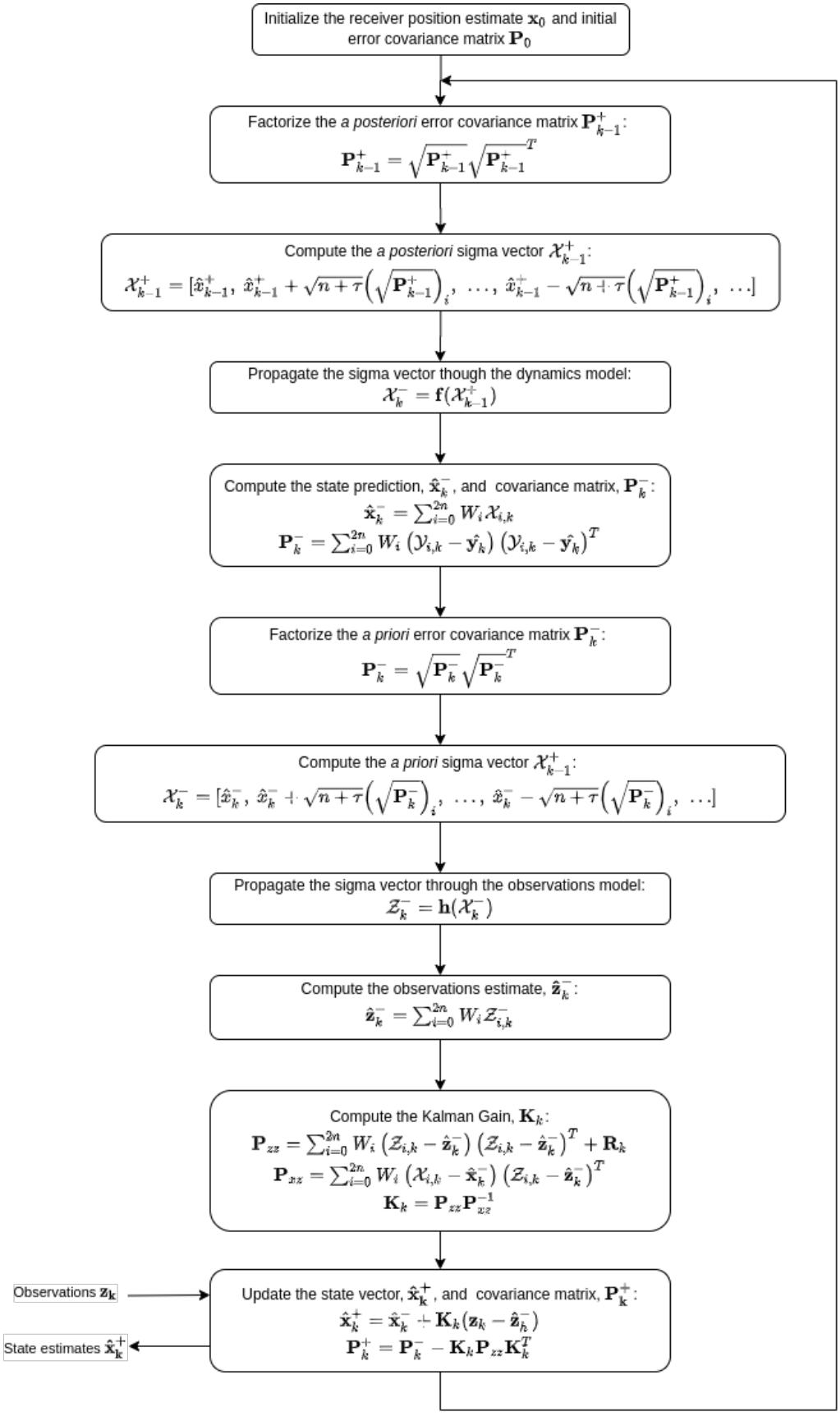

Figure 3.3: Flowchart of the UKF algorithm for GPS positioning

3.6 Differential GPS

Until now, all the methods that were discussed are single-receiver methods, however there are methods to make use of one or more reference GPS receivers to improve the position estimate of another receiver, also called rover. This method is called Differential GPS (DGPS) and explores the spatial and time correlation properties of GPS errors to signifficantly improve the positioning accuracy of a GPS receiver. However, because of this DGPS algorithms require that the rover receiver be in the vicinity of the reference receivers, with a separation of 10-200km [4].

There are three types of DGPS systems: Local-Area DGPS (LADGPS), Regional-Area DGPS (RADGPS) and Wide-Area DGPS (WADGPS). For the present thesis, only the LADGPS will be considered. There are also several methods for code-only DPGS, like position domain corrections and pseudorange domain corrections. In this thesis we will use another method, the code-equivalent GPS interferometer. This method uses double differences (DD) to compute the vector from the reference receiver to the rover receiver, and with that vector and a precise estimate of the reference receiver position we can accurately determine the position of the rover receiver.

The Code-Equivalent GPS Interferometer

Let us consider the case of two GPS receivers and a single satellite, whose configuration is presented in Figure 3.4.

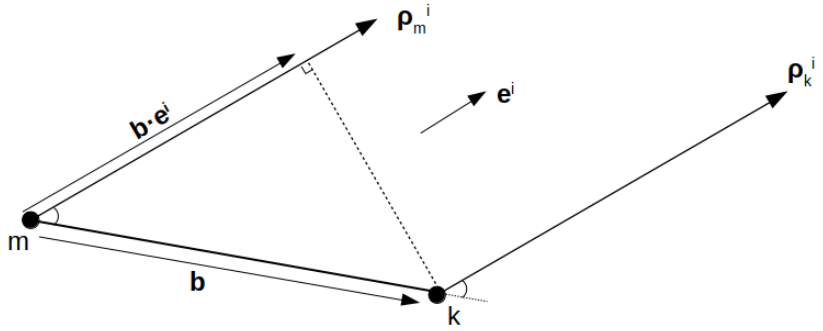

Figure 3.4: GPS interferometer configuration for one satellite

where

- m and k are, respectively, the reference and rover receivers
- ρ_j^i is the pseudorange between receiver j and satellite i
- $\mathbf{e}^i$ is the direction vector to satellite i
- $\mathbf{b}$ is the vector from the reference to rover receivers, called baseline vector
- $\mathbf{b} \cdot \mathbf{e}^i$ is the projection of $\mathbf{b}$ along the direction of $\mathbf{e}^i$

Now, consider that the distance between the receivers and satellite is much greater than the distance between receivers. In this case, the GPS satellite wave can be approximated to a planar wave at the

receivers, and we can also consider that the difference between direction vectors is negligible, hence both receivers share the same direction vector $\mathbf{e}^i$ as well as the same constellation. Finally, we also consider the case where both receivers are approximately at the same height.

Recovering the pseudorange model from Equation 2.24, we can write the pseudorange equations for the two receivers, m and k, as

$$\begin{aligned} \rho_m^i &= r_m^i + c\delta t_m - c\delta t^i + T_m^i + I_m^i + MP_m^i + \epsilon_{\rho,m}^i \\ \rho_k^i &= r_k^i + c\delta t_k - c\delta t^i + T_k^i + I_k^i + MP_k^i + \epsilon_{\rho,k}^i \end{aligned} \tag{3.38}$$

By differentiating the pseudorange measurements pertaining to the same satellite between both receivers we can cancel the common satellite clock bias term. Also, since we are working on a local area, the baseline is small and as such we can assume that the ionospheric error for both receivers is equal and cancel out those terms. Since we also assumed that the receivers where roughly at the same altitude, the tropospheric error can be assumed equal for both receivers and also cancels out. The resulting difference is called the Single Difference (SD) and is given by (where receiver m was considered the reference receiver):

$$SD_{km}^i = \rho_k^i - \rho_m^i = r_{km}^i + c\delta t_{km} + \epsilon_{\rho,km}^i \tag{3.39}$$

where the subscript km represents the difference between receiver k and m for each parameter.

From Equation 3.39, we can see that SD_{km}^i corresponds to the distance travelled by the GPS signal during the reception time difference between receiver k and m. From Figure 3.4, it is clearly seen that this distance corresponds to the value of the SD between both receivers, i.e.

$$SD_{km}^i = \mathbf{b} \cdot \mathbf{e}^i \tag{3.40}$$

Expanding on the single satellite interferometer, let us add a second satellite, j. This configuration is presented in Figure 3.5.

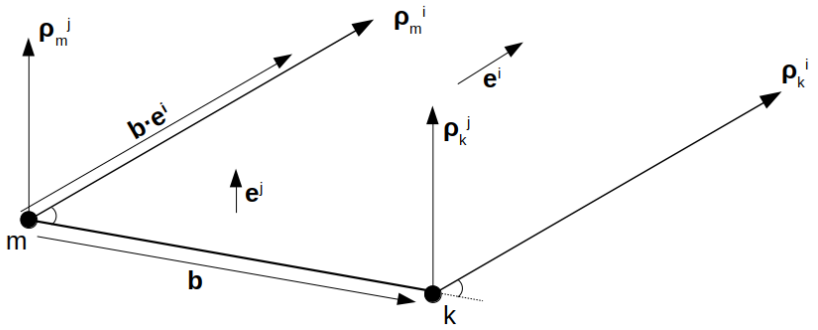

Figure 3.5: GPS interferometer configuration for two satellites

We can apply Equation 3.39 for this second satellite and obtain a new SD:

$$SD^j_{km} = \rho^j_k - \rho^j_m = r^j_{km} + c\delta t_{km} + \epsilon^j_{\rho,km} \quad = \mathbf{b} \cdot \mathbf{e}^j \tag{3.41}$$

By differencing these two SD, we can cancel out the receiver clock bias errors for both receivers. This new difference is called Double Difference and is given by:

$$DD^{ij}_{km} = SD^i_{km} - SD^j_{km} = r^{ij}_{km} + \epsilon^{ij}_{\rho,km} \tag{3.42}$$

where the superscript ij denotes between which satellites the difference is taken. We can also apply the DD to Equation 3.40 to obtain the relationship between the DD and the baseline vector:

$$DD^{ij}_{km} = \mathbf{b} \cdot \mathbf{e}^i - \mathbf{b} \cdot \mathbf{e}^j = \mathbf{b}(\mathbf{e}^i - \mathbf{e}^j) = \mathbf{b} \cdot \mathbf{e}^{ij} \tag{3.43}$$

For this interferometer, the DD are all taken in relation to the same satellite. In this case, the satellite with highest elevation is taken as the reference satellite from which all the DD are computed, since this satellite will be, most likely, the one less affected by atmospheric and pseudorange errors. Combining Equations 3.42 and 3.43 for n satellites we obtain the system

$$\begin{bmatrix} DD^{12}_{km} \\ DD^{13}_{km} \\ \vdots \\ DD^{1n}_{km} \end{bmatrix} = \begin{bmatrix} e^{12}_x & e^{12}_y & e^{12}_z \\ e^{13}_x & e^{13}_y & e^{13}_z \\ \vdots & \vdots & \vdots \\ e^{1n}_x & e^{1n}_y & e^{1n}_z \end{bmatrix} \begin{bmatrix} b_x \\ b_y \\ b_z \end{bmatrix} + \begin{bmatrix} \epsilon^{12}_{km} \\ \epsilon^{13}_{km} \\ \vdots \\ \epsilon^{1n}_{km} \end{bmatrix} \tag{3.44}$$

which can be written in a more compact notation as

$$\mathbf{y} = \mathbf{B} \cdot \mathbf{b} + \mathbf{e} \tag{3.45}$$

where $\mathbf{y}$ is the measured pseudorange DD vector, $\mathbf{B}$ is the matrix of the components of the differenced direction vectors, $\mathbf{b}$ is the baseline vector and $\mathbf{e}$ is the measurement noise vector.

The baseline vector can then be determined using for example a Least Squares method or a Kalman Filter. In this case, we implemented a very simple Kalman Filter with

$$\begin{aligned} \mathbf{x} &= \mathbf{b} \\ \mathbf{\Phi} &= \mathbf{I}_3 \\ \mathbf{Q} &= \mathbf{0}_{3\times 3} \\ \mathbf{H} &= \mathbf{B} \end{aligned} \tag{3.46}$$

and whose algorithm is presented in Figure 3.6.

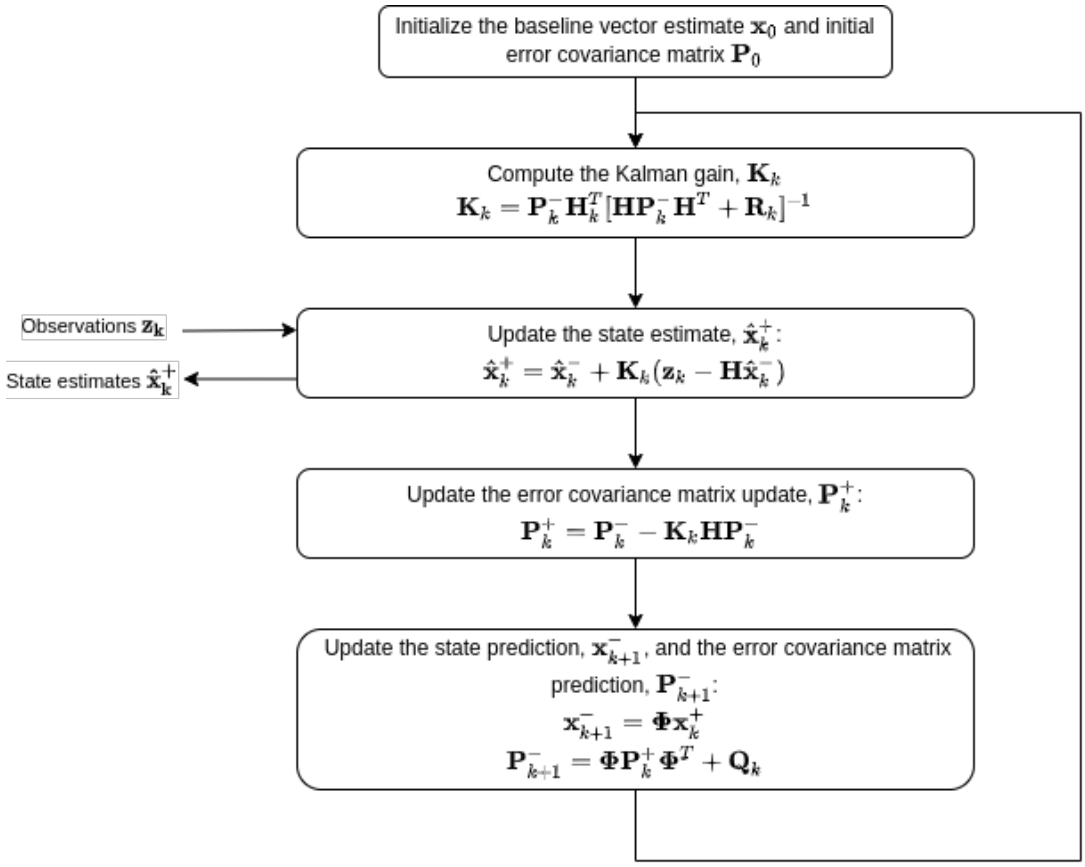

Figure 3.6: Flowchart of the basic KF algorithm

3.7 RAIM

As a final topic in position determination, we will introduce the concept of RAIM. The Receiver Autonomous Integrity Monitoring (RAIM) techniques allow a GPS receiver to detect instances where a faulty satellite or faulty measurement will degrade the position solution considerably, and provide the receiver with integrity information so that the receiver can be aware of possible position solution degradation and act accordingly [4]. While RAIM isn't directly responsible for position determination, this integrity augmentation is relevant even for a static receiver, hence the introduction in this thesis, albeit in a more simplified fashion.

Most of the RAIM algorithms follow the following generic sequence of steps given a navigation solution [30]:

1. Use a detection parameter, the test statistic, to detect the presence of a fault
2. Use the expected system noises and test statistic relationship to describe a faulty measurement
3. Establish a detection threshold based on the desired probability of false alarm
4. Obtain the test statistic for each observation and perform the fault detection
5. If there are detected faults, apply some method to isolate the faulty satellite
6. Compute the protection levels (optional)

While several RAIM algorithms exist [31], in this thesis we will only focus on the conventional RAIM techniques. In these techniques, there are several methods can be employed for fault detection, like Least Squares Residuals (LSR) [30], Total Least Squares (TLS) [32], Range Comparison [30], etc. In this thesis we will only use the LSR method. Also, since we are using a static receiver without any need for a safety envelope, the protection levels will not be calculated.

3.7.1 Fault detection and handling of conventional RAIM

In conventional RAIM, there are two main algorithms: Fault Detection (FD) and Fault Detection and Exclusion (FDE).

Fault Detection

This algorithm is responsible for checking for anomalies in the received measurements. Requiring at least 5 satellites, it will divide the visible constellation into N subsets of $N-1$ satellites, where N is the number of satellites in the visible constellation. Afterwards, it applies the test statistic to identify which subset of satellites is the one that doesn't have anomalies and provides information on the faulty satellite to the receiver. For the case of $N = 5$, this algorithm is merely informative, since, without an extra satellite, there is no redundancy to be able to apply the next algorithm, FDE.

Fault Detection and Exclusion

The FDE algorithm is the logical consequence of the FD algorithm when $N > 5$. This algorithm excludes one satellite from each subset fo $N-1$ satellites and repeats the FD algorithm, allowing for correct identification of the faulty satellite and its exclusion from the measurements. This method allows the receiver to continue to operate nominally even in the presence of faulty satellites, as long as there are enough satellites visible to satisfy the FDE requirements

3.7.2 Least Squares Residuals

For a set of pseudorange measurements, the Least Squares solution from Chapter 3.1 is given by Equation 3.11:

$$\boldsymbol{\Delta}\hat{\mathbf{x}} = \left(\mathbf{H}^{\mathsf{T}}\mathbf{H}\right)^{-1}\mathbf{H}^{\mathsf{T}}\boldsymbol{\Delta}\rho \tag{3.11 revisited}$$

Using the incremental model of Equation 3.7, we can obtain an estimate of the prefit-residuals vector for the newly computed position correction:

$$\boldsymbol{\Delta}\hat{\rho} = \mathbf{H}\boldsymbol{\Delta}\hat{\mathbf{x}} \tag{3.47}$$

From these results, we can calculate the range residuals, $\mathbf{w}$ [33]:

$$\mathbf{w} = \boldsymbol{\Delta}\rho - \boldsymbol{\Delta}\hat{\rho} = \boldsymbol{\Delta}\rho - \left(\mathbf{H}^{\mathsf{T}}\mathbf{H}\right)^{-1}\mathbf{H}^{\mathsf{T}}\boldsymbol{\Delta}\rho \tag{3.48}$$

To be able to do fault detection, some error metric must be used in order to obtain the test statistic. The range residuals provide us with information about the difference between the computed and expected pseudorange measurements, however its nature as a vector doesn't lend itself to an easy comparison with a test statistic. To solve this, we can use the sum of squared errors, SSE, which provides a scalar value that can be easily used to compute the test statistic:

$$SSE = \mathbf{w}^{\mathsf{T}}\mathbf{w} \tag{3.49}$$

And finally, we can compute the test statistic, given by [33]

$$t = \sqrt{\frac{SSE}{n-4}} \tag{3.50}$$

where n is the number of satellites used in the FD algorithm.

If the measurment errors of the pseudoranges are independent and normally distributed random variables with zero mean, then SSE is chi-squared distributed with $n-4$ degrees of freedom. Consequently, the test statistic t will also be chi-squared distributed with $n-4$ degrees of freedom. This statistic, in the case of a fault, will become a non-central chi-squared distribuition with $n-4$ degrees of freedom [34]. With this information, we can define a detection criteria based on a detection threshold, λ, which performs a simple binary decision:

$$\begin{cases} t \geq \lambda \rightarrow \text{Fault} \\ t < \lambda \rightarrow \text{No fault} \end{cases}$$

The detection threshold is dependent on the false alarm probability, P_{fa}, and the number of visible satellites, n. Given those values, we can compute the detection threshold by inverting the incomplete gamma function [34]

$$1 - P_{fa} = \frac{1}{2^a \Gamma(a)} \int_0^{\lambda^2} e^{-\frac{s}{2}} s^{a-1} ds \tag{3.51}$$

where $a = (n-4)/2$ and the gamma function is given by

$$\Gamma(x) = \int_0^{\infty} e^{-t} t^{x-1} dt \text{ , with } x \in \mathbb{R}^+ \tag{3.52}$$

A flowchart of the RAIM algorithm used in this thesis is presented in Figure 3.7. Do note that, since the FDE is always applied whenever there are more than 5 satellites, the division of the visible satellites in subsets was merged in the FDE section of the algorithm.

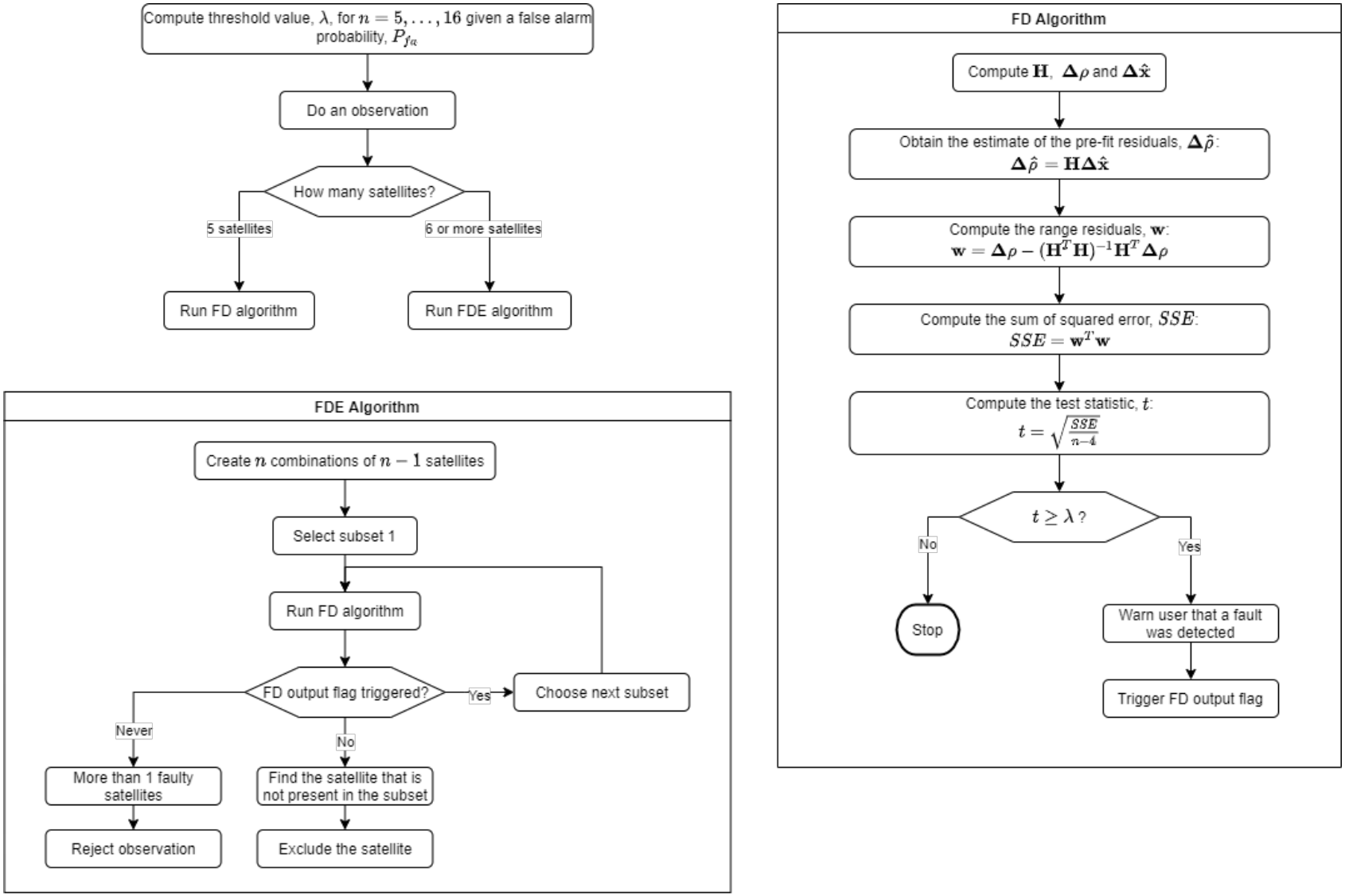

Figure 3.7: Flowchart of the RAIM algorithm

Chapter 4

Precise Positioning

Up until now, we only discussed positioning methods that rely solely on the data provided by the receiver or, in the case of differential GPS, another receiver in the vicinity. As such, these methods are only as accurate as the data they receive. However, it is possible to obtain better data, like precise orbital ephemeris and clock data, from external sources to improve the performance of the positioning methods. In this section, we will give an overview of the International GNSS Service and its products, as well as one method of precise positioning, called Precise Point Positioning.

4.1 International GNSS Service

The International GNSS Service (IGS) was established by the International Association of Geodesy in 1993, with the goal of supporting geodetical and geophysical research. To this end, the IGS is responsbile for standards and specifications, as well as providing GNSS data and products [4]. Several GNSS tracking stations around the world provide accurate GNSS data to the IGS, which is then used to create very accurate measurements of several parameters of GNSS satellites, which then are provided to the public free of charge. These parameters, bundled in so-called GNSS products, are [35]:

- Precise orbital ephemeris
- Precise clock data
- Earth orientation parameters
- Ionospheric and tropospheric parameters
- Differential code biases
- Antenna phase center corrections

and can be obtained from the IGS products page: `https://www.igs.org/products-access/`.

In this thesis we will focus on the precise orbit and clock products for the GPS satellites, as well as the ionospheric products and antenna phase center corrections.

Precise orbit and clock products for GPS satellites

These products are provided to end-users in three varieties, differing in their latency and accuracy:

- **Ultra-Rapid products** are provided four times a day, and consist in predicted and observed products. The predicted part can be used in real time, while the observed part is available every 3 - 9 hours. These products have an accuracy of 3 - 5 cm for orbital products and 0.15 - 3 ns for the clock products
- **Rapid products** have a latency of 17 - 41 hours, and provide an accuracy of 2.5 cm for orbital products and 0.075 ns for clock products
- **Final products** are the highest precision available products, with a latency of 12- 18 days and provide slightly better accuracy than the rapid products

As can be seen from the product latency, only the ultra-rapid products, in their predicted form, can be used for real-time positioning methods. However, the other products can still be used for receiver data post-processing, with significantly better results than the predicted ultra-rapid products.

Ionospheric products

Since the IGS has available a large number of GNSS receivers capable of multi-frequency operation, it can use those receivers to compute the ionospheric delay, which is then used to create a map of the concentration of free electrons in the ionosphere, the Vertical Total Electron Content (VTEC) map. This map is then converted to a receiver-independent data format, IONEX, which can then be shared with IGS users worldwide. [35].

These ionospheric products are available daily, for the rapid products, after 9 - 10 days for the predicted solution of the final product, and after approximately 11 days for the final product.

Antenna phase center corrections

Another product that is available from the IGS are the antenna phase center corrections. The GPS satellite's force models, that are used to model its orbit, are referenced to the satellite's center of mass, hence the IGS orbit and clock products are also refered to the satellite's center of mass. However, the pseudorange and carrier phase measurements are taken with relation to the satellite's antenna phase center, creating an offset. To correct this offset, the IGS compiled a list of offsets for each GPS satellite, which is provided in the same way as the IGS products [36].

4.2 Precise Point Positioning

The Precise Point Positioning is a very precise processing model for GPS data that does not require the usage of nearby reference stations. This positioning method is similar to the point positioning methods

of Chapter 3, but instead of the navigation message broadcast data it uses precise orbital and clock products combined with additional error modeling to compute the position solution.

While PPP methods weren't used for obtaining positioning solutions in this thesis, this method was employed to obtain precise estimations of the static GPS antennas as reference positions. To this end, the software *RTKLIB* [37], from Tomoji Takasu of the Tokyo University of Marine Science and Technology was used. This is popular open-source software for precise positioning, capable of using several different positioning methods for position determination as well as providing a single-stop solution for DGNSS and Real-Time Kinematics (RTK) measurements. For PPP positioning, this software uses the EKF in conjunction with the PPP methods to obtain precise positioning solutions for a fixed receiver [38].

In the present thesis, the following settings were used for the PPP positioning using RTKLIB, based on [39]:

- Static positioning mode, PPP-Static
- Forward filtering only
- GDOP threshold of 30
- Elevation mask angle of 10^{o}
- Earth tides correction enabled
- Ionosphere corrections using IONEX file for single-frequency receivers and ionosphere-free model for double-frequency receivers
- Troposphere correction using the Saastamoinen model
- Precise satellite ephemeris and clocks using IGS data
- Satellite phase center corrections enabled, to correct the difference between the center of mass position, used in the ephemeris, and the phase center of the GPS antenna array
- Phase wind-up corrections enabled, to account for the delay caused by relative rotation between satellite and receiver antennas
- GPS Block IIA satellites are excluded when in eclipse conditions
- RAIM FDE is activated to detect and remove faulty measurements
- Integer ambiguity resolution enabled, using the PPP-AR mode

This combination of settings allows the correction of most of the GPS measurement errors with great precision. However, it should be noted that the receiver antenna phase center correction was not used due to lack of correction data for the antennas used in this thesis.

Chapter 5

Experimental Results

In this chapter, the experimental methods and results are summarily described. We start by describing the problem that gave origin to this thesis and the experimental setup, and then present the various experimental results and their analysis, which are used to draw the conclusions for this thesis.

5.1 Problem Description

As stated in Chapter 1.3, the main goal of this thesis is to compare position estimation methods for a static receiver in order to provide a possible end-user with information on what method he should use for a given application. To this end, we are comparing several positioning methods and also adding data pre-processing (Hatch Filter, RAIM) and post-processing (in the form of statistical analysis) methods to the experimental results. These results will also be compared regarding how long they take to obtain a certain accuracy. This analysis is especially useful for end-users who might be interested more in having a quick but relatively accurate position for their base station instead of a very precise, almost geodetic-quality, measurement for, for example, usage with a DGPS or RTK setup for drone positioning. Finally, the results obtained will be applied to two DGPS setups, in order to validate their effectiveness.

5.2 Experimental Setup

Data collection for this thesis was done using two different types of receivers, as well as different antennas and some processing software. All the receivers were connected to a laptop computer which provided both serial communication handling and Internet Protocol (IP) communication. A more in-depth explanation of the procedure can be found in Annex B.

5.2.1 Receivers

Since this thesis is designed around the idea of lowering the cost-barrier for a DGPS base station, the main receivers used were relatively low-cost receivers from u-blox. However, a higher-end Ashtech

receiver was used in order to allow comparison of the developed algorithms with a more expensive, high-precision receiver.

u-blox 6T

The main receiver used was the U-Blox 6T Evaluation Kit. This receiver is a L1-only capable receiver, which was designed for both static and dynamic applications and can output raw observation data [40]. Its low-cost makes it a very compelling receiver for our objective, and provides a good baseline for what a cheaper but high quality receiver is capable. This receiver is also capable of tracking SBAS satellites, however, in order to comply with this thesis' objective those functionalities where not used. Communication with this receiver is done in the form of serial communication.

Figure 5.1: u-blox EVK 6T Receiver

Ashtech ProFlex 500

This receiver is a high-end GNSS receiver, capable of receiving both GPS and GLONASS signals on both L1 and L2 frequencies [41]. This is a survey-grade receiver, capable of providing not only PVT solutions but also work as a standalone base-station without need for external processing equipment. This receiver not only provides serial communication with a computer, but can also work as a web-server for configuration and data transmission over IP, as well as providing integrated data logging methods.

Figure 5.2: Ashtech ProFlex 500 Receiver

5.2.2 Antennas

For this thesis, the antennas on the roof of the North Tower of Instituto Superior Técnico were used. This allowed long surveys to be performed, which then were used for the precise determination of the antenna position.

NovAtel GPSAntenna Model 521

These antennas, used for the fixed u-blox receivers, are L1 active antennas with an integrated 26 dB preamplifier [42]. In their current installation at the top of the IT GNSS lab, they were fitted with a choke ring to reduce multipath effects.

Figure 5.3: NovAtel GPSAntenna Model 521 GNSS antenna

ProFlex 500 Survey Antenna - AT1675-7M

This dual-frequency L1/L2 antenna, which is connected to the ProFlex 500 receiver, is an active antenna with a 38dB integrated preamplifier. Like the previous antenna, it is also installed at the top of the IT GNSS lab and fitted with a choke ring.

5.2.3 Software

Since different GPS receivers were used, there were also different software involved in the capture of the observation data.

u-blox u-center

For the u-blox receivers, observation data was captured using the proprietary *u-center* software. This software creates a log of the serial data sent by the receiver during the capture and outputs it as a proprietary .ubx file. Since this file is proprietary and uses proprietary messages for the raw receiver data, additional processing is required before using the data in our algorithms.

ProFlex 500 web interface

In the case of the ProFlex 500, the observation data was logged by the receiver itself using its built-in data logger. This data was saved to a file with proprietary message formats, and then converted to a

RINEX 3.01 format using the built-in converter.

RTKLIB

This software, introduced in Section 4.2, is also capable of converting the proprietary .ubx file into a RINEX file, which can then be used by the developed software. Another capability is the manipulation of RINEX files, for which it was also used in the present thesis. In this thesis version 2.4.2 of this software was used to obtain PPP solutions, with version 2.4.3 Beta 33 used for the u-blox to RINEX data conversion.

GFZRNX - RINEX GNSS Data Conversion and Manipulation Toolbox

The software GFZRNX [43], developed by Thomas Nischan from the German Research Centre for Geosciences in Potsdam, Germany, is a RINEX manipulation program. In this thesis, it was used to compile several RINEX files containing 1h of data into a contiguous, 24h data set.

5.3 Antenna reference position determination

In GNSS systems, the accuracy of a positioning method and/or system is measured by the error between the computed position of the antenna and its true position, both in the same reference frame. This raises one of the most important questions in GNSS: what is the true position of a GNSS antenna? Since GNSS systems are haunted by the ever-present noise, any measurement will always have some offset from the true position. However, by collecting measurements over a long time, we can somewhat cancel out these errors by averaging them over that period of time, making use of the so called ”Law of Large Numbers”.

As such, the reference position for the antennas used in this thesis is obtained by that same approach: we compute the position solution over a large number of epochs, and then average their results. The resulting position is then very close to the actual true position. However, this approach is only as precise as the data it is provided. If the data has a very large expected error, then it might take much longer for those errors to cancel out. To solve this, the reference position determination will use the PPP method described in Chapter 4, with the methodology described in Section 4.2.

5.3.1 Reference Station antenna position

The first antenna whose reference position we will obtain is the antenna that has been used for all the auto-surveying methods. This antenna, which has assigned the code RF2 in the IT GNSS Lab [44], is attached to one of the u-blox EVK-6T receivers. A continuous logging of the observations was done for an entire GPS week, starting at midnight of 25/10/2020 and ending at 23:59:59 of 31/10/2020, for a total of 604800 observed epochs. The data capture was started slightly before midnight to allow the receiver to obtain the complete navigation message of all visible satellites and the full almanac data.

These observations were then split into 24h blocks and processed using RTKLIB. The reason for this split is that, while newer versions of RTKLIB can work with multiple days' worth of IGS products, it deprecated the implementation of PPP for single-frequency observations. As such, the data was processed using RTKLIB version 2.4.2, which has support for single-frequency PPP solutions but can only work with a single file for each IGS product. Finally, the average position solution for each day was collected, and the seven position solutions were averaged again, to produce a more accurate measurement. The position solution obtained for each day, as well as the average position, are presented in Table 5.1, and the scatterplot of the position solutions for the first day is presented in Figure 5.4.

Day	**X (m, ECEF)**	**Y (m, ECEF)**	**Z (m, ECEF)**
1	4918525.6298	-791212.1063	3969762.2795
2	4918525.4783	-791212.1159	3969762.2795
3	4918525.6004	-791212.0766	3969762.2795
4	4918525.6046	-791212.0488	3969762.2795
5	4918525.3394	-791211.8449	3969762.0718
6	4918525.4199	-791212.0304	3969762.1318
7	4918525.5907	-791211.9873	3969762.2616
Average	4918525.5233	-791212.0300	3969762.2262

Table 5.1: PPP position results for RF2

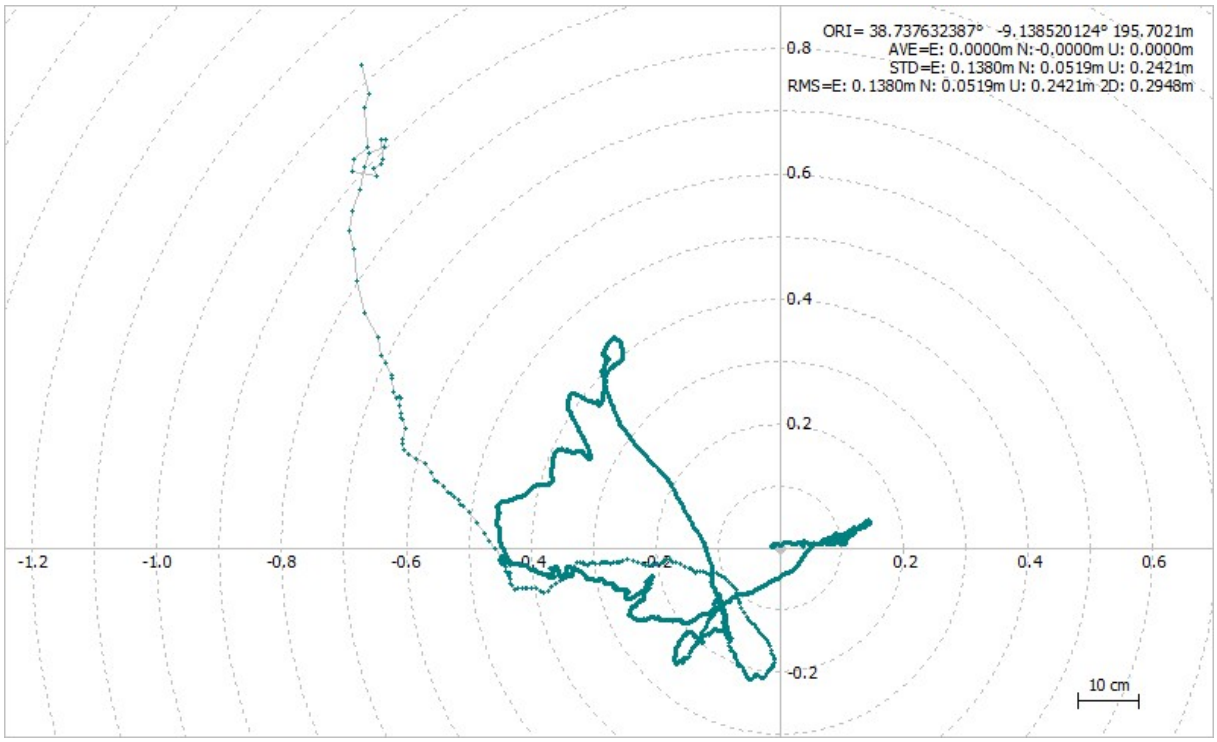

Figure 5.4: Scatterplot of PPP position results for RF2 (day 1)

As we can see, the PPP method has decimeter-level precision, and provides a very well bounded

result for the receiver position, with very small standard deviations and low-decimeter-level RMS error. These results are very good for a single-frequency receiver, which cannot completely resolve the ionospheric error due to only having a single frequency band, even with external ionospheric data, and as such it is safe to say it is the current best estimate of the antenna position.

5.3.2 Fixed Rover antenna position

Since the IT GNSS Lab has several fixed antennas, it is logic to use another of those antennas as a rover to validate the positioning methods since, as they are static antennas, long-term surveys can easily be done. This second antenna, designated RF6, is also attached to a u-blox EVK-6T receiver. A similar survey to the one of Section 5.3.1 was done, with the same duration and time-frame. The resulting position estimate is given in Table 5.2, and the scatterplot of the position solutions for the first day is presented in Figure 5.5.

Day	X (m, ECEF)	Y (m, ECEF)	Z (m, ECEF)
1	4918532.2224	-791212.5657	3969754.7410
2	4918532.1333	-791212.5816	3969754.7042
3	4918532.2288	-791212.4954	3969754.8402
4	4918532.2064	-791212.5560	3969754.8305
5	4918531.9371	-791212.4515	3969754.5903
6	4918531.9778	-791212.4947	3969754.6181
7	4918532.1256	-791212.5403	3969754.7366
Average	4918532.1188	-791212.5264	3969754.7230

Table 5.2: PPP position results for RF6

While the initial results present meter-level error, the strong convergence after an initial phase is clearly seen in this result, where the average position is not very affected by this initial error.

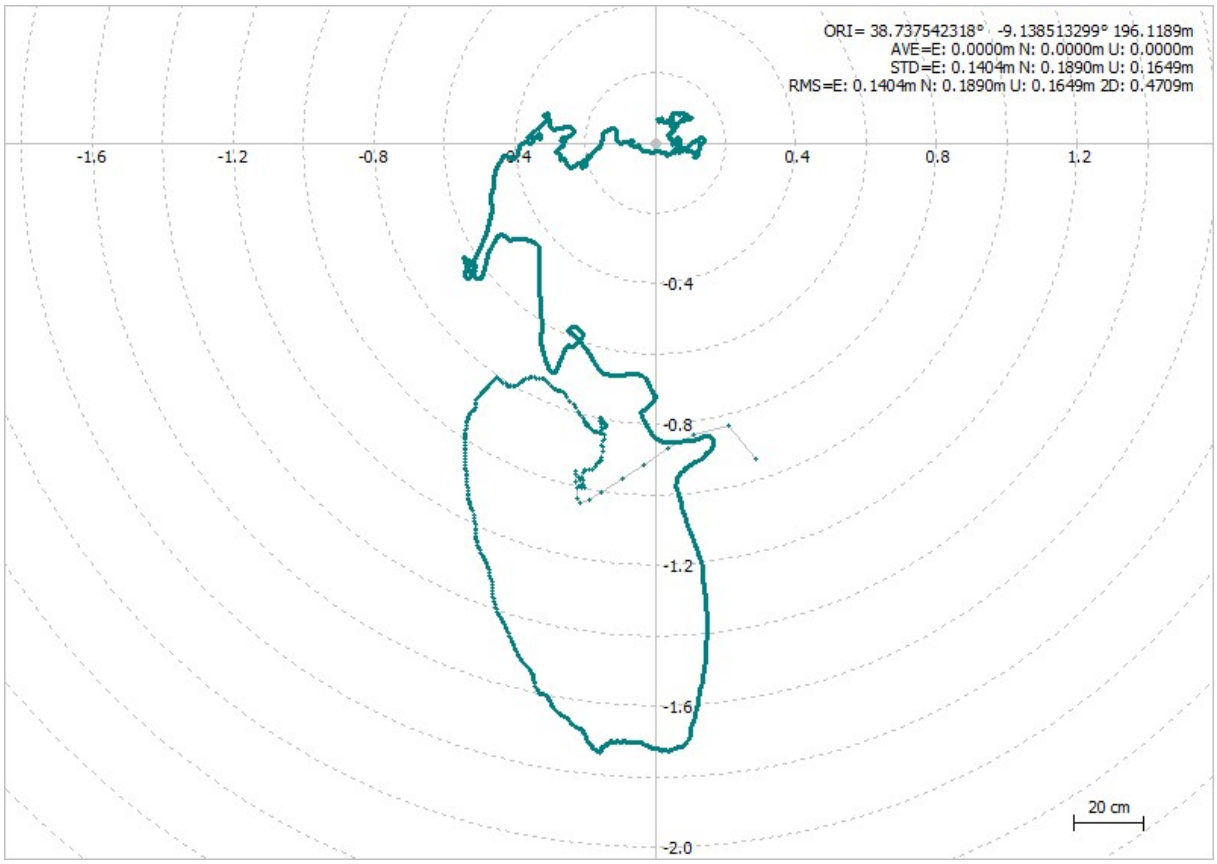

Figure 5.5: Scatterplot of PPP position results for RF6 (day 1)

5.3.3 ProFlex 500 receiver antenna position

For the ProFlex 500 receiver the same method has been applied, with the difference that the data collection ran from midnight 08/12/2020 until 23:59:59 of 9/12/2020, for a total of 172800 epochs, and that IGS rapid products were used instead of final products due to final products not having been computed at the time of writing. Also, since this is a dual-frequency receiver, the ionospheric error modeling was replaced by the ionosphere-free model, which requires a multi-frequency receiver. This receiver is connected to the antenna designated RF4. The estimated position will later be used to analyse the error convergence of the ProFlex 500 auto-survey. The resulting position estimate is given in Table 5.3, and the scatterplot of the position solutions for the first day is presented in Figure 5.6.

Day	X (m, ECEF)	Y (m, ECEF)	Z (m, ECEF)
1	4918524.4387	-791213.3689	3969763.1261
2	4918524.5261	-791213.4105	3969763.1942
Average	4918524.4824	-791213.3897	3969763.1602

Table 5.3: PPP position results for RF4

As expected, since the receiver is dual-frequency, the resulting position estimation presents much less jitter, due to the reduction of ionospheric error from the ionosphere-free model.

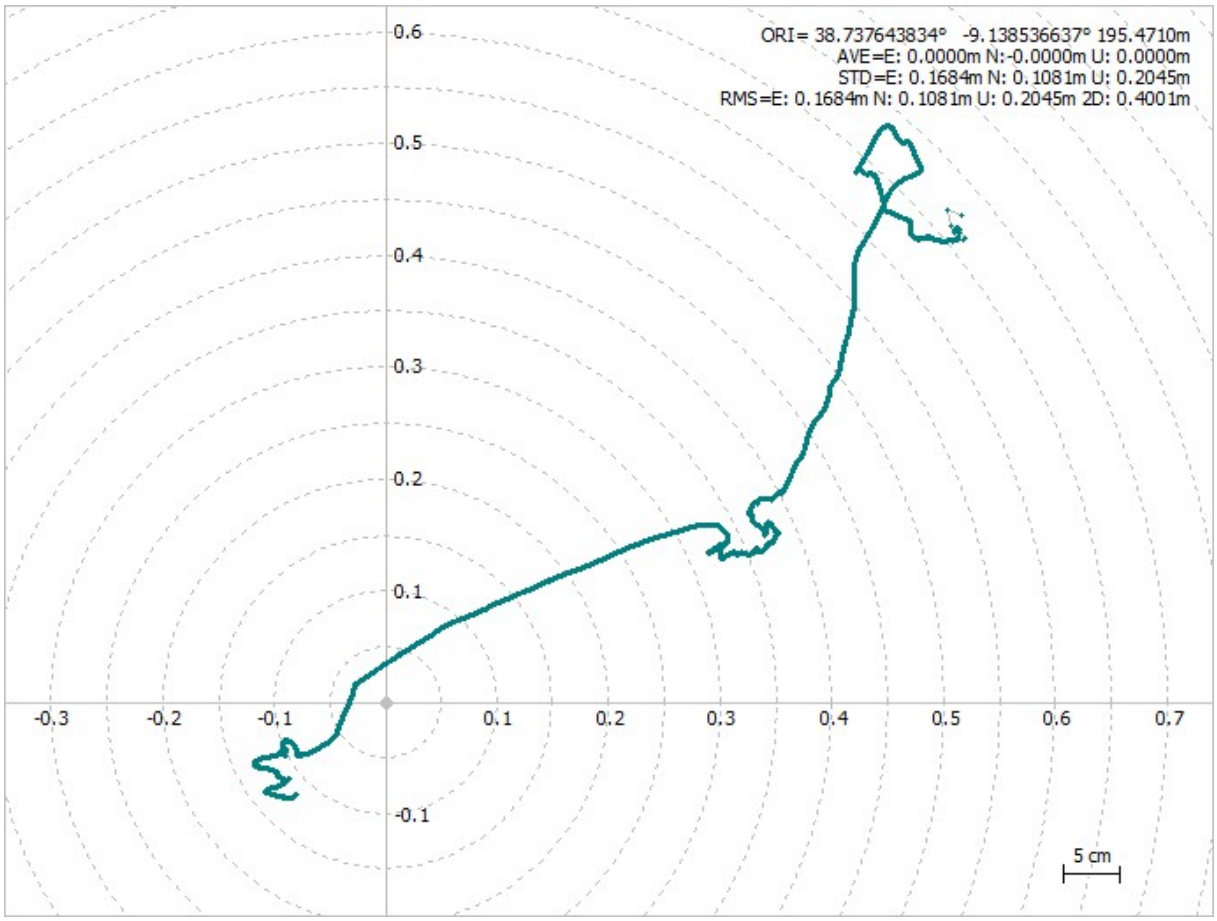

Figure 5.6: Scatterplot of PPP position results for RF4 (day 1)

5.4 Algorithm validation using IGS station data

5.4.1 Positioning algorithm validation

In order to validate the developed algorithms, it was necessary to use them with observations whose receiver antenna position is accurately determined. To this end, we ran the algorithms against 24h of observation data retrieved from the IGS. IGS provides users with free access to GNSS data from geodetic-grade receivers from all over the world, which can be downloaded from their FTP sites [45] using the routines from Annex A. For the validation process of this thesis, we chose their high-rate datasets, which are taken at 1s intervals like the measurements of the receivers used in this thesis. The downloaded data corresponds to a set of 24 1-hour observations using a reference receiver, as well as a set of navigation messages that contains 24h of navigation messages. This data was then processed to remove unused observations and constellations, leaving only the navigation message and L1 observations for the GPS satellites.

For this validation, it was used GNSS data from ESA's Malargüe Satellite Tracking Station in Mendoza, Argentina, which has the station code MGUE. The used data was captured on 25/10/2020 for 86400 epochs. The initial results, using the methods in Sections 3.1 through 3.4 and without applying the Hatch Filter, are presented in Figure 5.7 and Table 5.4.

Error Metric	LS	WLS	EKF	UKF
Mean (m)	1.330	1.064	3.482	1.213
RMS (m)	3.687	3.265	91.597	70.619
DRMS (m)	2.155	1.885	48.225	36.298
CEP (m)	1.597	1.397	1.403	0.512
R95 (m)	3.429	3.445	2.000	1.149
MRSE (m)	3.438	3.087	91.531	70.609
SEP (m)	2.301	2.037	1.765	0.676
SAS90 (m)	5.149	4.565	3.345	1.679

Table 5.4: Error metrics for the reference receiver

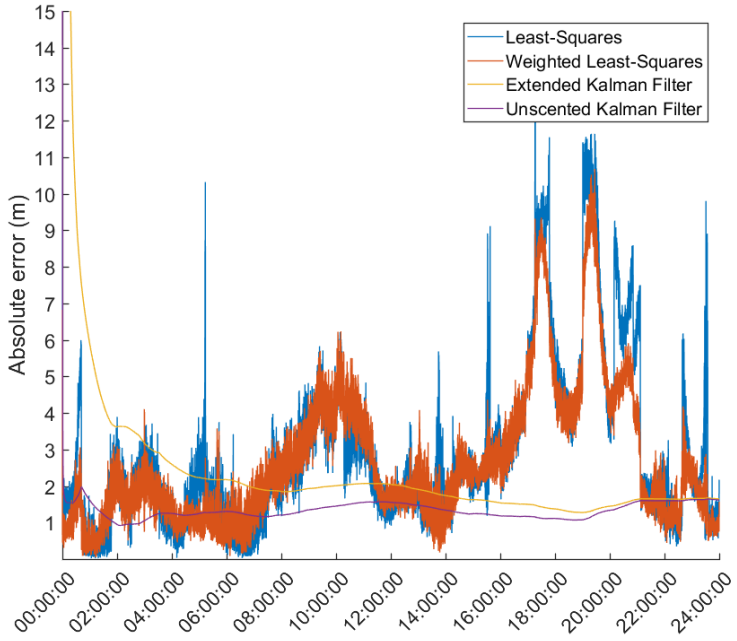

Figure 5.7: Absolute position error for the reference receiver

The position used to initialize the methods was a random point in the city of Buenos Aires. These results were obtained with a very high initial position variance for the EKF and UKF algorithms of $\sigma^2_{x,y,z} = 10^8$, corresponding to an expected 10km initial position error. However, as can be clearly seen, this initial estimate was too far from the true initial position error, which is in the order of 1000km. While we could provide a more accurate initial position error estimate right from the start, this would require the user to know roughly the distance to the initial position estimate, which is a non-user-friendly solution, or a higher initial position error, which might lead to a significantly increased time to convergence. To this end, a slightly different strategy was devised. If the initial position estimate is a point taken from a small list of possible points, for example the capitals of countries which is easily implemented in an end-user ready product, the receiver could do an initial Least Squares estimate of the receiver position, which would then be used to initialize the EKF and UKF algorithms. This allows a much smaller initial position

variance on the order of tens of meters to be used with negligible computational impact. After this correction, and setting the initial position variance to be $\sigma^2_{x,y,z} = 10^4$, corresponding to a 100 meter initial error, another simulation was run to validate the change. The results obtained are presented in Figures 5.8 and 5.9 and Table 5.5, and confirm the validity of the proposed initialization method since the error metrics for the Extended and Unscented Kalman Filters are improved from an average error higher than the Weighted Least Squares method (and, in the case of the Extended Kalman Filter, higher than the Least Squares method) with very high deviations to a much more tight position solution space.

Error Metric	LS	WLS	EKF	UKF
Mean (m)	1.330	1.064	0.986	0.986
RMS (m)	3.687	3.265	1.345	1.345
DRMS (m)	2.155	1.885	0.644	0.644
CEP (m)	1.597	1.397	0.537	0.540
R95 (m)	3.429	3.445	0.537	0.611
MRSE (m)	3.438	3.087	0.915	0.915
SEP (m)	2.301	2.037	0.756	0.756
SAS90 (m)	5.149	4.565	0.781	0.798

Table 5.5: Error metrics for the reference receiver after correction of initial position

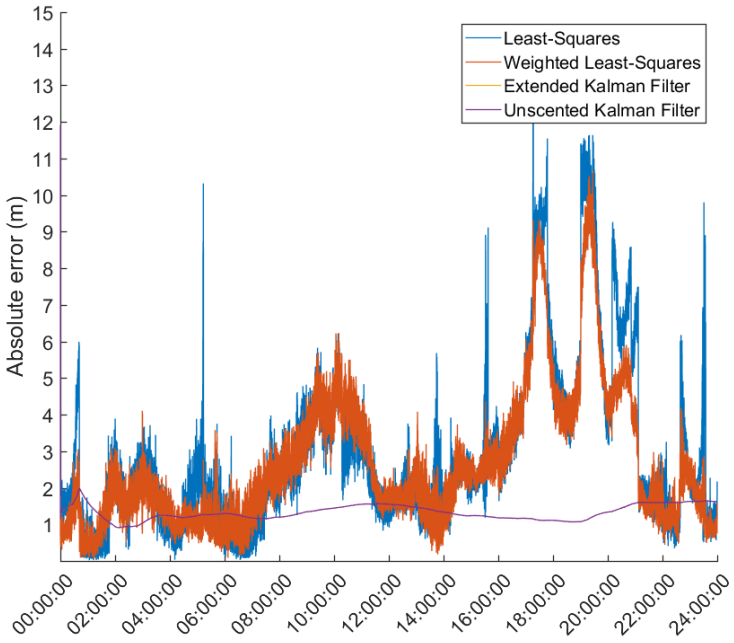

Figure 5.8: Absolute position error for the reference receiver after correction of initial position

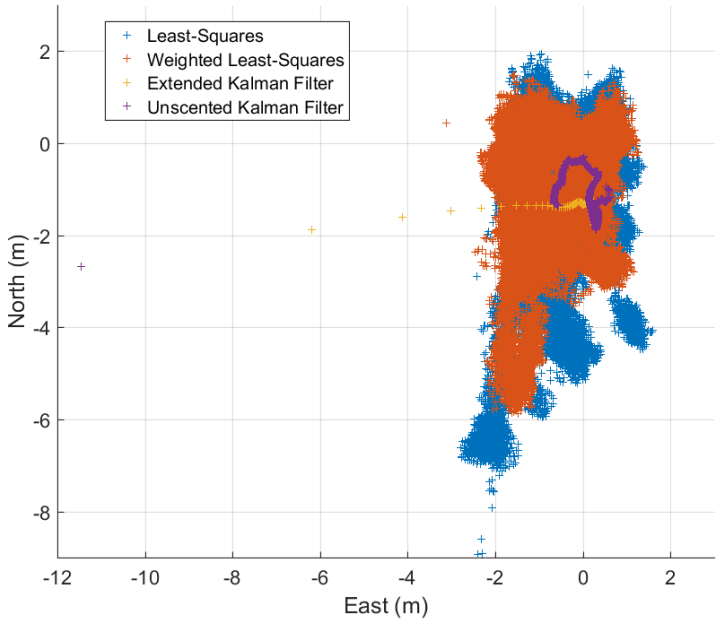

Figure 5.9: Scatter plot of position results for the reference receiver after correction of initial position

5.4.2 Hatch filter validation

Having validated the positioning methods, we can now test the performance of the Hatch filter for different filtering parameters in order to select one to apply to the rest of our experimental results. Since, as stated in Section 3.5, the Hatch Filter is dependent on the accurate detection of cycle slips to reinitialize the filter, the Loss-of-Lock flag present in the RINEX observations file, the LLI flag, was used to signal the Hatch Filter to reset the filter. However, the LLI flag is set by the GPS receiver, which might not detect the cycle slip accurately. This is clearly seen when using the reference dataset, which didn't update the LLI flag when a cycle slip occurred for SVN 7 at epoch 18738. The cycle slip at this epoch was strong enough to disable the developed algorithms from running, since it produced a position error in the order of 10^7 meters, for the Least Squares methods, that produced errors throughout the positioning algorithms. Since the LLI flag is clearly not enough to detect a cycle slip, another method must be used. A simple but effective implementation was devised, using the difference between the measured and smoothed pseudoranges for a given epoch. If a cycle slip occurs, this difference will be very large, to the point of several thousand meters; as such, we can use a difference threshold for the pseudoranges to detect the slip and reset the hatch filter accordingly. The result of this implementation is presented in Figures 5.10 and 5.11, where the change completely mitigated the effect of the cycle slip in the Least Squares and Weighted Least Squares algorithms. The threshold difference used was of 5 meters and the filtering constant was 0.005, with such threshold chosen since the difference between the measured and smoothed pseudoranges is very small compared to the effects of the cycle slips, which are anywhere from approximately a few meters to the order of millions of meters. While this method doesn't provide a concrete, clear identification of cycle slips, and as such won't detect those that create small position variations, it provides a computationally efficient, simple solution that can easily be used by single-

frequency receivers, and will be the method used throughout this thesis for cycle-slip correction.

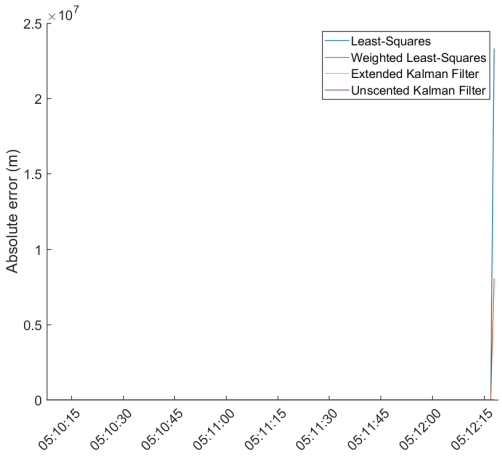

Figure 5.10: Detail of the effect of a cycle slip in the Hatch Filter

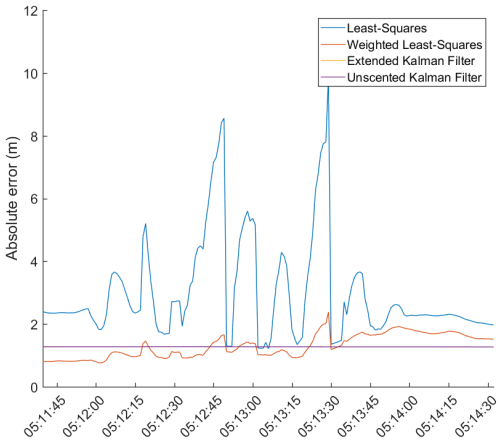

Figure 5.11: Detail of the result of cycle slip correction in the Hatch Filter

From these results, it is clear that the Hatch Filter provides a strong damping effect on the pseudorange observations, with this effect proportional to the filtering window γ^{-1}, which in turn result in a much less noisier estimation using both Least Squares and Weighted Least Squares; it should be noted, however, that the Extended and Unscented Kalman Filters were mostly unaffected by the cycle slip; this is due to their nature as state estimation filters, which attenuate changes to the measured states and mitigate sharp changes to their observations.

In order to analyse the effect of the filtering window in the position solution, the Hatch filter was implemented with filtering constants of 0.005, 0.01, 0.015 and 0.02, corresponding respectively to filtering windows (γ^{-1}) of 200, 100, 66.7 and 50 seconds. The results are presented in Table 5.6 and Figures 5.12 through 5.15.

From these results, we see that a shorter filtering window provides a better average error for the Least Squares and Weighted Least Squares, although it increases the spread of the position solutions compared to longer filtering windows, as can be seen by the increased error in some metrics. However, for all the metrics, this difference is very small, in the order of decimeters or less. For the Extended and Unscented Kalman Filters, the added filtering step provides a very small improvement to the results of all the metrics, but on the order of milimeters only. Contrarely to the Least Squares methods, the Kalman Filters get better results with a larger filtering window, which can be attributed to much less noisier observation inputs to the filters, leading to lower noise overall in the entire filter.

To allow for benchmarking the results of other algorithms with and without the added Hatch Filter, it was chosen to run the rest of the simulations with $\gamma = 0.010$. This value strikes a good balance between the shorter filtering windows, that are biased towards the Least Squares methods, and the longer filtering windows, that are favorable to the Kalman Filters.

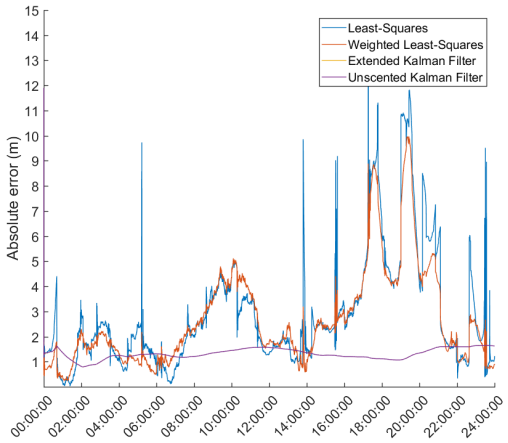

Figure 5.12: Absolute error for the reference receiver with Hatch Filter with $\gamma = 0.005$

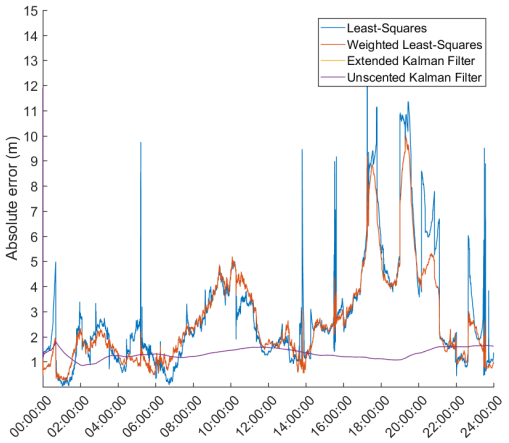

Figure 5.13: Absolute error for the reference receiver with Hatch Filter with $\gamma = 0.010$

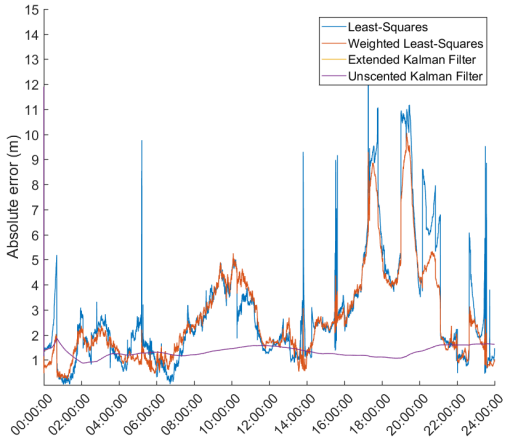

Figure 5.14: Absolute error for the reference receiver with Hatch Filter with $\gamma = 0.015$

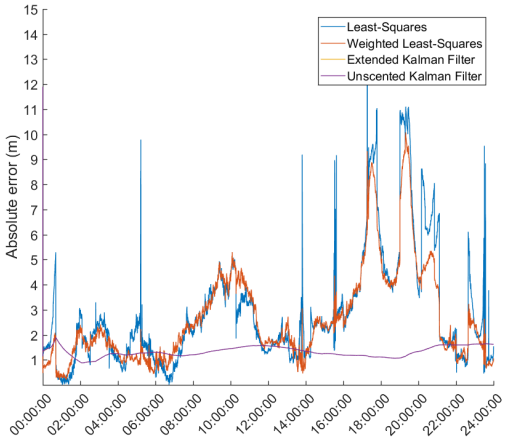

Figure 5.15: Absolute error for the reference receiver with Hatch Filter with $\gamma = 0.020$

	Least Squares				Weighted Least Squares				Extended Kalman Filter				Unscented Kalman Filter			
γ	**0.005**	**0.010**	**0.015**	**0.020**	**0.005**	**0.010**	**0.015**	**0.020**	**0.005**	**0.010**	**0.015**	**0.020**	**0.005**	**0.010**	**0.015**	**0.020**
Avg (m)	1.342	1.333	1.331	1.331	1.109	1.084	1.077	1.073	0.983	0.984	0.984	0.985	0.983	0.984	0.984	0.985
RMS (m)	3.685	3.669	3.665	3.663	3.295	3.264	3.255	3.251	1.335	1.340	1.342	1.342	1.334	1.340	1.341	1.342
DRMS (m)	2.112	2.119	2.124	2.126	1.858	1.859	1.861	1.862	0.634	0.638	0.640	0.641	0.634	0.637	0.640	0.641
CEP (m)	1.516	1.523	1.526	1.530	1.363	1.358	1.361	1.364	0.510	0.522	0.528	0.529	0.537	0.538	0.539	0.539
R95 (m)	3.059	3.048	3.039	3.028	2.875	2.904	2.919	2.939	0.510	0.522	0.528	0.529	0.630	0.619	0.615	0.612
MRSE (m)	3.432	3.419	3.414	3.413	3.103	3.078	3.071	3.068	0.902	0.910	0.912	0.912	0.902	0.909	0.912	0.912
SEP (m)	2.171	2.205	2.220	2.225	2.006	1.984	1.978	1.978	0.741	0.750	0.753	0.753	0.741	0.750	0.753	0.752
SAS90 (m)	5.063	5.078	5.101	5.111	4.528	4.486	4.493	4.488	0.756	0.770	0.775	0.775	0.820	0.808	0.803	0.800

Table 5.6: Error metrics for different values of γ of the Hatch Filter for the reference position

5.5 Reference Station antenna position determination

Having validated the proposed algorithms against a known receiver, we will now proceed with the position determination of the Reference Station antenna, designated RF2 and whose reference position was determined in Chapter 5.3.1.

Using the positioning methods developed for this thesis, as well as the Hatch Filter, a position survey of the antenna, starting at midnight of 25/10/2020 and with duration of 24 hours, was done. The obtained results of the complete survey are presented in Table 5.7 and Figures 5.16 and 5.17.

	No Hatch Filter				**Hatch Filter with $\gamma = 0.01$**			
Error Metric	**LS**	**WLS**	**EKF**	**UKF**	**LS**	**WLS**	**EKF**	**UKF**
Mean (m)	1.386	1.300	0.750	0.602	1.388	1.312	0.732	0.587
RMS (m)	2.655	2.597	1.729	1.477	2.426	2.415	1.728	1.477
DRMS (m)	1.589	1.557	0.818	0.750	1.341	1.377	0.826	0.755
CEP (m)	1.331	1.346	0.612	0.575	1.134	1.242	0.615	0.581
R95 (m)	2.708	2.598	1.855	1.332	2.270	2.223	1.889	1.532
MRSE (m)	2.264	2.249	1.558	1.349	1.990	2.028	1.565	1.355
SEP (m)	1.857	1.944	0.713	0.694	1.629	1.823	0.710	0.689
SAS90 (m)	3.413	3.336	2.620	2.232	3.025	2.907	2.609	2.222

Table 5.7: Error metrics for 24 hour position survey of the Reference Station Antenna

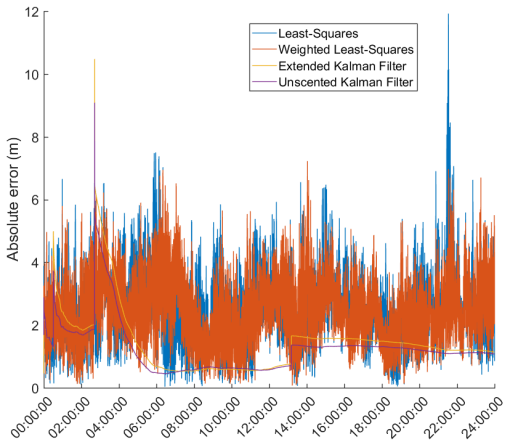

Figure 5.16: Absolute error for the RF2 antenna position with no Hatch Filter

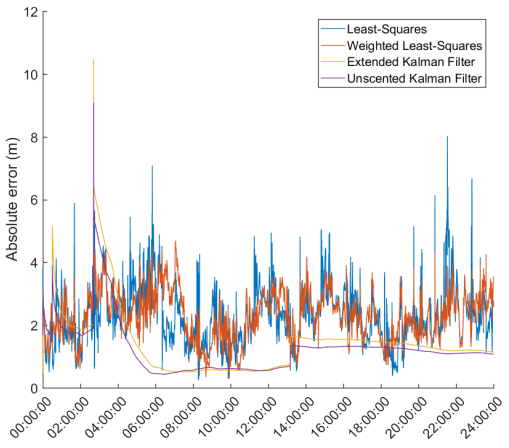

Figure 5.17: Absolute error for the RF2 antenna position with Hatch Filter and $\gamma = 0.010$

From this survey, we can see that both Kalman Filter methods present a much more precise and accurate position solution, presenting not only a lower mean error but also much tighter position solutions, as can be seen from the rest of the error metrics, although the Least Squares methods also present a relatively good estimate of the antenna position. The surveyed position presents an error at or bellow meter-level, which is a very good result considering that the 1σ error of the pseudorange measurements

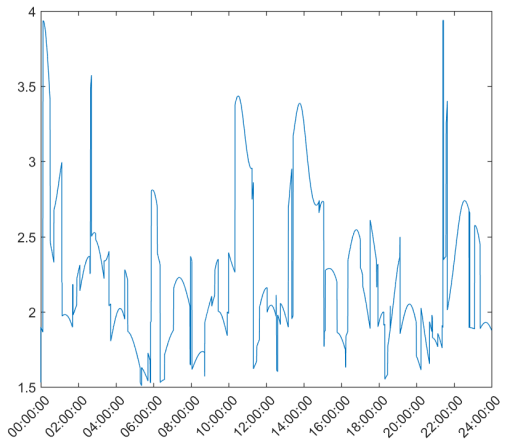

Figure 5.18: GDOP values for the 24 hour survey of the reference station antenna

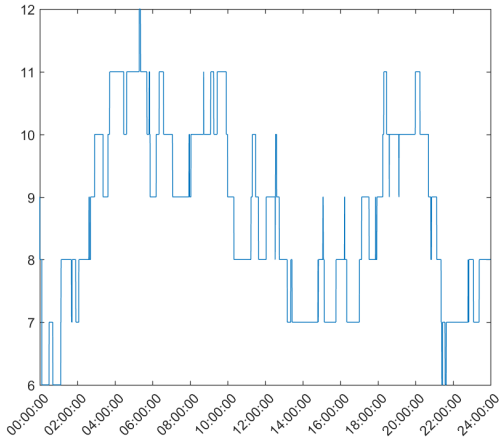

Figure 5.19: Number of satellites used for position determination for the 24 hour survey of the reference station antenna

is approximately 7 meters. The Hatch Filter employed also allows for a significant reduction in the spread of the Least Squares and Weighted Least Squares position solutions, reducing their overall error metrics; however, the mean error for these methods presents a very slight increase. This can be attributed to the reduction of the measurement noise, which can sometimes present some measure of error cancelation due to random errors. However, since this effect is random and not predictable, it should not be considered a kind of noise-cancelling effect. For the Kalman Filters, the Hatch Filter produces a slight decrease in the mean error of the position estimate, but a small increase in some of the other error metrics. However, since this increase is on the same order of the reduction in the mean error it is an acceptable trade-off.

5.6 Convergence over time of the position solution

Since this thesis objective is the characterization of auto-surveying methods for use in base stations for differential GPS methods, an important metric is the time necessary for the position solution to converge to below a given error threshold. This is an important measurement since not all base stations are permanent: sometimes a user wants to setup a base station for, for example, usage with a DGPS-enabled drone and as such might not have the time for a complete geodetic survey of the base station antenna position. For this end, a comparison of the mean position error over time was done, with results presented in Figures 5.20 and 5.21.

From these results, we can see that the presence of the Hatch Filter doesn't change the overall mean error dynamic, which is to be expected since the Hatch Filter's function is one of noise reduction and not hard data filtering. We also see that, even though both the Extended and Unscented Kalman Filters present a higher initial error, their mean error falls bellow the mean error of the Least Squares methods relatively quickly, in just a few hours. Although the present results show a sharp decrease in the mean error, that might be due to a change in constellation geometry; however, there is a clear

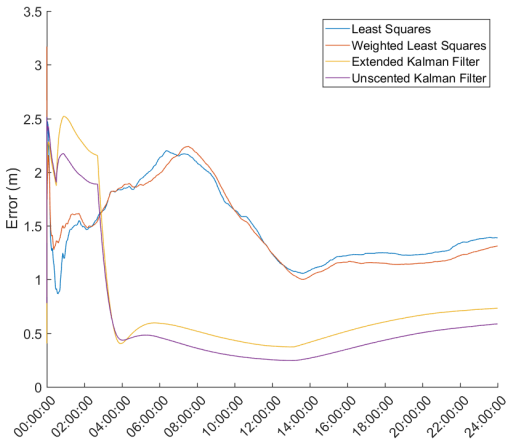

Figure 5.20: Mean error variation over time for the reference station antenna with no Hatch Filter

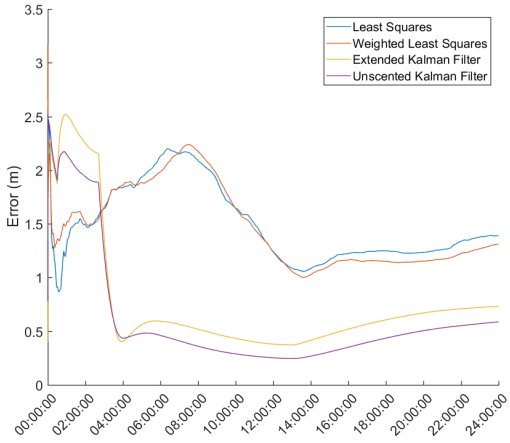

Figure 5.21: Mean error variation over time for the reference station antenna with Hatch Filter and $\gamma = 0.010$

trend in the data, which is the much less pronounced variation over time of the Kalman Filter methods, which, although presenting some degree of variation, is much more bounded in its results compared to the Least Squares methods. Additionally, for both Least Squares methods we see that their mean error never goes down below 1 meter except for a very short time at the start of the observation, with the Weighted Least Squares method closely following the Least Squares method and showing only a marginal improvement with no clearly defined trend, which precludes the conclusion that the Weighted Least Squares is significantly better than the Least Squares method. For the Kalman Filters, we clearly see the improved estimation of the Unscented Kalman Filter, providing a better position estimate than any other method. Another remark is the increasing mean error tendency after approximately 13 hours of surveying. This increase is most likely due to constellation changes, as can be seen from Figure 5.19, where a variation of the number of visible satellites is visible, followed by a significant increase in the DOP parameter, as per 5.18. To note, however, is that the Least Squares methods present a smaller initial error than the Kalman Filters; however, this result cannot be taken at face value, since the number of obtained data samples are small and the Least Squares methods are noisy and not bounded by previous results and the results present a relatively high DOP; as such we cannot be certain if the estimated position using the Least Squares methods at that time is indeed a good estimate

5.7 Improving the position estimate with statistical methods

While until now we have only been using the average of the position solutions to compute the estimate of the position solution, this method might not be the best. By its definition, an average might be biased by a few position solutions that present a large error, something that we wish to avoid. To that end, we will test three other possible approaches for the estimation of the antenna position solution: the median, the weighted average and the maximum likelihood estimator (MLE).

5.7.1 The median as position estimate

One statistical measure that is designed to avoid bias from fringe results in a data set is the median. This value is given by the point that separates the higher half and lower halfs of a data set, and as such provides a more ”true” estimate of the ”average” value than the mean.

In this thesis, we calculated the median of the position solution during the entire observation, and computed the associated error. The results are presented in Figures 5.22 and 5.23

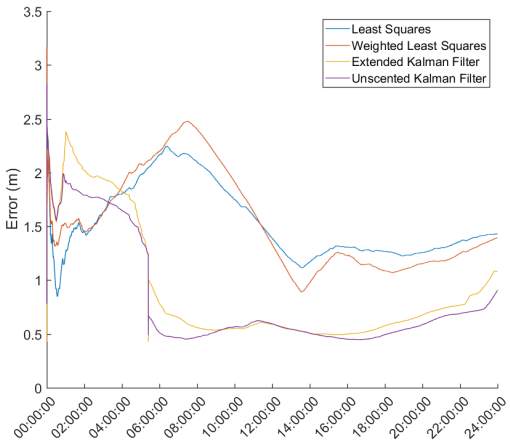

Figure 5.22: Median error variation over time for the reference station antenna with no Hatch Filter

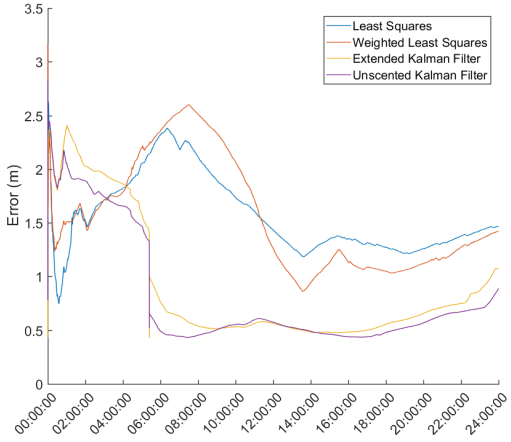

Figure 5.23: Median error variation over time for the reference station antenna with Hatch Filter and $\gamma = 0.010$

From here we can see that the median approach produces a slightly worse error than the mean, which is accentuated by the increased error in the presence of the Hatch Filter. This, coupled with the fact that the changes in the position error are minimal, leads us to exclude this method as a viable alternative to the mean.

5.7.2 The weighted average as position estimate

Another possible method to determine the position estimate is the weighted average. This method attributes a weight to each observation, and then estimates the receiver position in a way that gives more prevalence to position solutions with higher weights, and reduces the effect of the position solutions with lower weights. The choice of the weight metric is critical to the accuracy of this method, and several weights are possible. In this thesis, the weighting was done using the inverse of the GDOP parameter, which makes it so that the position solutions with lower expected accuracy are given lower weight. The results of this analysis are presented in Figures 5.24 and 5.25.

From these plots, we obtain a similar result to that of Chapter 5.7.1: There is a slight worsening of the position error, making this method not suitable, in its current form, for position estimation when compared with the mean. However, it should be noted that the GDOP parameter is not the only weighting parameter that can be used, and other weighting methods might produce different results.

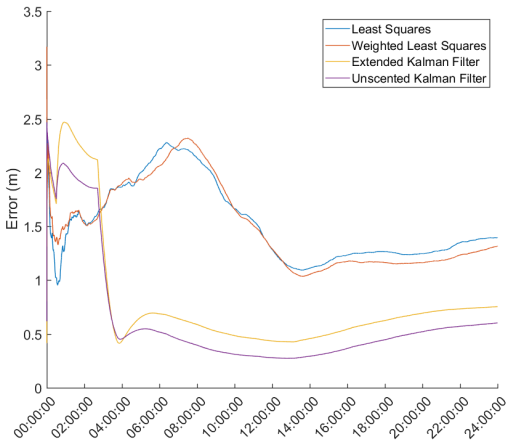

Figure 5.24: Weighted average error variation over time for the reference station antenna with no Hatch Filter

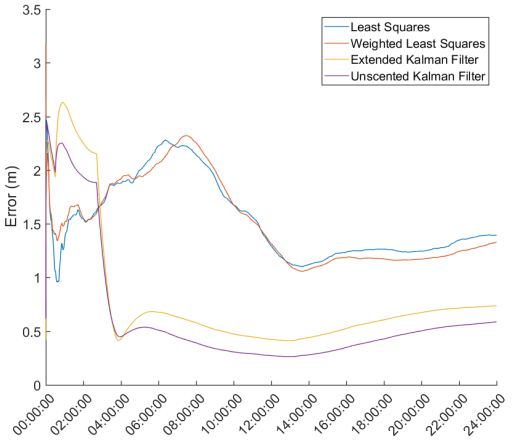

Figure 5.25: Weighted average error variation over time for the reference station antenna with Hatch Filter and $\gamma = 0.010$

5.7.3 The MLE as position estimate

The final method used to determine the position estimate from the position solutions is the maximum likelihood estimator. This method is based in the Maximum Likelihood Estimation method from Chapter 2.8. Using this method, the maximum likelihood estimator was continuously calculated during the entire observation. While initially both Normal and t-Location Scale distributions were considered for analysis, the method used to compute the MLE was unable to converge for the t-Location Scale distribution; as such, it was only possible to obtain results for the Normal distribution. The results are presented in Figures 5.26 and 5.27.

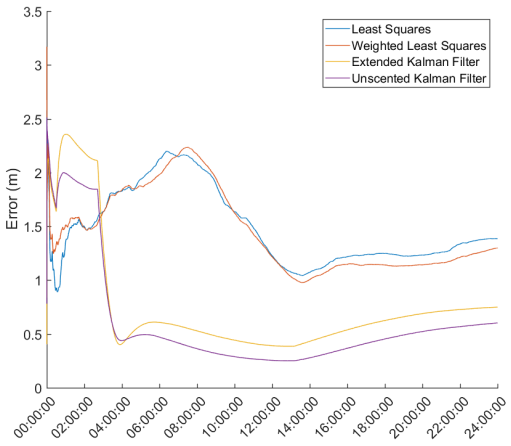

Figure 5.26: Maximum Likelihood Estimator error variation over time for the reference station antenna with no Hatch Filter

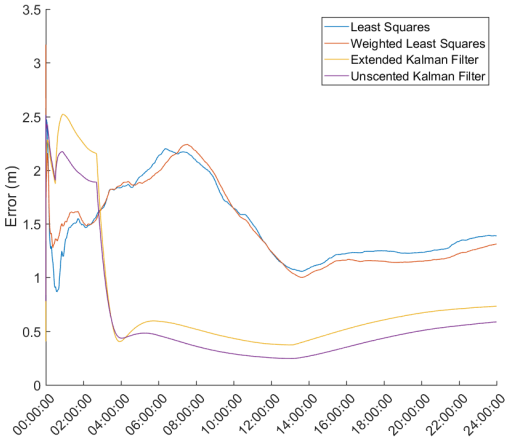

Figure 5.27: Maximum Likelihood Estimator error variation over time for the reference station antenna with Hatch Filter and $\gamma = 0.010$

The Maximum Likelihood Estimate of the antenna position is exactly the same as the mean antenna position obtained in Chapter 5.6, which is to be expected since the maximum likelihood estimator of the

normal distribution is the mean. As such, no improvement whatsoever is obtained with MLE using a normal distribution.

5.8 Filtering using a threshold

Until now we only discussed methods to obtain a better estimate from all the available data, irrespective of its impact in the position estimate. Another possible data conditioning method is filtering according to a specific threshold. Given a set of position solutions, we can define a threshold for the data and ignore any position solution that is outside that threshold.

In this implementation, the threshold is given by the standard deviation, σ centered on the current mean of the data set. To analyse this filtering method two different thresholds were used: 1σ and 2σ. The resulting errors are presented in Figures 5.28 through 5.31

It is clear from these results that the 2σ threshold provides a lower error for the Kalman Filters, but it also allows a greater degree of variation which is seen after roughly 13 hours after the start of the start of the observation where the error starts to increase. For the Least Squares methods, the higher allowed variation of this threshold gives an overall increase in the error of the estimate. One important thing to note is that the increased variation also allows for noisier measurements to make their way into the position estimate. While this has been benefic to the Kalman Filters and the Weighted Least Squares, it should not be taken as granted that the 2σ threshold is always better. For the 1σ threshold, the results are much more bounded, and present signifficantly lesser variations.

Overall, the 2σ threshold provided better results for the position estimate. However, as stated, this threshold is larger and as such allows noisier estimates to affect the position estimate when compared to the 1σ threshold, which might have both a beneficial effect, as seen by the Kalman Filters, and a more harmful effect, as seen in the Least Squares methods, which are dependent on the specific spread of measurements that are present in the observation.

Even so, given these results, a preliminary analysis shows that the 2σ threshold produces better results. This decision is supported by the overall tendency for the GNSS position estimates to converge to a mean value closer to the true position over time, which tends to lower the overall error as the number of observations increases.

5.9 Final proposed positioning method

Given the plethora of methods that have been investigated in the previous chapters, it naturally follows the question: ”What is the result when these methods are all combined?”. To answer this question we combined the methods studied in Chapters 5.5, 5.7 and 5.8, choosing only the methods that provide better results than the methods of Chapter 5.5.

To this end, the following methods were selected:

- Least Squares methods

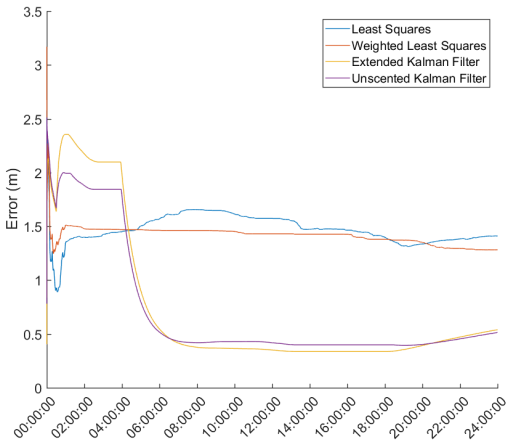

Figure 5.28: Effect of a 1σ threshold on the mean error over time for the reference station antenna with no Hatch Filter

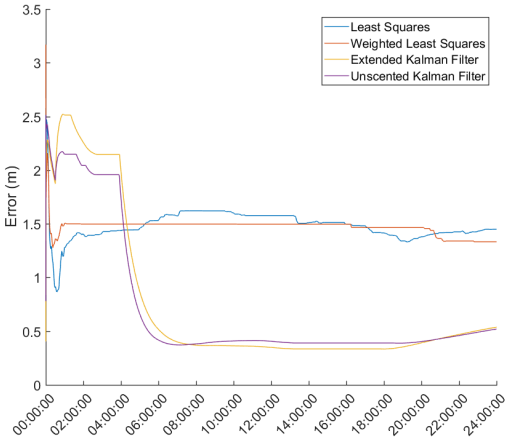

Figure 5.29: Effect of a 1σ threshold on the mean error over time for the reference station antenna with Hatch Filter and $\gamma = 0.010$

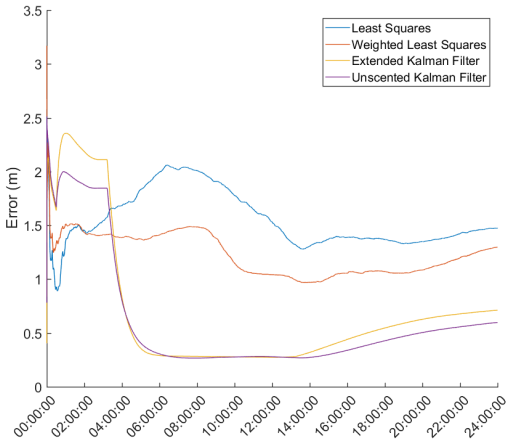

Figure 5.30: Effect of a 2σ threshold on the mean error over time for the reference station antenna with no Hatch Filter

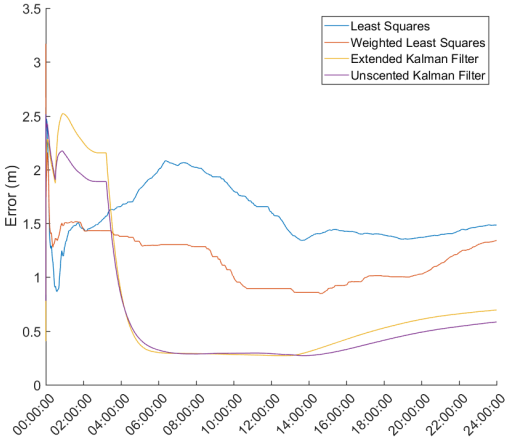

Figure 5.31: Effect of a 2σ threshold on the mean error over time for the reference station antenna with Hatch Filter and $\gamma = 0.010$

  - Hatch filter with $\gamma = 0.010$
  - Position estimate using the mean value of the measurements
  - No thresholding

- Kalman Filter methods
  - Hatch filter with $\gamma = 0.010$
  - Position estimate using the mean value of the measurements
  - 2σ threshold filter for position measurements

This allows all the methods to be compared against each other in their ”best” possible results. Of note is the fact that the Least Squares methods still present the Hatch filter even when it degrades their

mean position estimate. This is due to the fact that the Hatch filter removes a signifficant amount of noise in the data, allowing for much more precise, even if slightly less accurate, position estimates. The error measurements in these conditions are presented in Table 5.8 and Figure 5.32.

Error Metric	LS	WLS	EKF	UKF
Mean (m)	1.386	1.300	0.694	0.584
RMS (m)	2.655	2.597	1.536	1.314
DRMS (m)	1.589	1.557	0.740	0.676
CEP (m)	1.331	1.346	0.599	0.566
R95 (m)	2.708	2.598	1.357	1.169
MRSE (m)	2.264	2.249	1.370	1.177
SEP (m)	1.857	1.944	0.710	0.656
SAS90 (m)	3.413	3.336	2.471	2.103

Table 5.8: Error metrics for 24 hour position survey of the reference station antenna using the finalized position methods

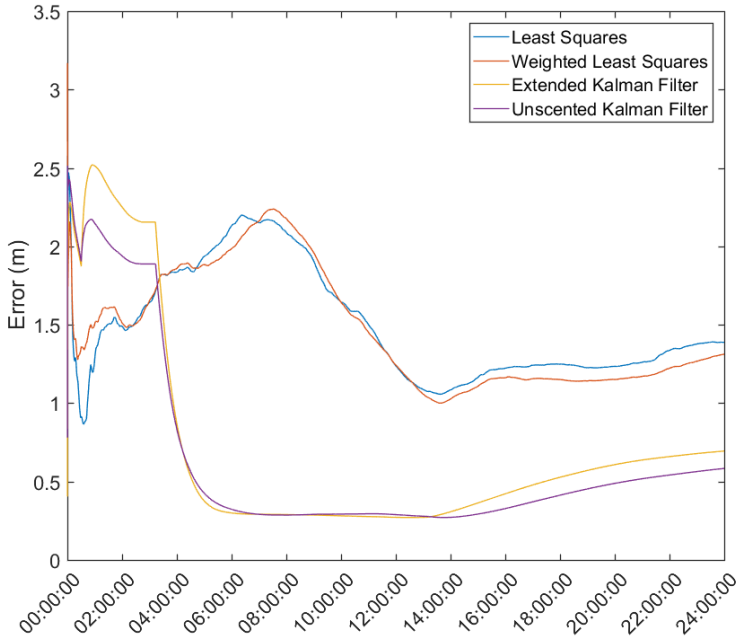

Figure 5.32: Mean error for 24 hour position survey of the reference station antenna using the finalized position methods

From here we can confirm a trend that has been constant throughout all the observation analysis in this chapter: the Kalman Filter methods present a much better position estimate overall than the Least Squares methods, with the Unscented Kalman filter being slightly better than the Extended Kalman Filter. This result was expected, since the Kalman Filter approaches have been used as the *de facto* positioning methods when it comes to GNSS.

5.10 Impact of RAIM in auto-surveying

As stated in Chapter 3.7, RAIM doesn't provide position solutions; instead, it provides integrity augmentation for a receiver. While originally designed for computing horizontal and vertical protection levels in a aircraft-borne receiver, its utility is not restricted to such use. The capability for this system to detect and remove observations that degrade the position solution is also highly desirable for a base station GNSS receiver, since it reduces the overall measurement noise and increases the precision of the auto-survey.

In order to test how this algorithm impacts the position estimate, and in the absence of real RAIM events, several different failures were added to the survey from Chapter 5.5. These consist in

- A 15 meter pseudorange bias between epoch 100 and 200
- A 30 meter pseudorange bias between epoch 3000 and 3500
- A ramp bias, growing at the rate of 1 meter per second, between epochs 10000 and 12000

These bias where applied to random satellites in the sub-constellation that was used at that epoch, and the RAIM algorithm was run with a probability of false alarm of 8×10^{-7} [46]. The position error results with and without RAIM are presented in Figures 5.33 and 5.34, with a plot of the test statistic of the RAIM presented in Figure 5.35, where the epochs that had RAIM events were focused. The error metrics for the entire observation are also presented in Table 5.9. These results were obtained without Hatch filtering, since the Hatch filter would not produce any noticeable effect on the results.

Error Metric	LS	WLS	EKF	UKF
Mean (m)	1.391	1.300	0.801	0.649
RMS (m)	2.664	2.621	1.766	1.508
DRMS (m)	1.592	1.575	0.806	0.739
CEP (m)	1.327	1.345	0.600	0.565
R95 (m)	2.715	2.602	1.806	1.403
MRSE (m)	2.272	2.276	1.574	1.361
SEP (m)	1.855	1.939	0.703	0.682
SAS90 (m)	3.414	3.339	2.666	2.276

Table 5.9: Error metrics for 24 hour position survey of the Reference Station Antenna after RAIM test

From these results, we can observe that the RAIM algorithm correctly detected the fault of the first two events, excluding the faulty satellite from the position solution right from the start of the event. For the third event, the RAIM algorithm only detected the fault after it grew to 16 meters of offset, but removed the satellite correctly afterwards. This "dead zone" in the RAIM test statistic's threshold is due to the false alarm probability selected. However, while the later two events had no discernible effect in the measurement error, the first event produced an error of more than 10 meters even with the removal of the satellite using the RAIM algorithm. This might be an implementation error, and should be subjected to further analysis. Overall, even in the presence of the incorrectly handled fault event, the error was

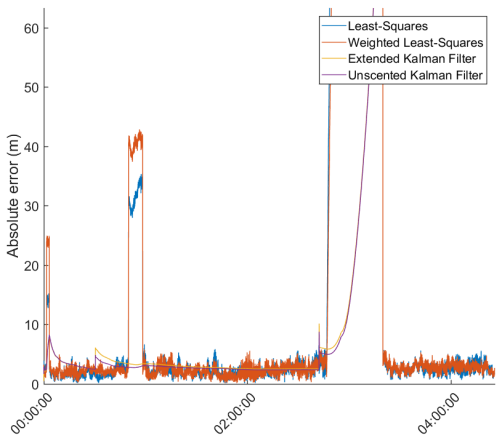

Figure 5.33: Reference station receiver error in the presence of simulated faulty satellites without RAIM

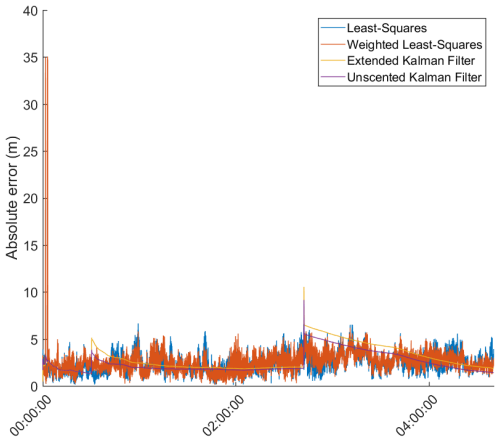

Figure 5.34: Reference station receiver error in the presence of simulated faulty satellites with RAIM FDE algorithm

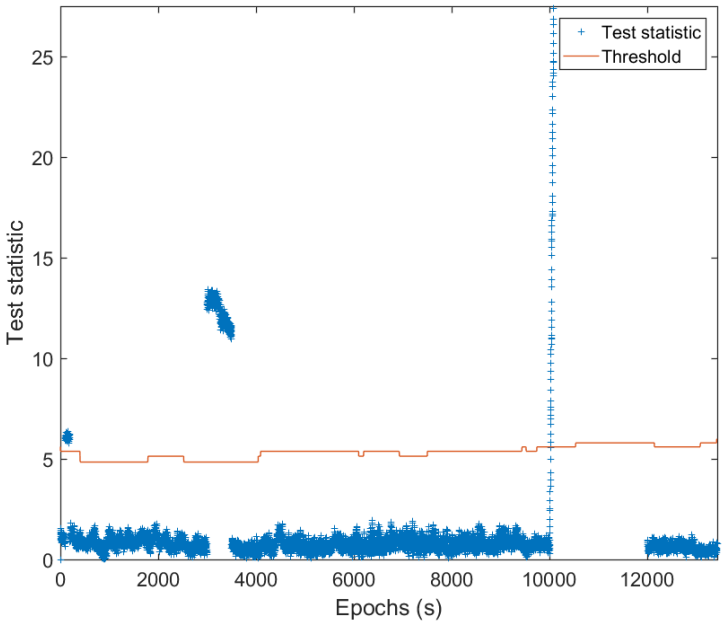

Figure 5.35: RAIM test statistic for the simulated faulty satellites

only very slightly impacted, and it is almost surely related to the missed failure event. All in all, we verify that the RAIM algorithms are still of use for a static receiver, since the error rejection they provide is also applicable to static receivers and can provide significant improvements to position determination.

5.11 Performance comparison with existing auto-survey methods

In order to benchmark our methods, we must compare them with a known auto-survey method. For this, we used the Survey-In mode of the u-blox 6T receivers as well as the RTKLIB in static mode for the ProFlex 500 receiver.

For both the u-blox and ProFlex receivers this auto-survey was done at 03/12/2020 for 24 hours, in clear meteorological conditions. For the u-blox receiver, the survey was done with the same antenna as the survey of Chapter 5.5, while the ProFlex auto-survey was done with the ProFlex AT1675-7M antenna. While the surveys where using different antennas, these receivers have different antenna requirements that preclude the usage of the same antenna for both receivers. However, since the test objective is to compare the surveyed position with the reference position, i.e. the survey error, this difference is not relevant enough. Finally, the u-blox receiver's auto-survey was done using the Survey-In functionality of the receiver, while the ProFlex's auto-survey was done by using RTKLIB in static EKF mode, due to this receiver's lack of a dedicated auto-survey routine.

The results of these surveys are presented in Figure 5.36. Comparing these results with the results presented in Figures 5.20 and 5.21, we see that the results of the Extended and Unscented Kalman Filters from the method proposed in Chapter 5.9 provide signifficantly better results when compared with the u-blox 6T receiver's Survey-In algorithm. However, when compared with the geodetic-grade, dual-frequency ProFlex 500 we obtain a worse position estimate, which is expected since it is a much better receiver than the u-blox 6T used. However, it should be noted that both the ProFlex 500 and the Kalman Filters of the proposed method do not show much difference in their accuracy, both being to within approximately 25 centimeters from each other and both converging to sub-meter error values within few hours, with a clear lead for the ProFlex 500.

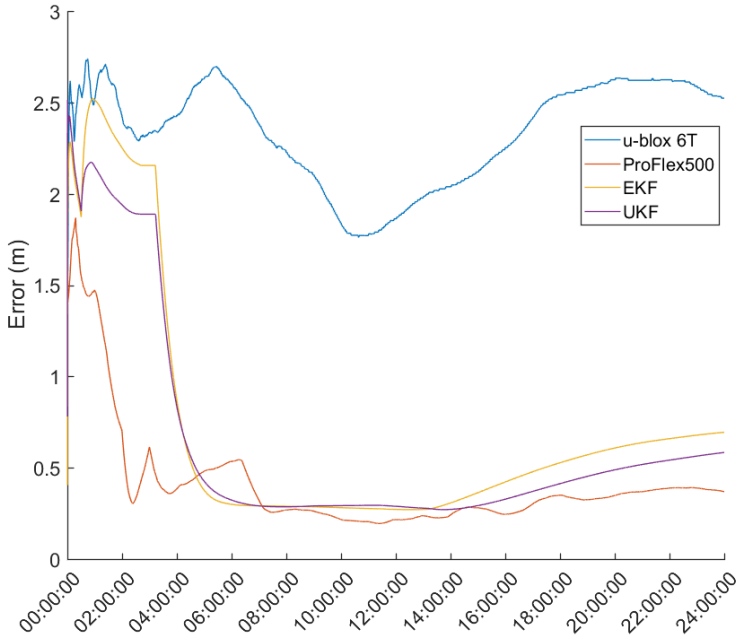

Figure 5.36: Auto-survey results for the u-blox 6T and ProFlex receivers for a 24 hour survey

5.12 Differential GPS test

As a final performance test, the previous methods were applied to a DGPS setup in order to determine the position of a rover receiver, with known position. To this end, two u-blox receivers were used, one connected to the antenna RF2 and another to the antenna RF6. This position solution was obtained using the observations of the two receivers and using the Double Difference method of Chapter 3.6. The base station reference positions are taken at 4 hour intervals by taking the average of the Extended and Unscented Kalman Filters from Chapter 5.9, and a 4 hour position determination of the rover receiver was performed for each reference position. The reference position is based only in the Kalman Filters due to their lower error compared to the Least Squares methods. The resulting error plots are presented in Figures 5.37 and 5.37 and the mean error is presented in Table 5.10.

	Extended Kalman Filter						Unscented Kalman Filter					
Hours	4	8	12	16	20	24	4	8	12	16	20	24
Mean error (m)	0.732	0.794	0.661	0.787	0.903	0.932	0.767	0.677	0.506	0.584	0.686	0.719

Table 5.10: Mean error for the DGPS receiver with base station position averaged after a set number of hours

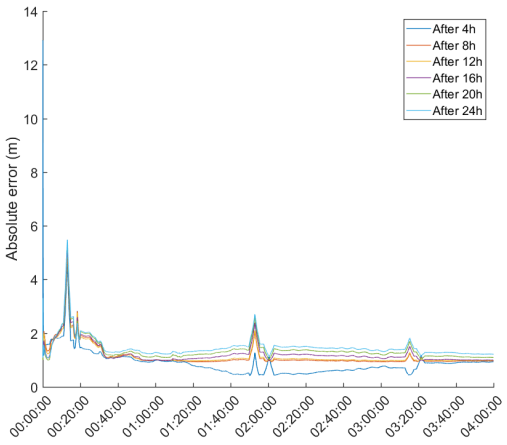

Figure 5.37: Rover position error with base station position obtained with EKF and averaged after a set number of hours

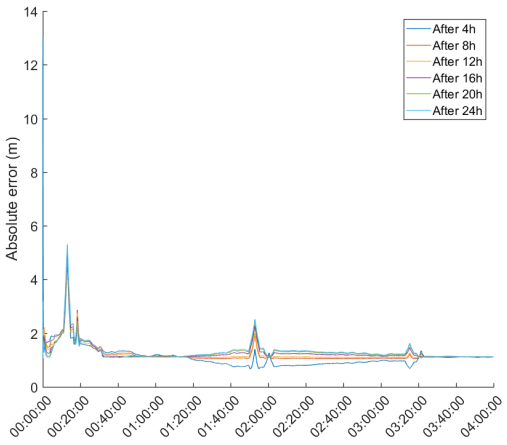

Figure 5.38: Rover position error with base station position obtained with UKF and averaged after a set number of hours

These results show clearly that both the Extended and Unscented Kalman Filters provide good estimates of the base station position, which are reflected in the sub-meter error of the rover position estimate. It can also be seen that the UKF shows a better position estimate, and that both methods still present the error increase after roughly 13 hours of survey.

Chapter 6

Conclusions

This thesis was developed with the goal of doing a comparative analysis of positioning algorithms when applied to the position estimation of a fixed base station receiver, in the context of a short-term, non-geodetic survey. To this end, a model of the GNSS observables and their errors was presented in Chapter 2. In Chapter 3 the several positioning methods used throughout this thesis were described, and in Chapter 4 a brief introduction was given on PPP, which was used for determining the reference position for the antennas used. Afterwards, on Chapter 5 the results obtained by the different positioning algorithms, as well as several methods to analyze and filter the results, were shown, demonstrating the performance of the used algorithms. This culminated in defining a ”best” positioning method, which was then used in a DGPS setup to validate the result.

This work has shown that the Extended and Unscented Kalman Filters provide a much better position estimation than the Least Squares methods, not only in mean error but also in every other error metric that was analyzed. It was also shown that the Hatch filter, while providing some improvements to the Least Squares methods, provides a very small improvement for the Kalman Filters. Finally, the usage of a 2σ threshold for the position solutions provides further improvement in the position estimates of the Kalman Filters, while slightly improving the Weighted Least Squares method and degrading the position estimate of the Least Squares algorithm. From these results, it was decided to ignore the Least Squares methods for the DGPS setup test in favor of the Kalman Filters.

Finally, a DGPS setup was used to test the impact of the base station position estimate in the rover position estimate.

6.1 Future Work

While the results presented in this thesis are very promising, they have been obtained using only pseudorange measurements, with an eventual phase smoothing. The logical next step in improving these results consists in replacing the pseudorange measurements with the much more precise carrier phase measurements.

Another part of this thesis that can be further worked on is the cycle slip detection routine. While it

currently performs satisfactorily, it still doesn't detect some slighter cycle slips, which create peaks in the pseudorange measurement and can degrade the position solution.

Finally, there are some quirks in the Kalman Filter algorithms that originate jumps in the position estimate. While they haven't produced a significant enough error in the data set used for this thesis, it cannot be entirely excluded that there exist cases where a significant jump can seriously degrade the position solution, so further refinements of the Kalman Filters should be considered.

Bibliography

[1] M. S. Grewal. *Global Positioning Systems, Inertial Navigation, and Integration*. Wiley, John & Sons, Incorporated, 2001. ISBN 9780471200710,0-471-20071-9.

[2] The White House, Office of the Press Secretary. Statement by the President regarding the United States' decision to stop degrading Global Positioning System accuracy. https://clintonwhitehouse3.archives.gov/WH/EOP/OSTP/html/0053_2.html, . Accessed on: 08-06-2020.

[3] The White House, Office of the Press Secretary. statement by the press secretary, .

[4] E. D. Hegarty, Christopher; Kaplan. *Understanding GPS/GNSS*. Artech House, 3rd ed edition, 2017. ISBN 978-1-63081-058-0,9781630814427,1630814423.

[5] T. A. Stansell. The TRANSIT Navigation Satellite System. MAGNAVOX GOVERNMENT AND INDUSTRIAL ECTRONICS COMPANY, 1978. Accessible in https://www.ion.org/museum/files/TransitBooklet.pdf.

[6] The White House, Office of the Press Secretary. Statement by Deputy Press Secretary Speakes on the Soviet Attack on a Korean Civilian Airliner. https://www.reaganlibrary.gov/research/speeches/91683c, . Accessed on: 09-06-2020.

[7] E. G. Agency. GNSS Market Report, Issue 6, 2019.

[8] United States Coast Guard Navigation Center. GPS constellation status. https://www.navcen.uscg.gov/?Do=constellationStatus. Accessed on: 11-06-2020.

[9] GPS.gov. GPS Control Segment. https://www.gps.gov/systems/gps/control/. Accessed on: 11-06-2020.

[10] N. G.-I. A. (NGA). *World Geodetic System 1984, Its Definition and Relationships with Local Geodetic Systems*. Department of Defense, United States of America, 1.0.0 edition, 7 2014. Accessed on: 18-09-2020.

[11] M. Heikkinen. Ggeschlossene formeln zur berechnung räumlicher geodätischer koordinaten aus rechtwinkligen koordinaten. *Z. Vermess, Vol. 107, pp. 207-211*, 1982.

[12] J. Zhu. Conversion of Earth-centered Earth-fixed coordinates to geodetic coordinates. *IEEE Transactions on Aerospace and Electronic Systems*, 30, 7 1994. doi: 10.1109/7.303772.

[13] H. Vermeille. Computing geodetic coordinates from geocentric coordinates. *Journal of Geodesy*, 78, 09 2004. doi: 10.1007/s00190-004-0375-4.

[14] J. E. Sanguino. *Sistemas de Navegação - Apontamentos das Aulas*. Instituto Superior Técnico, 2017/2018.

[15] GPS Directorate. *IS-GPS-200K, NAVSTAR GPS Space Segment/Navigation User Segment Interfaces*. U.S. Air Force GPS Directorate, El Segundo, CA, 2019.

[16] S. Storm van Leeuwen, H. Marel, M. Tossaint, and A. Martelluci. Validation of SBAS MOPS Troposphere Model over the EGNOS Service Area. January 2004.

[17] RTCA, Inc. *Minimum Operational Performance Standards for Global Positioning System/Wide Area Augmentation System Airborne Equipment, RTCA DO-229D*, 2006.

[18] J. Klobuchar. A first-order, worldwide, ionospheric, time-delay algorithm. 1975.

[19] Y. X. a. Guochang Xu. *GPS: Theory, Algorithms and Applications*. Springer-Verlag Berlin Heidelberg, 3 edition, 2016. ISBN 978-3-662-50365-2,978-3-662-50367-6,87-7866-158-7,978-3-642-32792-6.

[20] GPS position accuracy measures. Application Note APN-029, NovAtel, December 2003.

[21] T. K. Yaakov Bar-Shalom, X. Rong Li. *Estimation with applications to tracking navigation*. Wiley-Interscience, 1 edition, 2001. ISBN 047141655X,9780471416555,9780471465218.

[22] M. C. Morais. *Notas de apoio da disciplina de Probabilidades e Estatística*. Instituto Superior Técnico, 2010.

[23] F. D. Nunes. *Sistemas de Controlo de Tráfego - Apontamentos das Aulas*. Instituto Superior Técnico, 2017.

[24] K. B. G. Strang. *Linear algebra, geodesy, and GPS*. Wellesley college, 1997. ISBN 9780961408862,0961408863.

[25] A. Q. Le. Achieving decimetre accuracy with single frequency standalone gps positioning. In *Proceedings of the 17th International Technical Meeting of the Satellite Division of The Institute of Navigation (ION GNSS 2004)*, pages 213–237, 2004.

[26] R. G. Brown and P. Y. C. Hwang. *Introduction to Random Signals and Applied Kalman Filtering with Matlab Exercises*. Wiley, 4 edition, 2012. ISBN 0470609699,9780470609699.

[27] M. Wickert and C. Siddappa. Exploring the extended kalman filter for gps positioning using simulated user and satellite track data. In *Proceedings of the 17th Python in Science Conference (SCYPI 2018)*, pages 84–90, 01 2018. doi: 10.25080/Majora-4af1f417-00d.

[28] F. Zhu, Y. Zhang, X. Su, H. Li, and H. Guo. GNSS position estimation based on unscented Kalman filter. *2015 International Conference on Optoelectronics and Microelectronics (ICOM)*, pages 152–155, 07 2015. doi: 10.1109/ICoOM.2015.7398793.

[29] K. Mazher, M. Tahir, and K. Ali. GNSS pseudorange smoothing: Linear vs non-linear filtering paradigm. In *2016 IEEE Aerospace Conference*, pages 1–10, 2016. doi: 10.1109/AERO.2016.7500779.

[30] J. P. D. Duarte. Integrity monitoring techniques in GPS/Galileo. Master's thesis, Instituto Superior Técnico, 2015.

[31] Navipedia. RAIM Algorithms. `https://gssc.esa.int/navipedia/index.php/RAIM_Algorithms`, . Accessed on: 13-11-2020.

[32] F. de Oliveira Salgueiro. Evaluation of GPS Standalone Single Frequency Receiver Autonomous Integrity Monitoring Algorithms. Master's thesis, Instituto Superior Técnico, 2014.

[33] F. D. Nunes. *Notes on RAIM*. Instituto de Telecomunicações - Instituto Superior Técnico, 2011.

[34] B. Z. Junren Sun, Zun Niu. Fault detection and exclusion method for a deeply integrated bds/ins system. *Sensors*, 20, 03 2020. doi: 10.3390/s20071844.

[35] International GNSS Service. Products. `https://www.igs.org/products`. Accessed on: 2-11-2020.

[36] Navipedia. Satellite antenna phase centre. `https://gssc.esa.int/navipedia/index.php/Satellite_Antenna_Phase_Centre`, . Accessed on: 2-11-2020.

[37] RTKLIB Github page. `https://github.com/tomojitakasu/RTKLIB`. Accessed on: 2-11-2020.

[38] T. Takasu. *RTKLIB ver. 2.4.2 Manual*. Tokyo University of Marine Science and Technology, April 2013.

[39] G. Dardanelli, C. Pipitone, A. Angrisano, S. Gaglione, and A. Innac. Performance Assessment of PPP Surveys with Open Source Software Using the GNSS GPS–GLONASS–Galileo Constellations. *Applied Sciences (Switzerland)*, 10, 2020. ISSN 2076-3417.

[40] u-blox. *LEA-6 u-blox 6 GPS Modules Data Sheet*, February 2017.

[41] Ashtech. *ProFlex 500 Reference Manual*, April 2011.

[42] NovAtel. *NovAtel GPSAntenna Model 521 - User Information*, September 1999.

[43] T. Nischan. GFZRNX - RINEX GNSS Data Conversion and Manipulation Toolbox. V. 1.13. *GFZ Data Services*, 2016. doi: 10.5880/GFZ.1.1.2016.002.

[44] P. M. F. e Silva. *Antenna Survey, IT GNSS Monitoring Station*, June 2013.

[45] International GNSS Service (IGS). High-rate (1-second) GNSS observation data. URL `ftp://gssc.esa.int/gnss/data/highrate/`.

[46] ICAO. *AN-WP/7556 Addendum No.1 Appendix, Draft amendment to Annex 10 of the Convention on International Civil Aviation, Volume I - Radio Navigation Aids*.

Appendix A

Routines for downloading IGS GNSS data

In this section, the source code for the routines used to extract and merge data from the IGS FTP website is provided.

A.1 IGS_dump.bat

```
@echo off

for %%A in (00 01 02 03 04 05 06 07 08 09 10 11 12 13 14 15 16 17 18 19 20 21 22 23 24) do (
echo Going for %%A
wget -e robots=off -r -nH --cut-dirs=6 --no-parent "ftp://gssc.esa.int/gnss/data/highrate/2020/299/%%A"
↪  -P gssc_esa_int_highrate -A "MGUE00ARG_R_2020299*.crx.gz"

wget -e robots=off -r -nH --cut-dirs=6 --no-parent "ftp://gssc.esa.int/gnss/data/hourly/2020/299/%%A"
↪  -P gssc_esa_int_highrate -A "MGUE00ARG_R_2020299*.rnx.gz"
)
pause

for %%f in (gssc_esa_int_highrate\*) do ("C:\Program Files\7-Zip\7z.exe" -ogssc_esa_int_highrate x %%f)

move gssc_esa_int_highrate\*.gz gssc_esa_int_highrate\dump

pause

cd gssc_esa_int_highrate

for %%f in (*) do (..\..\RNXCMP_4.0.7_Windows_bcc\bin\crx2rnx.exe %%f)

del *.crx
mkdir nav
mkdir obs
move *_MN.rnx nav
move *_MO.rnx obs
pause
```

A.2 IGS_merge.bat

```
@echo off

..\gfzrnx_win64.exe -vnum 3.02 -no_nav_stk --nav_sort time -satsys G -finp gssc_esa_int_highrate\nav\* -fout gssc_esa_int_highrate\::RX3::"

for %%A in (00 01 02 03 04 05 06 07 08 09 10 11 12 13 14 15 16 17 18 19 20 21 22 23) do (
..\gfzrnx_win64.exe -f -ot S1C,D1C,L1C,C1C -satsys G -finp .\gssc_esa_int_highrate\obs\MGUE00ARG_R_2020299%%A* -fout "gssc_esa_int_highrate\obs\hourly_merged\::RX3::"
)
pause

..\gfzrnx_win64 -f -splice_direct -finp gssc_esa_int_highrate\obs\hourly_merged\*_GO.rnx -fout gssc_esa_int_highrate\::RX3::
```

Appendix B

Surveying procedure

In this chapter, a more in-depth explanation of the surveying procedure will be done, for both the 7 day datasets of the u-blox receivers and the 2 day dataset of the ProFlex 500 receiver.

B.1 7 day survey - Antennas RF2 and RF6

For this survey, the antennas were connected to a laptop computer using an USB cable, which allowed serial communications between the computer and receiver. The communication was done at 9600 baud, and receiver configuration and data recording were handled by the software *u-center* from u-blox. Due to instability of recent versions of the software when using the u-blox 6T receivers, the version used was version 19.02. The receivers were configured to log the following receiver-specific messages at the rate of 1 Hz (ignoring the standard NMEA data messages):

- **RXM-RAW**, which contains the observation data
- **RXM-SFRB**, which contains the subframe data of the navigation messages

The SBAS data was also collected by activating the SBAS subsystem in the Configurations menu, even though said data was not used for this thesis

With the configuration finalized, the data capture process was then initiated. To this end, the data was recorded using the record functionality of u-center, starting a few hours before the start of GPS week 2129. This allowed for the complete reception of the ephemeris data by the start of the survey window, avoiding the use of the imprecise almanac parameters, while also allowing for a final check of the receiver configuration. Finally, the survey was then allowed to run for an entire GPS week, being terminated on 1/11/2020, with the collected data saved as a .ubx file.

This survey data was then processed using RTKLIB version 2.4.3 beta 33, in order to convert the data from the proprietary UBX message format to the RINEX 3.02 format, chosen because it is the standard format for sharing GNSS data. In this software, the survey was trimmed to consist only in the observations from midnight of 25/10/2020 to 23:59:59 of 31/10/2020, and the .ubx file converted to .nav

and .obs files, respectively for navigation messages and observations of the GPS satellites, as well as .hnav and .sbs, for the navigation messages and observations of the SBAS satellites.

Finally, the .nav and .obs files were then used in RTKLIB for the antenna reference position computation, including the IGS corrections, and also for the auto-survey methods developed in this thesis.

B.2 2 day survey - Antenna RF4

In this survey, the procedure was slightly different from the previous survey. The ProFlex 500 receiver has an integrated webserver that provides a web interface, to which a computer can connect and configure the receiver. As such, this receiver was connected to a laptop computer via a network switch, which allowed communications with the receiver's webserver. The receiver was configured to log the following receiver-specific messages, again at the rate of 1Hz:

- **NAV**, which contains the navigation message data
- **MES**, which contains the observation data
- **DAT**, which contains the subframe data of the navigation messages

In this receiver, no SBAS data was collected.

After configuration, the receiver was set to data logging mode using the web interface. Like the previous survey, the data logging was started before the designated start time to ensure that the ephemeris data has been received, and was terminated on 10/12/2020, with the logged data being saved in a proprietary data format called ATOM.

After the survey, the data was converted to RINEX 2.11 using the receiver's integrated converter, which was then further converted to RINEX 3.02 using RTKLIB. During this conversion, the observation log was trimmed to contain only the observations from midnight of 8/12/2020 to 23:59:59 of 9/12/2020, resulting in a .obs file with the observation data and a .nav file with the navigation messages.

These files were then used in RTKLIB, together with the IGS corrections, to compute the antenna reference position used in this thesis.